Active Separation Control By Multiple Cooperative Actuation

vorgelegt von
Dipl. Ing.
Markus Blechschmidt
geb. in Dettelbach

von der Fakultät V - Verkehrs- und Maschinensysteme
der Technischen Universität Berlin
zur Erlangung des akademischen Grades
- Dr.-Ing.-

genehmigte Dissertation

Promotionsausschuss:

Vorsitzender:	Prof. Dr.-Ing. Dieter Peitsch
Gutachter:	Prof. Dr.-Ing. Wolfgang Nitsche
Gutachterin:	Dr. rer. nat. Karin Bauer

Tag der wissenschaftlichen Aussprache: 22.12.2016

Berlin 2017

Abstract

This thesis aims at reducing the impulse and the required mass flow needed in active separation control by pulsed actuation systems. The investigated strategy to achieve this is based on the cooperative action of multiple rows of actuators positioned downstream of each other. As shown by the analysis of PIV measurements in conjunction with pressure measurements, the fluidic rows can be actuated such that the flow structures (vortices) they produce are strengthened and stabilized by subsequent actuator rows while they propagate downstream. This strategy was applied to the reattachment of pressure induced separation on a planar half diffuser with variable step angle. A maximum reduction of 67% in total actuation momentum could be achieved compared with a single row of actuators. The authority requirements on the single actuator can be reduced by 89% c_μ , thus smaller and lighter actuation devices can be used to solve the flow control problem in future. A mass flow reduction up to 21% can be achieved by using a non-optimized cooperative actuation system. In future, a saving of approximately 30% is estimated if the system parameters, e.g. the duty cycle or a control algorithm regarding to the propagation velocities of the vortices, are fine tuned further. It is shown that this system is suitable to reattach the flow with less resources and therefore it is worth the additional effort.

Zusammenfassung

Diese Arbeit zielt darauf ab den Impuls und den Massenstrom eines gepulsten aktiven Systems zur Beeinflussung abgelöster Strömungen zu verringern. Um dieses Ziel zu erreichen wurden mehrere Reihen von Aktuatoren hintereinander in Strömungsrichtung angeordnet. Mit Hilfe von PIV und Druckmessungen kann gezeigt werden, dass die verantwortlichen Strömungsstrukturen stabilisiert und verstärkt werden. Dieses System wurde dann auf einen Halbdiffuser übertragen, bei dem der Stufenwinkel stufenlos eingestellt werden kann und somit eine Druck induzierte Ablösung erzeugt wird. Die kooperative Aktuatorik erreicht hier eine Reduzierung des gesamten Impulsbeiwertes von 67% und eine Reduzierung des Impulsbeiwertes beim Einzelaktuator von bis zu 89%. Damit lassen sich in Zukunft kompaktere und leichtere Aktuatoren verwenden oder verworfene Aktuator-Konzepte neu beleben. Der Massenstrom lässt sich mit einem nicht optimierten System um 21% reduzieren. Es wird angenommen, das bei einer weiteren Optimierung der Aktuatorparameter, wie z.B. der Pulsweite oder durch die Installation eines Algorithmus der den Phasenwinkel kontrolliert, bis zu ca. 30% eingespart werden können. Es wird gezeigt, dass mit dieser Art der Strömungsbeeinflussung die Anforderungen an den benötigten Massenstrom sowie an den Impulsbeiwert der Aktuatoren reduziert werden können. Mit den erbrachten Einsparungen lässt sich der höhere Systemaufwand insgesamt durchaus rechtfertigen.

Throughout the centuries
there were men who took first
steps down new roads armed
with nothing but their own
vision.

(Rand, Ayn)

Acknowledgments

The present thesis was developed as research associate at Airbus Group Innovations in cooperation with the Department of Aeronautics and Astronautics of the Berlin University of Technology. I acknowledge the support and funding of this work received through the German national program LuFo 4. I want to especially thank Heribert Bieler from Airbus Bremen for his support throughout the investigations.

First I want to express my sincere thanks to my thesis supervisor, Prof. Dr.-Ing. Nitsche, for his constant support and encouragement to carry out this work. The discussions, his comments and editorial advices were helpful to find the overall direction and essential to finish this thesis.

It was always a pleasure to work with the people at the Department of Aeronautics and Astronautics of the Berlin University of Technology. Especially, I would like to thank Marcel Staats and Dr. Matthias Bauer for their assistance and discussions during the wind tunnel experiments.

I also thank my colleagues, Winfried Kupke and Roland Wagner, for their technical assistance and arguments during my work at Airbus Group Innovations. Particularly, I would like to thank Rafael Knobling for his friendship and the sometimes heated, but always fruitful discussions we had in Ottobrunn.

I gratefully acknowledge Dr. Karin Bauer for her support, the constructive contributions and her management during my work in her team. It was a pleasure to work with her on different projects. I thank her for her engagement and for giving us the opportunity to build up a reasonable lab.

On a personal note, I would like to thank my siblings for the great times we had and will have. They never fail in giving me the break I need. A special thank go out to my parents for their love and their unrestricted support throughout my life. Particularly, I thank my wife, Angela, for her patience, encouragement and love. Her expertise and contributions more than once saved my day.

Contents

List of Figures

Nomenclature

Roman Letters

u, v, w	velocity components [$\frac{m}{s}$]
u', v', w'	fluctuation velocity components [$\frac{m}{s}$]
$\bar{u}, \bar{v}, \bar{w}$	time average velocity components [$\frac{m}{s}$]
$\tilde{u}, \tilde{v}, \tilde{w}$	median velocity components [$\frac{m}{s}$]
$\langle u \rangle, \langle v \rangle, \langle w \rangle$	phase locked velocity components [$\frac{m}{s}$]
c_μ	Momentum coefficient [-]
c_p	Pressure coefficent [-]
VR	Velocity Ratio [-]
PR	Propagation Ratio [-]
Re	Rynoldsnumber [-]
F^+	Strouhalnumber [-]
f	Frequency [$\frac{1}{s}$]
f_g	Cuttoff Frequency [$\frac{1}{s}$]
F_s	Sample frequency [$\frac{1}{s}$]
$\dot{m}$	Mass flow [$\frac{kg}{s}$]
$\dot{V}$	Volume flow [$\frac{l}{min}$]
Ma	Mach number [-]
Tu	Grade of turbulence [$\%$]

Greek Letters

α_{step}	Step angle [$^\circ$]
Θ	Phase of excitation [$^\circ$]
ω	Vorticity [$\frac{1}{s}$]
Λ	Duty Cycle [$\%$]
Δ	Difference
Δc_p	Pressure recovery [-]
σ	Standard deviation
Φ	Cross correlation, Phase angle [$^\circ$]

Subscript

$1, 2, 3$	number of actuator (row)
40	$40mm$ distance of two actuator
H	Height
c	Calibration
∞	refer to incident flow
i	control variable
jet	refer to jet

LE	Leading Edge
x	refer to position

Abbreviations

A	Area
AFC	Active Flow Control
AFM	Aerodynamic Figure of Merit
AR	Aspect ratio
CTA	Constant Temperature Anemometer
CCD	Charged Coupled Device
DEHS	Di-Ethyl-Hexyl-Sebacat
DSP	Digital Signal Processing
ER	Expansion Ratio
HF	Hot Film
PID	Proportional Integral Derivative
PIV	Particle Image Velocimetry
RMS	Root Mean Square
TR-PIV	Time Resolved Particle Image Velocimetry
ZNMF	Zero-Net-Mass-Flux

1 Introduction

The wing design is a major topic for aircraft manufactures all over the world. Most of the time an operating aircraft is in the flight phase called *cruise*. In this flight phase the aircraft travels at high altitude and high subsonic speed. Since it spends most of the time, especially on long distance routes, in this state, the wing is optimized for this conditions. The cruise and induced drag as well as the fuel consumption are a few examples of the engineering effort wing aerodynamicists are dealing with. Different systems are employed like sophisticated wing tips, super critical airfoils or high-bypass engines to enhance the aerodynamics. Despite the enormous effort to maximize the performance of these wings, there are still some critical regions, especially in low speed flight conditions, like the start and landing phase. In these specific flight phases the performance must be enhanced by using high lift devices. The common solution is to extend slats and flaps, which are changing the geometry and therefore the aerodynamics of the wing. They enable higher angle of attacks and thus higher lift coefficients, before the flow separates from the wing. These devices have been optimized over the years to enhance the performance. Unfortunately the high lift devices increase the overall system effort and increase weight. Nevertheless there are no alternatives to date.
Although the optimization has been enhanced, mainly two regions are still challenging. Namely the leading edge of the outer wing and the pylon wing integration of the jet engines. Due to the restricted space requirements, it is not possible to deploy slats at these positions. These are the locations, which are endangered to separate, due to the uncovered leading edge at angles of attack where the remaining wing is still in its working range.
Here, active flow control (AFC) systems can be deployed to solve this issue. It is proven that AFC is capable of reattaching or at least delaying separated flow [57, 71]. Such a system would increase the performance of the high lift devices towards higher angles of attack. Up to date, there is no commercial airliner equipped with an active flow control system.
However, there is always a drawback. An AFC system, capable of dealing with these flow conditions, requires a large amount of energy or mass flow of pressurized air. This mass flow must be provided during the flight and is taken either from the jet engine or an additional pressure source. Both methods would lead to cutbacks. When, that the mass flow is provided from the engine, a loss of performance is given and using an external pressure source, additional weight is added to the aircraft. Moreover, due to the restricted space requirements, especially at the outer wing, smaller and lighter actuators are preferable.
The reattachment process by means of pulsed blowing is mainly utilizing dynamic flow processes to increase the momentum within the separated area. This is done by supplying high energy fluid by means of the mass flow and to redistribute the fluid through the shear layer caused by the separation. This redistributing is driven by coherent structures induced by the pulsed blowing into the flow. These coherent structures are primarily large scale vortices. These vortices are depending on the excitation parameters, e.g the frequency,

duty cycle or the angle of the jet. Especially the latter has an effect on the formation and behavior of the vortices.
The aim of the present dissertation is to define how these vortices can be enhanced and stabilized during their downstream propagation. Thereby the behavior of two co-rotating vortices is systematically investigated during the interaction process. The driving parameter to merge these vortices is found using a non-intrusive measurement technique on a flat plate. This knowledge is then transferred to a half diffuser, where a pressure induced separation is provided. The influence of an adverse pressure gradient on the interaction process has been examined successfully. Utilizing this merging effect, the dynamic actuator parameters can be reduced. An additional estimation of the mass flow savings, achievable by the cooperative actuation, is provided.
This fundamental research of a new actuator concept represents a fresh approach to solve flow separation and thereby shows auspicious results. It also prepares the ground for further investigations and developments.

2 State of the Art

Flow separation describes the phenomena, when flow detaches from a surface or wall located in a stream. The origin of this behavior as well as the different mechanism to overcome this flow event, are described in this section. The advantages and disadvantages of several active flow control methods are shown and an overview of pulsed blowing is given. To deepen the subject of pulsed blowing, the mechanism of a jet in cross flow and the parameters to trigger this event are described.
The idea and novelty of multiple cooperative actuation are set in context to existing active separation control methods. Moreover the necessity to perform basic investigations and the aim of this thesis are described.

2.1 Separation control

2.1.1 Separation

Separation of flow occurs if a viscous fluid does not follow the body contour and is mainly distinguished in geometry induced and pressure induced separation. Geometry induced separation arises if flow separates stationary on a fixed edge or an unsteady contour by means of the mass inertia of the fluid. If the flow detaches because of a positive pressure gradient $\frac{\partial p}{\partial x} > 0$, it is called pressure induced separation as shown in Figure 2.1.
In this thesis a new method to reattach pressure induced separation is presented and therefore the mechanism of this kind of separation is explained in the following with respect to an incompressible fluid. The boundary layer before the separation is marked as turbulent. The kinetic energy of a fluid is converted into pressure by means of deceleration of the flow. This occurs, for example, at cross section expansion of a diffuser, where the static pressure is constantly increasing in flow direction. This leads to a positive pressure gradient in direction of flow $\frac{\partial p}{\partial x} > 0$. The pressure gradient of the boundary layer perpendicular to the flow $\frac{\partial p}{\partial y}$ can be neglected. Referring to Prandtl's boundary layer hypothesis the static pressure of the external flow is influencing the boundary layer and therefore the deceleration of the flow is directly linked to the boundary layer and leads to a deceleration of the velocity gradient $(\frac{\partial u}{\partial y})_W$. With increasing pressure gradient the deceleration of the velocity is also increasing and by means of decreasing kinetic energy. If the positive pressure gradient becomes too high the fluid is slowed down to standstill $(\frac{\partial u}{\partial y})_W = 0$. At this point the wall shear stress also becomes zero $\tau_w = 0$ and the fluid separates from the contour. After this point a recirculation area builds up due the further deceleration of the velocity close to the wall. This deceleration results in the fluid flowing against the main flow direction $(\frac{\partial u}{\partial y})_W < 0$. This recirculation area distract the flow away from the wall and a shear layer between recirculation area and external flow is build up

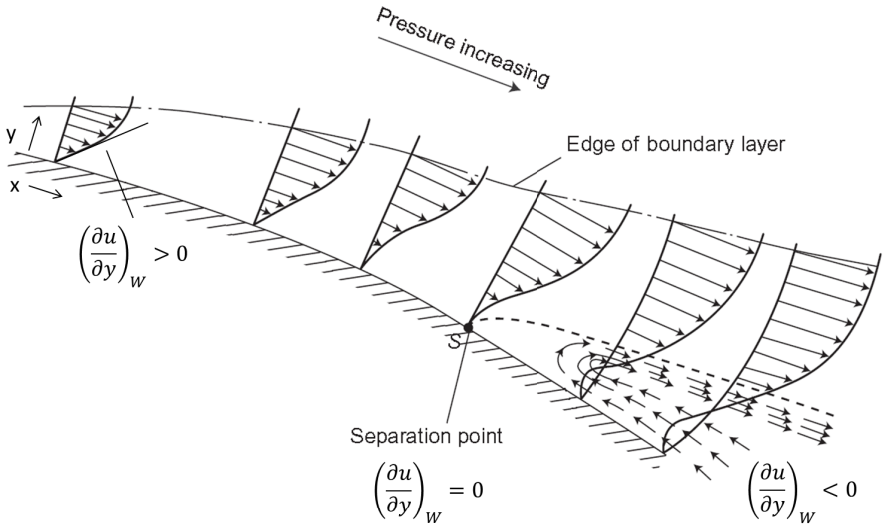

Figure 2.1: Pressure induced separation on a curved surface [5]

(see Figure 2.1). The reattachment process is triggered by the development of vortices in the free shear layer which leads to a momentum exchange between the recirculation area and the external flow. In case of a curved surface, e.g. a half diffuser, the recirculation area is bounded by the wall and therefore the separation is reattached because of the more intense momentum transfer [8].

2.1.2 Strategies for separation control

In fluid mechanics flow control means changing the state of flow by specific measures. The complexity and dynamic of the control system are determined by the state of the flow. The method of flow control has to be coordinated with the the flow behavior to maximize the mechanism to reach a certain effect. Using the right flow control method it is possible to influence the flow in a positive way, e.g. drag reduction or lift increase, which leads to an economic advantage.
The methods are principally distinguished in **passive** and **active** methods [25], where passive methods do not require auxiliary power or a control loop, while active devices need energy expenses. There are different passive methods to deal with separation. The physical principles can be subdivided as follows [32]

- Shear layer entrainment
- Momentum increase
- Influencing the pressure gradient $\frac{\partial p}{\partial x}$
- Modifying the boundary layer profile $\frac{\partial u}{\partial y}$

Vortex generators are an example for shear layer entrainment and can delay separation locally. This is done by supplying high energy fluid to the separation prone area by

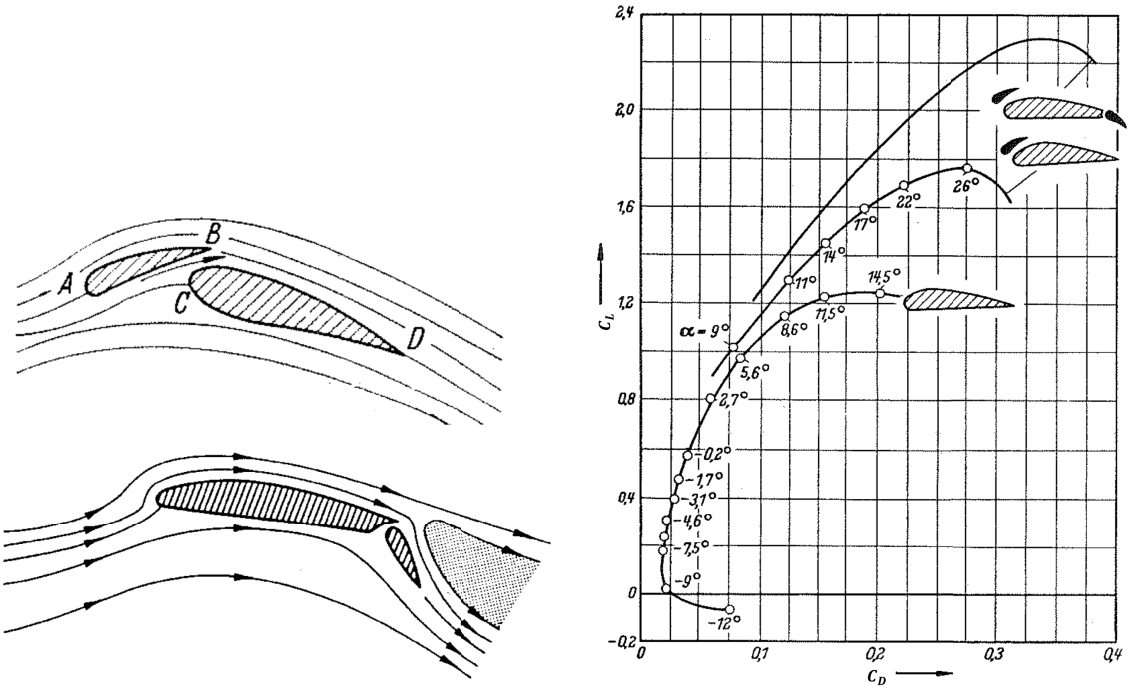

(a) Schematic flow around slat and flap [2] (b) Lift-to-drag ratio comparison of slat and flap [67]

Figure 2.2: Mechanism of high lift devices

generating longitudinal vortices [45]. These vortex generators have the disadvantage of producing parasitic drag, even if the boundary layer is not separation prone. Switching the boundary layer to turbulent is another form of passive flow control. Due to the higher velocity gradient, the turbulent boundary layer is more resistance against separation[63]. However, the most common standard of passive flow control is to optimize the shape of the airfoil. Hereby, the geometry of an airfoil is optimized during the design process to ensure a less pronounced positive pressure gradient and therefore the flow remains attached over a longer distance [71, 50]. It is also possible to supply energy to the separation prone flow by adding further elements to the airfoil geometry. These elements, normally slats and flaps, supply energy from the surrounding flow field, enhancing the lift to drag ratio as shown in Figure 2.2. Using flaps increases the curvature of an airfoil and therefore the circulation around the profile. The circulation then increases the lift by Δc_l. Hereby higher lift coefficients can be reached at the same angle of attack α compared to the baseline without any flap. On the other hand the higher curvature also leads to an increase of the pressure gradient which results in a higher load of the airfoil. Therefore the maximum lift is reached at smaller angle of attack. The separation can then be pushed to higher angles of attack by using a slotted flap. This slot supplies the separation prone boundary layer of the suction side with energy from the pressure side of the airfoil. This effect can be enhanced even further by using multiple slotted flaps.
Another way to reach a higher maximum lift at higher angles of attack is to install slats. The pressure distribution is manipulated by the flow through the slot between slat and airfoil in such a way that the positive pressure gradient decreases. This effect delays separation to a higher angle of attack and increases maximum lift $C_{l,max}$. The buoyancy at lower angles

of attack is hardly affected by the slats [74].
Active flow control affects the velocity profile by injecting high energy fluid, sucking low energy fluid or redirecting high energy fluid to the wall. The impulse of the flow is actively increased by these actuator systems, which are always supplied by an external energy source. The advantages of these systems are that the flow control can be adjusted to the flow conditions, and they can be turned on and off, depending on whether they are needed or not. The relevance of active flow control was shown by Ludwig Prandtl by implementing a boundary layer suction on a circular cylinder, delaying the separation of the cylinder flow [60]. In the late 1920s Bamber [3] investigated the effect of steady blowing on the lift-to-drag ratio. Furthermore the parameters of the slot were investigated. It was proven that the lift-to-drag ratio of a conventional two dimensional airfoil could be increased up to $150\,\%$. With the definition of the momentum coefficient C_μ by Poisson-Quinton an effective scaling parameter was found. An extensive review of the boundary layer control with steady working actuator systems is given by Lachmann [41].
Since the relevance of momentum was shown, Collins and Zelenevitz [10] demonstrated that acoustic and therefore periodic excitation can increase the momentum near the surface by transferring it from the free-stream. A lot of experiments were done later on, addressing different issues of acoustic excitation [87, 1, 53]. Despite of the disadvantages of such systems, e.g. complexity and high amplitude of excitation, the effectiveness of pulsed blowing was shown. In a next step the excited mixing layer was examined [56, 34, 6, 35]. It is now accepted that large vortical, spanwise structures are the building blocks of the mixing layer and are responsible for the momentum transfer across its extent [28] (See Figure 2.3). A detailed discussion of the mechanism of inciting the instabilities of a shear layer is given in section 2.2.3. Further investigations of periodic excitation are more application oriented e.g. airfoils and high-lift configurations. The examinations range from generic flaps [54], NACA airfoils [39, 69], trailing edge flaps without slot [68, 47] to single slotted flaps [80, 85]. The focus of these examinations are the effect of the active flow control on an overall aerodynamic configuration with regard to lift enhancement and drag reduction.
The flow reattachment method introduced in this thesis, is by means an active flow control method and furthermore periodic actuation is used. Therefore the next sections give an overview over the mechanism of periodic actuation.

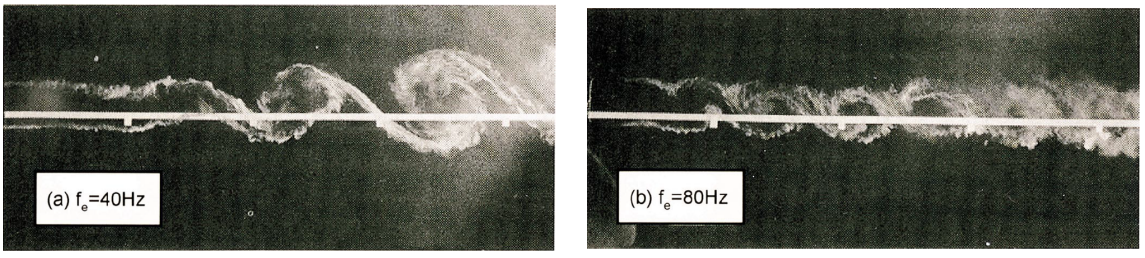

Figure 2.3: Smoke flow visualization at two different frequencies showing large vortical spanwise structures which are responsible for large momentum transfer [56]

2.2 Mechanism of periodic actuation

2.2.1 Flow control systems

Providing periodic excitation different designs of actuators can be used. There are oscillating flaps, flexible surfaces, rotating valves, plasma, combustion driven and fluidic actuators and mechanical valves. An detailed and comprehensive overview and comparison of all kinds of actuators are given by Cattafesta III & Sheplac [7]. A useful classification is organizing the actuators by function.
Fluid injection or suction, in Figure 2.4(a) the fluidic part built hereby the most common type of actuators. Within the fluidic type the actuators have to be distinguished between continuously and periodic working systems (Figure 2.4(b)). The periodic systems have the advantage of reducing the amount of energy needed to reattach the separated flow compared to continuously working actuators. The disadvantage, on the other hand, is that the system becomes more complex. In addition, the periodic systems are divided into oscillating blowing and sucking, so called zero-net-mass-flux (ZNMF) [88] and pulsed blowing where the fluid is externally provided. The oscillating sucking and blowing result in a time averaged jet above the actuator slot which provided a positive momentum into the flow. This jet is called *synthetic jet* [27] (see Figure 2.5(a)). The synthetic jet sucks in low momentum fluid from the boundary layer and blows the sucked in fluid back in the flow. Since there is no external fluid supply this actuator has a time-averaged net-mass-flux of zero. The oscillation is generated electrically and is converting electric power into fluid power as a result. A lot of effort was put into the investigations of synthetic jets to over come the disadvantages of these actuators e.g. the limitation in frequencies [61], heat development and low momentum and velocity output [76]. An extensive overview on synthetic jets and their application is given by Glezer and Amitay [27].
A device which can generate high jet velocities is the *pulsed combustion actuator* (see Figure 2.5(c)). The high momentum jet is produced by igniting a fuel oxidant mixture [16] which triggers a detonation. This detonation causes a rapid pressure increase in the

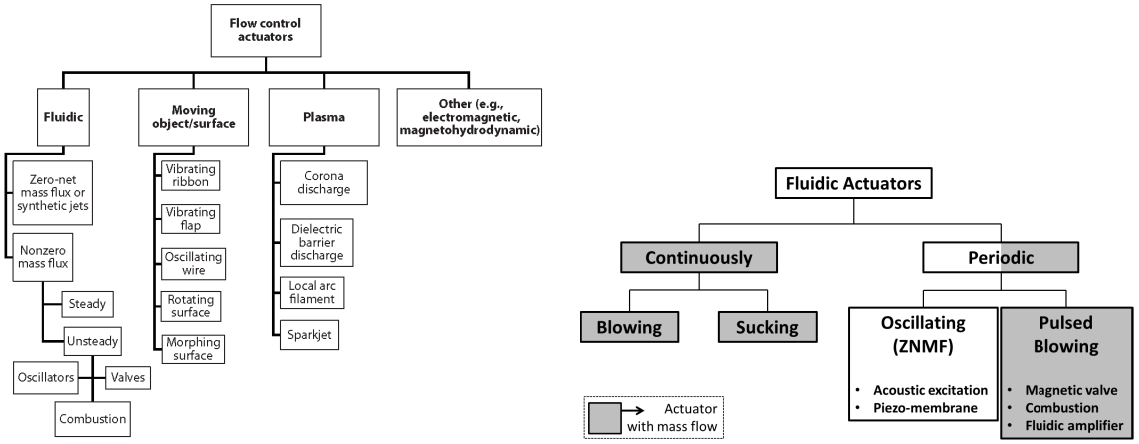

(a) A type classification of flow control actuators [7]

(b) Classification of fluidic actuators for active flow control [32]

Figure 2.4: Classification of actuators (a) and distinction of periodic actuation (b)

cavity which then ejects the unburned air through an orifice, but also emits the combustion products. This possible compact design provides a high energy density with high jet velocities. Using auto-ignition by reflecting pressure waves and cavity resonance [16] the pulse repetition rate can be increased from $f \approx 100\,\mathrm{Hz}$ up to $f \approx 1\,\mathrm{kHz}$ [13]. The drawbacks of this type of actuation are that the emitted combustion products are extremely hot and combustible material is required. Moreover an additional engine process within the wing or aircraft is not very desirable.
An actuator which overcomes a drawback all other have, is the fluidic oscillator [78] or fluidic actuator [4]. This device has no moving or electrical components and is therefore a simple and robust device (see Figure 2.5(d)). The working principle was first patented in 1964 [38] and relies on the principle that a primary jet is switched between two stable states. These actuators are sub-categorized in self-switching and external triggered devices. The external trigger can be mechanical components [15], plasma actuators [30] or piezoelectric benders [29]. The self-switching devices can be divided in actuators with mass flow feedback and pressure feedback [51]. Other actuators following the same principle as well as the physical behavior are explained in detail by Bauer [4]. Besides the advantage that no moving parts are involved, these actuators can provide high jet velocities within a large frequency range. On the other hand, an external pressurized fluid supply is still necessary and the amplitude and frequency are directly coupled for practical designs.
In order to reduce the development effort for experiments, mechanical valves can be used.

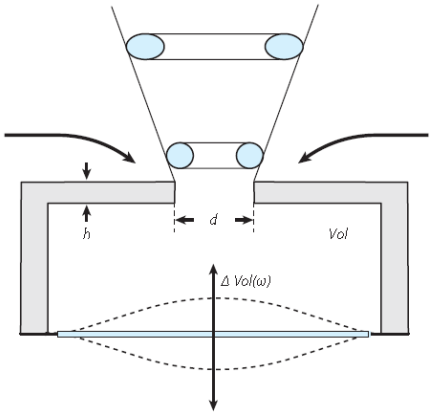

(a) Synthetic jet with piezoceramic diaphragm [7]

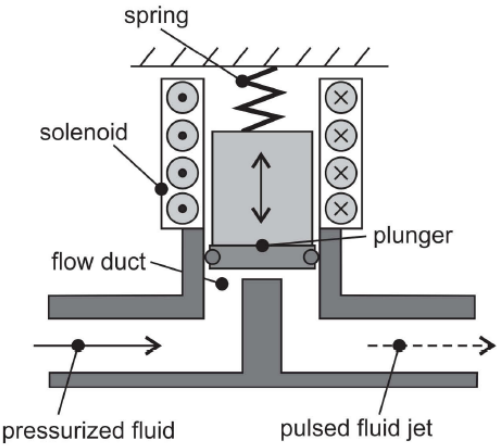

(b) Mechanical valve [4]

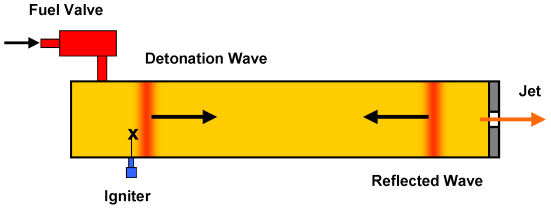

(c) Resonant Detonation Actuator [16]

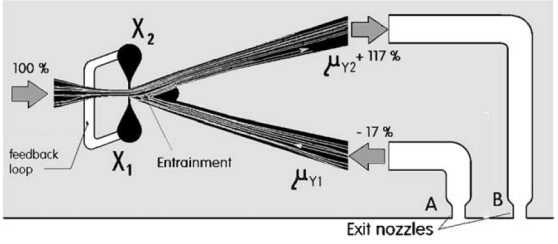

(d) Fluidic oscillator with feedback loop [77]

Figure 2.5: Example of different actuator types

These off the shelf valves operate with a plunger driven by a solenoid, opening and closing a flow channel (see Figure 2.5(b)). These devices need pressurized air as an inlet and a slotted actuator to work as an active flow control device [57]. The actuator normally transforms the flow from a round inlet to a slotted outlet (aspect ratio $>> 1$). The performance of the system is given by the valve technique, where the switching time is dominating the duty cycle depending on the frequency. The amplitude is regulated by the mass flow rate and is also depending on the valve technique. Fast switching solenoid valves (e.g. Festo^{TM}*MHE*) keep the balance between amplitude and frequency. The duty cycle and frequency are also controllable over a wide range. The response of the jet velocity to the trigger signal is depending on various factors like the chamber of the actuator and the length of the hoses connecting the actuator with the valve. Another often used actuator are the rotary valves [68], which can provide high frequencies (up to $f = 1\,\mathrm{kHz}$) and high mass flow rates. The duty cycle is fixed and therefore can not be varied during an experiment. Since the flow is unidirectional from the inlet to the outlet, these actuators have a positive net-mass-flux and thereby belong to the injection type actuators. Periodic excitation is characterized by some parameters. These can be divided in physical and geometrical parameters. Physical ones include the frequency, the duty cycle and the amplitude and can also be called variable parameters. The geometrical ones are related to the actuator and contain the shape and the direction of the slot, but also the position of the actuator in the experiment. The flow conditions are commonly varied in terms of the similarity parameters Mach number and Reynolds number. Nevertheless the actuation system itself has to be in accordance with the corresponding experiment and therefore the optimal exciting parameters can not be directly transferred from one investigation to another [86].

2.2.2 Influence of actuator parameters

The physical parameters are also called variable parameters, because they can be varied during the experiments. Several parameters are used in active flow control and are presented in a normalized form. Frequency is generally defined, analogously to the Strouhal number, as normalized frequency F^+ and given in Equation 2.1.

$$F^+ = St = \frac{f_{AFC} \cdot l_{ref}}{u_\infty} \tag{2.1}$$

The frequency is normalized by the characteristic length l_{ref} and the incident velocity u_∞. In general, the distance between actuator and trailing edge of the model is used for l_{ref}. Thereby the introduced vortex structure refers to the length of the separation area of the step or flap. This implies that, with a dimensionless frequency of $F^+ = 1$, the wavelength of the generated oscillation correspond exact to the characteristic length of the model. Sometimes the step height *H* or the diameter of a diffuser *D* is also taken. Depending on the normalized frequency the different scales of vortex structures are generated. By increasing the frequency the single vortices are decreasing until no coherent vortex structures can be identified anymore, when $F^+ = 10$ [26]. With small excitation frequencies the coherent vortex structures are leading a periodic attachment of the free shear layer to the surface, whilst with high frequencies the form of the model is changed by a vortex layer (*trapped vorticity* [26]) which prevent separation in the first place.

The duty cycle describes the ratio between the time of blowing through the slot τ to the length of the period $T = \frac{1}{f}$ of the actuator and is therefore linked to the frequency. In Equation 2.2 the duty cycle is given as a percentage, where $\Lambda = 0\,\%$ means no actuation and $\Lambda = 100\,\%$ is steady blowing. In case of fast switching solenoid valves it can be varied between $20\,\%$ and $80\,\%$ due to the response time of the valve. Normally a duty cycle of $\Lambda = 50\,\%$ is used, which means the blowing time and pause are equal.

$$\Lambda = \frac{\tau}{T} \cdot 100 \tag{2.2}$$

The next parameter, the velocity ratio VR is stated by Nagib et al.[52] to be the dominating factor. It describes the ratio of the peak jet velocity to the free stream velocity as given in Equation 2.3.

$$VR = \frac{u_{jet}}{u_\infty} \tag{2.3}$$

To investigate the influence of several parameters Nagib et al. varied the geometrical actuator parameter by changing the width of a tangential blowing jet. By doing so they were able to alter the momentum coefficient and the velocity ratio independently of each other. It has been shown that the active flow control performance is increasing the narrower the actuator slot, leading to the highest velocity ratio, whilst the momentum input is the same.
The velocity ratio depends on the actuator geometry and position, therefore this parameter is not sufficient to establish comparability between actuation concepts. Thus the introduced momentum or the interference momentum is taken in form of the momentum coefficient. This coefficient is a ratio of the interference momentum with regard to the momentum of the incident flow and is given in the generalized form for steady blowing in Equation 2.4.

$$c_\mu = \frac{J}{q_\infty \cdot A_{ref}} \tag{2.4}$$

The momentum of incident flow is given by the free stream dynamic pressure q_∞ and a reference area A_{ref}, e.g. the entry area of the wind tunnel [79] or the projected area of the model [4]. The momentum introduced by the active flow system J can be given as $\dot{m} \cdot \overline{u}_{jet}$ [79]. The time averaged mean value of the jet velocity $\overline{u}_{jet}$ would lead to a false result because the duty cycle of a system would not be taken into account. Therefore the RMS-value of the jet velocity, which rates the efficiency of the blowing, can be used [32] and is given in Equation 2.5.

$$u_{jet,RMS} = \sqrt{\frac{\tau}{T} \cdot \widetilde{u}_{jet}^2} = \frac{1}{\sqrt{\frac{\tau}{T}}} \cdot \overline{u}_{jet} \tag{2.5}$$

where

$$\widetilde{u}_{jet,\dot{m}} = \frac{\dot{m}}{\rho \cdot A_{slot}} \cdot \frac{100}{\Lambda} \tag{2.6}$$

is the jet velocity depending on the mass flow, duty cycle and the area of the slot. With Equation 2.5 the momentum coefficient can be calculated analogously to the Equation for steady blowing.

$$c_\mu = \frac{\dot{m}_{jet} \cdot u_{jet,RMS}}{q_\infty \cdot A_{ref}} \tag{2.7}$$

Based on Equation 2.7 the momentum coefficient can be determined with regard to the mass flow for every single duty cycle. Even though the momentum coefficient c_μ is commonly used to quantify the amplitude of forcing, it is not consistently defined and therefore the comparability is hardly given and has to be examined carefully.
The geometrical parameters are usually hard factors and given by the design of the actuators. The main parameters are the shape of the slot, the jet angle with regard to the model surface and also the position of the actuator slot relating to the separation. The shape of the slot orifice is mostly distinguished between radial-symmetric and rectangular. Other shapes are investigated by Salewski et al. [64], e.g elliptic or square apex, but only with small aspect ratios ($<< 1.5$). The similarity between radial-symmetric and rectangular jets with a small aspect ratio (≈ 1) are almost identical and discussed by Plesniak and Cusano [58]. Also the jet cross section, the diameter for holes and the width of the rectangular slot are relevant for the separation control task since the mass flow rate and the jet velocity depends on this parameter. Therefore, the velocity ratio for a given momentum coefficient is determined.
The location of the AFC system is normally stated upstream of the time averaged detachment line. Troshin and Seifert [82] demonstrate that the most effective and efficient actuator slot is close by, but upstream of the separation. Shmilovich and Yadlin [72] numerically

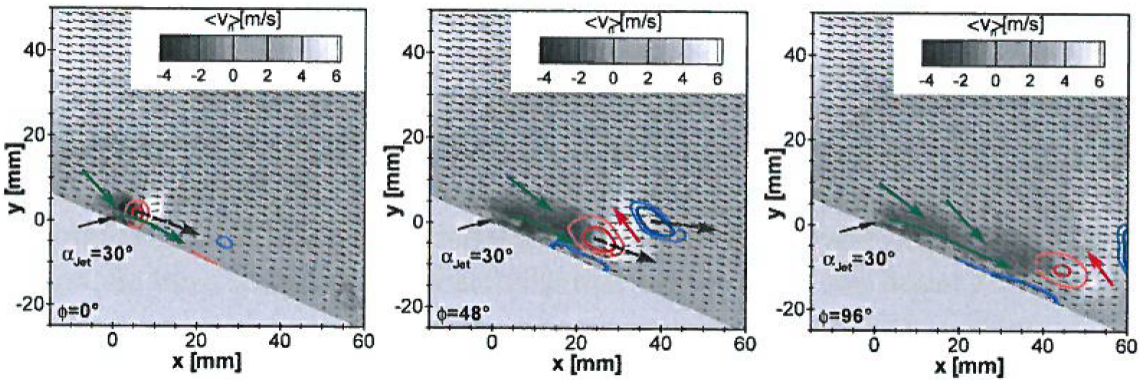

(a) Jet angle 30 °, diffuser angle 23 °

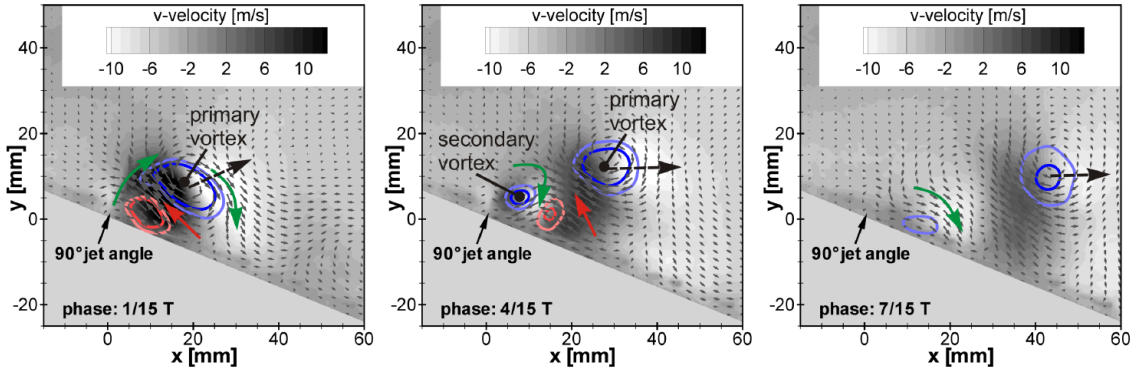

(b) Jet angle 90 °, diffuser angle 22 °

Figure 2.6: Reattachment process at different blowing angles at midspan of the diffuser step. The mean velocity is subtracted from the vector fields. blue: clockwise vortex; red: counter-clockwise vortex [33]

investigated two different positions for ZNMF actuators on a simple hinge flap. The one located upstream of the separation gains $79\,\%$ more lift then the one located downstream. However, there are no reasons given for this effect. Different experiments to examining the actuator location, ranging from leading edge to trailing edge, high deflected flaps and circular cylinder, were done by Wygnanski [86].
The jet angle relative to the local surface influences the strength and characteristics of the induced vortices. Hecklau [32] investigated the impact of different jet angles on the flow structures. Different parameters, like duty cycle, amplitude and mechanism of reattachment are analyzed independently of each other. The mechanism of reattachment can be distinguished with regard to the jet angle. Using a perpendicular jet, the reattachment process is triggered by the induced vortices only. Due to the high penetration depth of the jet, the vortex structure becomes more complex as shown in Figure 2.6(b). Thus, the reattachment is only initiated by the exchange of fluid through the shear layer. The advantage of this angle is that only a small impulse is necessary to build up a vortex and therefore the duty cycle can be kept small. Moreover, a high duty cycle can trigger a separation by itself. A low jet angle, in contrast, has the advantage by using an additional effect, called the Coandă effect. This effect causes a flow towards the wall by means of the attached jet flow which further delays the separation. The different mechanisms of the jet angle are shown in Figure 2.6.
The aim of this investigation is to enhance the fluid transferring vortices and therefore it is necessary to induce full developed vortices as it happens with a $90\,^\circ$ jet. On the other hand the additional effect is also considered. Hence, for this experimentation a $45\,^\circ$ jet angle was chosen to combine the benefits of both.

2.2.3 Mechanism of shear layer entrainment

The reattachment process is triggered by mainly two mechanisms, which are directly increasing the momentum of the separation area and through shear layer entrainment. To understand the shear layer entrainment the mechanisms of a jet in cross flow (JICF), which are investigated elaborately in the recent years [36, 65, 19, 24] are described. The jet is superimposed by the cross flow and is deflected in the direction of the flow (see Figure 2.7). Depending on the velocity ratio the penetration depth and the deflection of the jet vary. Fric [23] identified four different vortex structures resulting from a radial jet in cross flow. These structures are shown in Figure 2.7(a) and are:

- Shear layer vortices
- Counter-rotating vortex pairs
- Horseshoe vortices
- Wake vortices

With increasing aspect ratio of a rectangular slot ($>> 2$) the wall jet becomes quasi two dimensional and forms a spanwise vortex parallel to the slot, if superimposed with the cross flow (see 2.7(b)). At the edge of the slot counter-rotating streamwise vortices are formed. The influence on the spanwise vortices on the rectangular jet decreases when the length of the slot increases. The horseshoe vortices extend with the increasing slot length and are dominated by two counter-rotating streamwise vortices and are shown in Figure

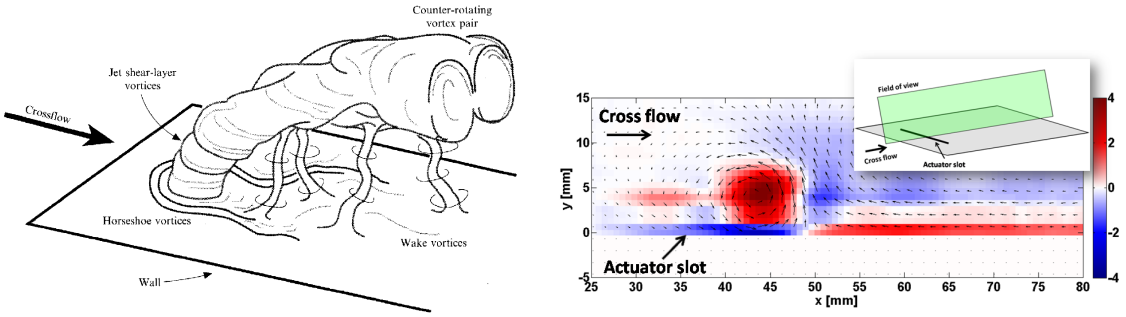

(a) Schematic drawing of the four types of vortical structure associated with the transverse jet[24]

(b) Two dimensional view of a vortex induced by a rectangular slot in cross flow.

Figure 2.7: Schematic draw of a radial jet in cross flow and the vorticity field of a slotted jet in cross flow

2.8(a). The horseshoe vortices result from a positive pressure gradient through which the boundary layer is separating, whereby the separation line depends on the velocity ratio. As Plesniak and Cusano [58] have shown, there are no wake vortices for a rectangle jet and also the induced vortices as well as the penetration depth is smaller compared to a radial jet.
Jet penetration and the mixing process can be enhanced by use of pulsed blowing. Recent experiments have shown that the jet penetration and the the spread can be maximized by using periodic excitation [70, 46, 20]. The shear layer vortices of a jet in cross flow as shown in Figure 2.8(b) can also be found during the blowing phase of the pulsed actuation. Nevertheless these are too small to trigger a momentum transfer, which is necessary to handle separation. However, by pulsed excitation large-scale vortices are also induced, which incite the instabilities of the shear layer.
Deploying a higher velocity ratio $VR = \frac{u_{jet}}{u_\infty} > 1$ and a lower jet angle (e.g. $\alpha_{jet} = 45\,°$) two effects can be used to overcome separation. With the lower jet angle the direct increase of the momentum of the separation area is supported as known for tangential blowing. The higher jet amplitude triggers the entrainment through shear layer. The jet separates at the edge of the slot and a counter-rotating vortex pair builds up [44]. The vortex pair is propagating downstream directly interacting with the shear layer of the separation. This results in a high momentum transfer vertical to the wall, implying a fluid entrainment

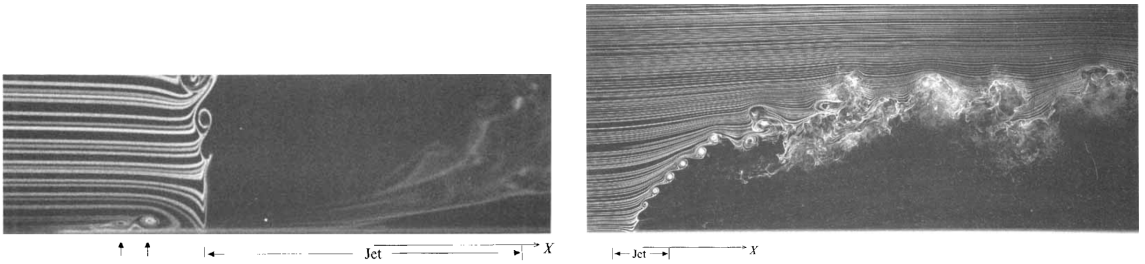

(a) Centreplane section showing two horseshoe vortices (indicated by arrows) upstream of a jet

(b) Smoke streamlines entrained into the leading edge of the jet

Figure 2.8: Shear layer and horseshoe vortices of a jet in cross flow [24]

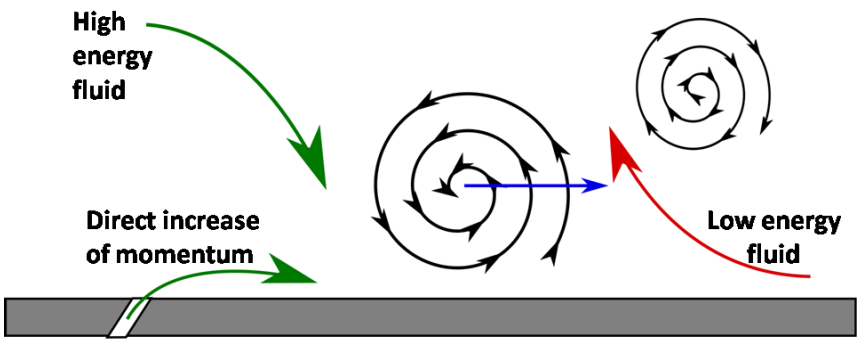

Figure 2.9: Schematic drawing of the mechanism affecting the reattachment process

through the shear layer. Through this entrainment high energy fluid is transferred to the wall whilst low energy fluid is transported away. A schematic drawing of this process is shown in Figure 2.9. The orientation of the jet determines the rotation and the symmetry of the vortex pair. Furthermore the mechanism of the separation control is depending on the jet angle. A $90\,^{\circ}$ jet related to the model surface, enhances the entrainment process by producing large-scale vortices. The lower the jet angle the higher is the increase of momentum in the separation area, because the jet adhere to the wall during the blowing phase.
The main objective of this thesis is to enhance the mechanism of shear layer entrainment by using a multiple cooperative system. In such a system the actuator slots must be deployed downstream behind each other to maximize the mechanism of the single actuator.

2.2.4 Existing multiple actuation systems

The idea of a system containing several rows of actuators was numerically investigated by Shmilovich and Yadlin [72, 73] on a simple hinge moveable element. They "mounted" five synthetic jets at equal intervals within the flap, between the hinge line and a section upstream of the trailing edge. The jet angle was rather low $\alpha_{jet} = 20\,^{\circ}$ relative to the flap surface. The flap was deflected to $\delta_{flap} = 25\,^{\circ}$, the angle of attack was set to $\alpha = 11\,^{\circ}$ at a Mach number of $Ma = 0.09$. The excitation of a single actuator was sinusoidal with an excitation frequency of $f = 217\,\mathrm{Hz}$. The momentum coefficient was $c_{\mu} = 0.03$, resulting in a velocity ratio of $VR = 2.5$. The overall excitation pattern was set to simultaneous actuation of every second port and with a phase shift of $\Theta = 180\,^{\circ}$ for the one in between (see Figure 2.10 lower right). The location and numbers of the ports are shown in Figure 2.10. The first case is shown in the upper left illustration of Figure 2.10. There the first port (port #1), located close to the hinge line where the separation originates, is active with a time-average overall lift improvement of $\Delta C_L = 0.65$. Moving the actuation downstream away from the separation line, the active separation control becomes more and more ineffective. This is shown in Figure 2.11. Here the graph with the open circles shows a single actuation of each port. The baseline results are included at the zero station. The lift as well as the lift to drag ratio decreases with the distance from the separation line. The flow field of the single actuation of port #3 is depicted in the upper right illustration of Figure 2.10. The largest lift increment can be achieved if blowing with all ports as shown

the lower right illustration of Figure 2.10. In this case the lift increment ($\Delta C_L = 1.36$) is nearly as high as this one of inviscid flow, which is stated with $\Delta C_L = 1.66$. On the other hand, with three actuators active the lift can be enhanced to $\Delta C_L = 1.05$, which is $88\,\%$ of the lift gained with all ports active. The overall results are shown in Figure 2.11. The filled circles indicate the adaptive actuation with every port active and the open squares that every other port is active. The authors could show that the ΔC_L and the L/D increases by increasing the number of active ports. The authors propose to properly place the single actuator, which suggests that the distance between the actuator slots and the excitation pattern have a close relationship.
An important point are the excitation amplitude or, in the case of synthetic jets, the energy consumption. This is set for all actuators as high as for the single actuation mode. This means in consequence that, with several actuators active, the total momentum coefficient (Equation 2.8)

$$c_{\mu,n} = \sum_{i=1}^{n} c_{\mu,i} \tag{2.8}$$

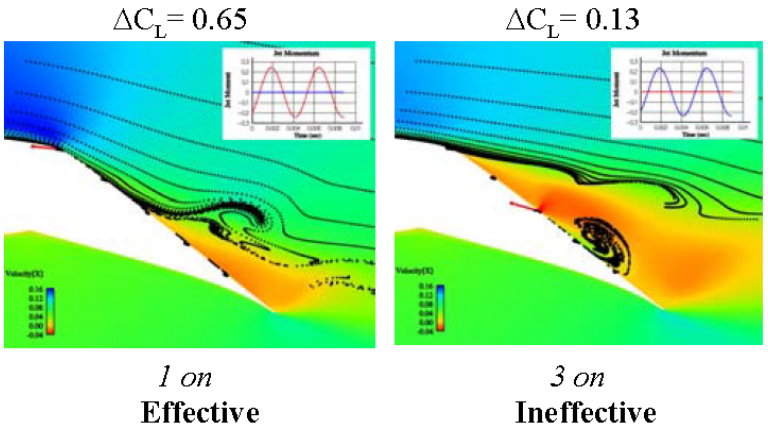

(a) Single actuation with different locations. Active actuators are given by the numbers.

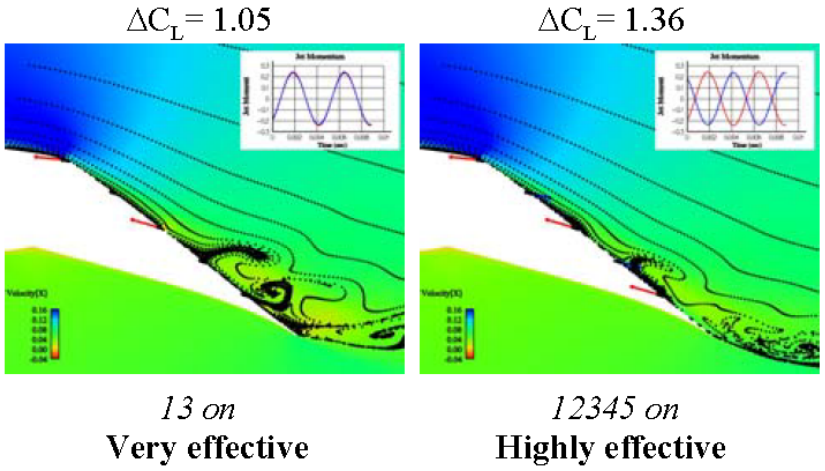

(b) Combined actuation. Active actuators are given by the numbers.

Figure 2.10: Flow structures for various actuation modes [73]

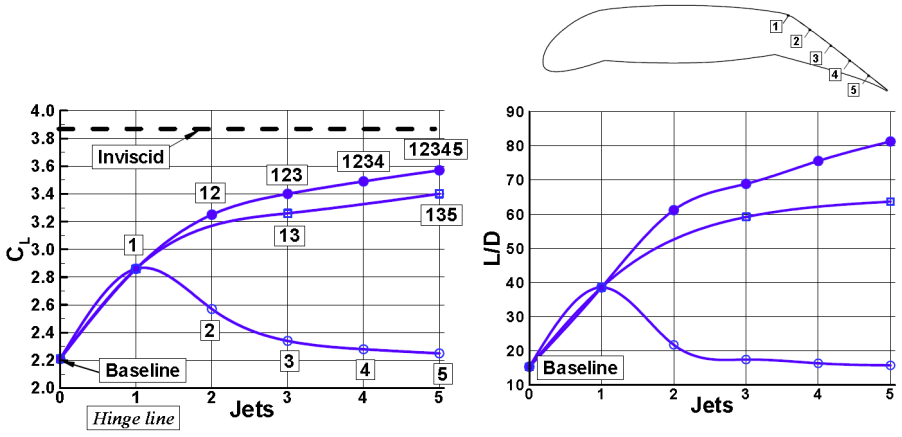

Figure 2.11: Buildup for distributed flow control at AoA $\alpha = 11\,^\circ$ [72]

is much higher than with a single actuator. The lift increment, however, does not increase in the same degree. Since synthetic jets are used, no external mass flow is required, but an alternate current input voltage. Therefore an actuator system with more actuators will increase the energy consumption.
Troshin and Seifert [82] investigated experimentally the performance recovery of a thick turbulent airfoil of a wind turbine by using a distributed closed-loop flow control system. In this experiment three rows of synthetic jet actuators were placed in equal intervals behind each other with an jet angle $\alpha_{jet} = 30°$ relative to the surface. The excitation frequency of the single actuator was $f = 1.35\,\mathrm{kHz}$ with an amplitude of an average peak velocity of $v_{jet} \approx 57\,\frac{\mathrm{m}}{\mathrm{s}}$. This leads to a momentum coefficient of $c_\mu \approx 0.04$. The airfoil was artificially tripped with "bugs" to simulate the degradation of the wind turbine. The experiments were executed with a Reynolds number of $Re = 0.5 \times 10^6$. The excitation pattern was similar to the numerical investigation of Shmilovich and Yadlin and was set to a phase shift of $\Theta = 180\,^\circ$ between the actuator rows. The efficiency is evaluated with Equation 2.9, called aerodynamic figure of merit, where values of $AFM3 > 1$ mean that it is energy efficient to introduce power to the actuators.

$$AFM3 \equiv \frac{[(L-D)\cdot U_\infty]_{Controlled} - 2\cdot P_{Elect}}{[(L-D)\cdot U_\infty]_{Baseline}} \tag{2.9}$$

In Figure 2.12 the overall system efficiency is shown with respect of the angle of attack. It is demonstrated that the performance of a contaminated airfoil, intended for the root section of a wind turbine blade, can be fully recovered and its energy harvesting capability is expected to be increased up to $60\,\%$ using distributed active flow control over a narrow incidence range [82]. However, the authors state that a closed loop is necessary to be efficient. In their investigation a single-input-single-output PID controller was used in a multiple-in-multiple-out configuration. The input was the estimated C_L and the amplitude of the actuator were controlled. The amplitude distributor was fed by the measured separation location to maximize the efficiency. Nevertheless the open loop case with high power consumption did reach the best performance (see Figure 2.12).
Since both investigations uses low jet angle (Shmilovich et al. $\alpha_{jet} = 20\,^\circ$ and Troshin et al. $\alpha_{jet} = 30\,^\circ$) obviously the active separation control works best with high amplitudes, because as Nagib et al. [52] states, the effectiveness increases with increasing velocity

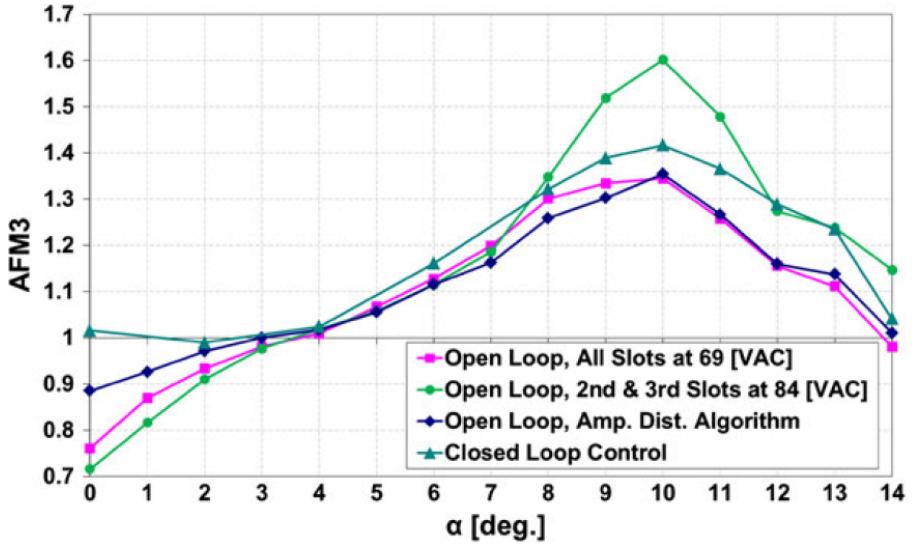

Figure 2.12: Overall system efficiency calculated with Equation 2.9 [82]

ratio for tangential blowing.
Since both of these systems reach considerable results, they are not using the entrainment through shear layer in a cooperative way. To reduce the energy, respectively the mass flow it is necessary to take the propagation velocity and therefore the phase shift into account. By doing so the vortex can be amplified or maintained over a longer distance, which increases the efficiency of such a system.

2.3 Objective and structure of this thesis

Pulsed actuation induces large-scale vortex structures, depending on jet angle, duty cycle and amplitude. These vortices trigger an exchange of fluid through the shear layer to reattach the separated region. The vortex structures grow with an increasing jet angle. Hecklau [32] states that, with a low jet angle $\alpha_{jet} \leq 30\,^{\circ}$, the induced vortex triggers only a short entrainment process vertical to the incident flow. The flow is then stabilized by the fluid transfer caused by the attachment of the jet to the wall. Therefore, a higher duty cycle with high amplitude is preferable, which in consequence increases the needed mass flow. A jet angle perpendicular to the wall can reduce the mass flow by inducing an impulse to the flow. Here only the vortex structure is responsible for the reattachment process. In consequence the duty cycle can be small ($\Lambda = 25\,\%$). However, a high duty cycle is disturbing the flow through building a fluid wall. Hence, the jet angle must be chosen by the boundaries of the application. A low jet angle is classified as robust but mass flow costly, while with a higher jet angle the vortex structures can be used to reduce the mass flow.
This knowledge can be used to build up a system which takes advantage of both mechanisms, the entrainment as well as the direct increase in momentum. To increase the momentum of the separated area a jet angle of $\alpha_{jet} = 45\,^{\circ}$ is chosen, to have the jet adhere to the wall but also inducing a proper vortex. The objective of this thesis is to reduce the energy,

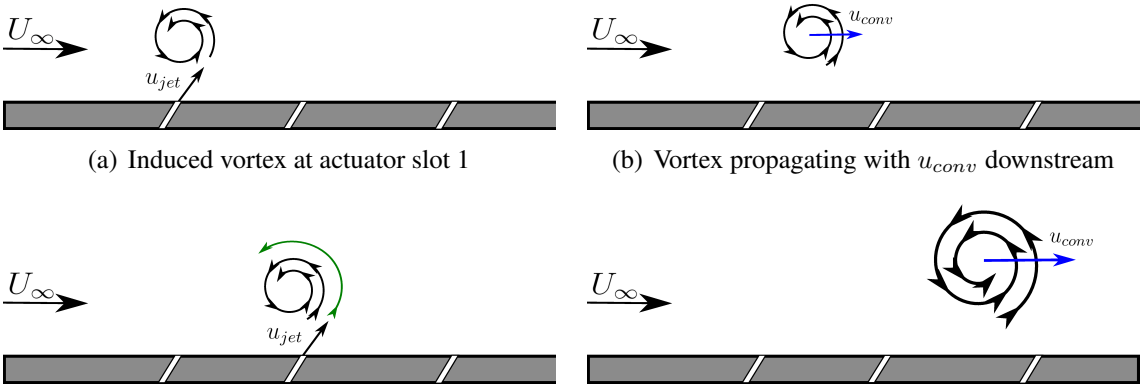

(a) Induced vortex at actuator slot 1

(b) Vortex propagating with u_{conv} downstream

(c) u_{jet} of second actuator merge with the vortex

(d) Strengthened and stabilized vortex propagating further downstream

Figure 2.13: Schematic drawing of vortex merging by cooperative actuation

respectively the mass flow by using a cooperative effect, enhancing the entrainment through the shear layer. Thereby, the responsible vortex is enhanced over a certain distance and the mass flow of the single actuator can be reduced significantly. According to the saying, the whole is grater then the sum of its parts, the overall mass flow is reduced by using this cooperative effect.
To enhance the vortex several parts must be considered. First a number of rows of actuators must be located downstream of each other with a certain distance. Second the mass flow must be adaptable and sensored. Last but not least the excitation of the actuators must be coordinated so that the vortices merge with each other.
Figure 2.13 shows a schematic drawing of the merging process. A vortex is induced by pulsed blowing of the first actuator (Figure 2.13(a)) and propagating downstream with the propagation velocity u_{conv} (Figure 2.13(b)). When the vortex reaches the second the slot, the blowing phase of this actuator starts, merging with propagating vortex (Figure 2.13(c)). Thereby the vortex is strengthened and stabilized. The now bigger vortex propagates further to the next slot (Figure 2.13(d)). Theoretically this process can be repeated more often.
The theory is just as simple as challenging the practical implementation. One key to success is a proper phase shift between the blowing phases of the actuators. The phase shift Θ is not only depending on the propagation velocity of the vortex and therefore the incident flow, but also from the distance of the actuator slots. Hence, an adaption of the wave length formula can be used to estimate the necessary phase shift (See Equation 2.10).

$$\Theta = \frac{d_{act} \cdot f_{act} \cdot 360\,^\circ}{u_{conv}} \tag{2.10}$$

The merging and interaction of vortices has been investigated for different settings like a counter-rotating vortex pair [12, 14] or co-rotating vortices [48, 42, 49]. These investigations address fundamental research or merging trailing edges of an aircraft. The propagation velocity is mostly opposite and fully built up at the time of merging. In the case of cooperating actuation, the aim is to merge the vortex with a newly induced one. Nevertheless, the merging of two vortices, generating at different times propagating in the same direction

has not been investigated yet. Therefore it is necessary to investigate the behavior of such a system. The results can then be taken to deploy a cooperative actuation system to reattach a pressure induced separation.
The main objective is to reduce the mass flow or, in the case of ZNMF actuators, to increase the aerodynamic figure of merit (2.9), by maintaining the flow attached to the surface. However, initially the merging parameter are investigated on a setup with no pressure gradient. Thereby, the main focus is on the induced vortices and how they interact with each other as well as the behavior of the surrounding flow. This has the advantage, that the boundary conditions remain the same and guarantee a direct comparability of different phase shifts. The second step is to transfer the setup and the first results obtained to a generic configuration, where a pressure gradient can be applied. This is done with a half diffuser where the separation line can be adjusted by changing the step angle α_{step}. This ensures that the flowmechanics of the merging and therefore the reattachment of the separation can be observed in isolation from changing boundary conditions like actuation influenced changing of the pressure distribution. Here the changes of the merging process are investigated, with the focus on the aerodynamic parameter. This is done in comparison to simultaneous blowing to highlight the advantages of cooperative distribution.
Following on from that the mass flow is reduced and varied over a significant range of phase shifts on the same setup. The efficiency of the system is rated with the pressure recovery Δc_p. Mainly the parameter of momentum c_μ and the phase shift are changed and compared to a single active row. With this configuration the potential of the distributed actuation to reattach flow with a lower velocity ratio and less mass flow is pointed out.
In the following section the measurement configurations, the used actuator system and control unit as well as the measurement setup including traditional and imaging measurement procedures are described. In section 4 the evaluation and used methods are presented. The flowing section provides the interaction of vortices without pressure gradient. First a look at a single vortex is described, followed by the merging process of vortices on a flat plate. This results are then transferred to an half diffuser where a pressure induced separation is deployed. The results of the interaction process is presented here. Subsequently a first comparison between the single and the cooperative actuation is done. Section 6 provides the benefits and discussion on the cooperative actuation with regard to the parameters VR, c_μ and mass flow as well as a recommendation to future work. Finally the conclusion completes this thesis.

3 Experiments and Methods

Two different test facilities were used two examine the cooperative actuation system. To understand the process of interacting vortices, the concept was first tested on a flat plate. Then it was transferred two a half diffuser, with an adjustable incline to generate a pressure induced separation.
The mechanism of the cooperative actuation was systematically investigated by means of different measurement techniques. The focus was on the laser optical investigation with Particle Image Velocimetry (PIV), to get a better insight in the flow behavior.
In this section the realization of the cooperative actuation concept, the used actuator system, the used measurement setup as well as both test facilities are presented.

3.1 Test facilities

The basic examinations were done at the LWK-2 located at Airbus Group Innovations in Munich. This facility is a Göttinger type wind tunnel, as shown in Figure 3.1, for basic subsonic measurements. The flow velocity range is adjustable up to $v_\infty = 37\,\frac{\mathrm{m}}{\mathrm{s}}$. This test section has a length of $L = 0.6\,\mathrm{m}$ and a square cross section of $h \times b = 0.09\,\mathrm{m}^2$. The grade of turbulence is between $0.5\,\% \leq Tu \leq 1\,\%$ referring to the inlet of the closed measurement test section. This test section also provides good optical access from the ceiling as well as from the sides, to perform PIV measurements. In addition a 3D Cartesian robot, mounted on the housing, enables exact flow investigations by means of a hot wire anemometer.
Three actuators are installed in the centre of the bottom plate of the test section. The first actuator slot has a distance of $d_{LE} = 0.3\,\mathrm{m}$, and the distance between the actuators is $d_{act} = 0.04\,\mathrm{m}$. Here, five hot film sensors were flush-mounted in between the rows and additional twelve hot film sensors were mounted behind the last row.
The investigations concerning the reattachment of the pressured induced separation were done at he GSW located at the Department of Aeronautics and Astronautics of the Berlin Institute of Technology. This wind tunnel is shown in Figure 3.2 and is also built as Göttinger type, for subsonic investigations. The flow velocity can be controlled up to $v_\infty = 30\,\frac{\mathrm{m}}{\mathrm{s}}$. Thanks to sieves and rectifiers this wind tunnel has a low grade of turbulence ($0.2\,\% \leq Tu \leq 0.6\,\%$). This facility provides a cooling circuit, so that the temperature is the same during the measurements. The incline step can be controlled with a step motion control unit and is adjustable between $0\,^\circ \leq \alpha_{step} \leq 25\,^\circ$. The section of measurements is designed to have optical access from above and from the side to allow optical measurements to take place. The positions of the hot wire anemometer are controlled by means of a 3D Cartesian robot unit.

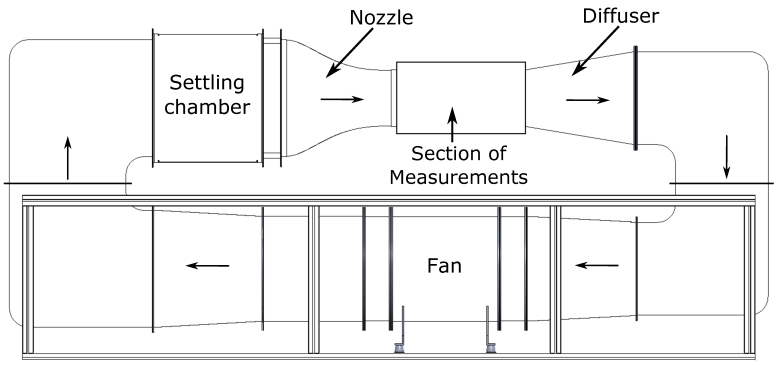

Figure 3.1: Wind tunnel OTN - LWK2

The incoming cross section is given by the section of measurements with $h_1 \times b = 0.237\,\mathrm{m}^2$. The length of the incline step is constant with $L_{step} = 0.34\,\mathrm{m}$. This means that the step height H and the outgoing cross section is a function of the step angle α_{step}. The base plate after the step is limiting the height h_2 at the end of the test section. Therefore the expansion ratio $ER = \frac{h_2}{h_1}$ is adjustable through the step angle. The incoming height $h_1 = 0.395\,\mathrm{m}$, the width of the section is $b = 0.6\,\mathrm{m}$ and the height h_2 for a step angle $\alpha_{step} = 23\,^\circ$ results in $h_2 = 0.53\,\mathrm{m}$. This leads to an expansion ratio of $ER = 1.34$ with a step height of $H = 0.133\,\mathrm{m}$.
The geometrical boundary conditions for the incline step are chosen too enable a specific positioning of the separation for selective step angles. The test section has secondary flow, but in the middle section, where the investigations took place, these flows are negligible [32]. For these investigations three rows with three actuators each were realized. A total of $40\,\%$ of the width is covered by the actuator slots. The actuators are flush-mounted to the surface with a distance of $d_{LE} = 0.034\,\mathrm{m}$ to the leading edge. The following rows have a distance of $d_{act} = 0.04\,\mathrm{m}$. Between and after the centered actuators wall mounted pressure transducers are implemented to monitor the pressure distribution and pressure recovery.

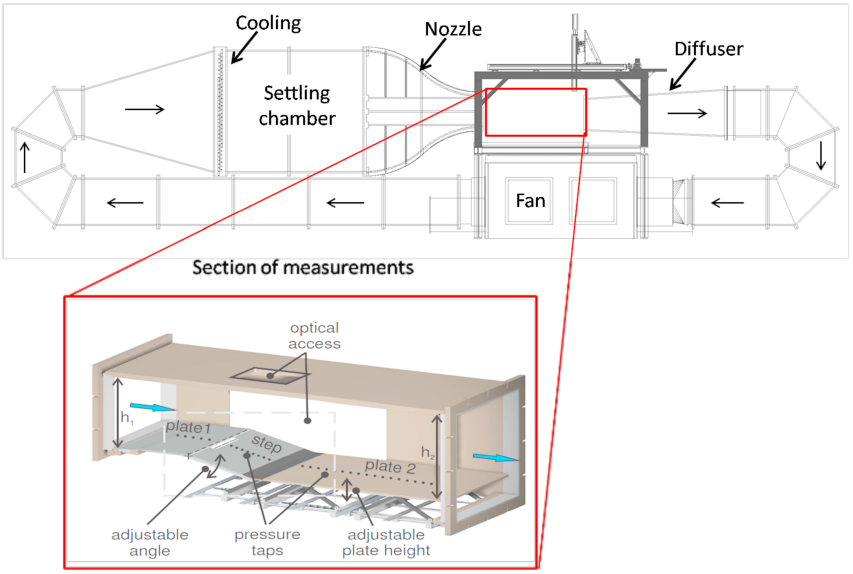

Figure 3.2: Wind tunnel TUB - GSW (after [32])

3.2 Actuator

Pulsed blowing through flush mounted slotted actuators has proven to be sufficient for active separation control. The slots are distinguished through a high aspect ratio transversely to the incident flow. This guarantees that a quasi two dimensional spanwise vortex is produced, interacting with the shear layer of the separation. Generally, for experimental investigations the slotted actuators are driven by a fast switching solenoid valve. The frequency and the duty cycle can be controlled, by means of a signal generator. The amplitude is adjusted with a pressure regulator and monitored with a volume or mass flow meter.
This setup is sufficient for the single actuator (row) setup. However, having several rows of actuators each row needs its own setup. Furthermore, to adjust the phase shift of excitation between the rows the signal generators have to communicate with each other. Therefore a Digital Signal Processing (DSP) rapid prototyping system was used to be able to adjust all parameters individually but keeping the dependence regarding the phase shift Θ. With the DSP it is also possible to control the amplitude by means of a PID control algorithm.
The cooperative actuation was realized as shown in Figure 3.3. Here the setup for the GSW is illustrated, but the insert, used in the LWK-2 is in principle the same. The difference between the two inserts is the used measurement techniques between and after the centered actuators. For the measurements on the flat plate hot film sensors are used, whereas on the incline step pressure sensors were wall mounted, as seen in Figure 3.3. The distance between the actuators is the nearest possible due to the fortifications to the insert. This is done due to the dissipative behavior of the vortex. This ensures, that it is possible to have an effective vortex interaction. Having this setup, a small addition has to be made concerning the dimensionless frequency F^+. The characteristic length l_{ref} between slot and trailing edge of the model is changing with every row and would therefore result in three different Strouhalnumbers. An example is given for the measurements done in the GSW. With a distance of $d_{act} = 40\,\mathrm{mm}$ the dimensionless frequency is decreasing with every actuator row (see Equation 3.2). To have the same frequency for all actuator rows, only the first one is set to a subharmonic of the characteristic length. The others are then the result of Equation 2.1.

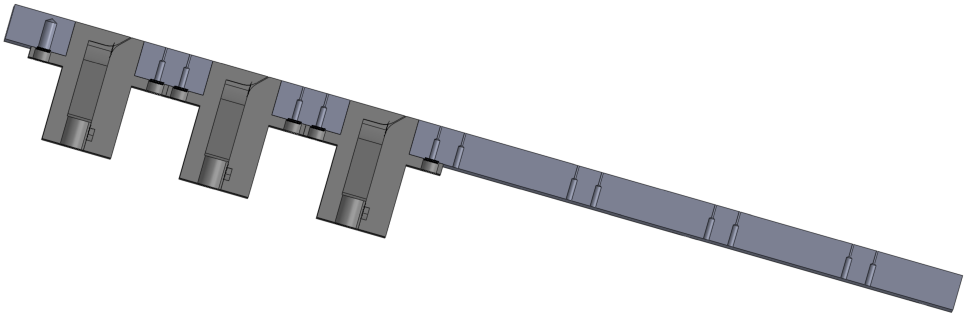

Figure 3.3: Section of used geometry

$$\begin{aligned} F_1^+ &= 2.0 \\ F_2^+ &= 1.7 \\ F_3^+ &= 1.4 \end{aligned} \tag{3.1}$$

For the cooperative actuation, generic slotted actuators are used within these investigations. The actuator is shown in Figure 3.4 (a). The inlet is radially symmetrical, whereas the outlet is rectangular. Two important factors have to be taken into account. A sharp increase of the velocity at the beginning of the blowing phase and a nearly rectangular velocity profile in spanwise direction. The volume of the actuator chamber is responsible for both behaviors. A high volume results in a rectangular velocity profile, but reduces the increase at the beginning of the blowing period. Therefore the chamber was adapted by experimental investigations to meet both criteria. The compromise is illustrated in Figure 3.4 (b). It provides also a high aspect ratio of $AR = 175$ resulting in a slot length of $l_{act} = 70\,\mathrm{mm}$ and a slot width of $b_{act} = 0.4\,\mathrm{mm}$. The jet angle of the actuator is set to $\alpha_{jet} = 45\,^\circ$. This angle is an ideal combination of the two mechanisms to reattach the separated flow. This guarantees that reasonable vortices are induced as well as the increase of momentum into the detached area. These parameters are called geometrical parameters and most of them may not be changed during the experiments.
The knowledge of the velocity distribution along the slot, the introduced momentum and the jet velocity are important. Therefore the actuator is calibrated by means of hot wire measurements. The actuator setup including the pressure regulator and the volume flow meter has to be built up outside of the wind tunnel. The hot wire is placed in the center of the actuator slot width and moved in small steps by a traverse along the slot. The hot wire was positioned very close to the actuator slot ($< 0.5\,\mathrm{mm}$). The resulting velocities are normalized and the distribution is shown in Figure 3.5 (a) as an example. The slot profile is nearly rectangular over the whole slot length, apart from the peak at the middle of the slot. This is due to the radial symmetrical inlet. Nevertheless this peak is smaller then $10\,\%$ of the mean velocity and can be neglected.
In Figure 3.5 (b) the normalized velocity over one period is illustrated. Additional measurements of the pressure within the actuator chamber took place with a wall mounted

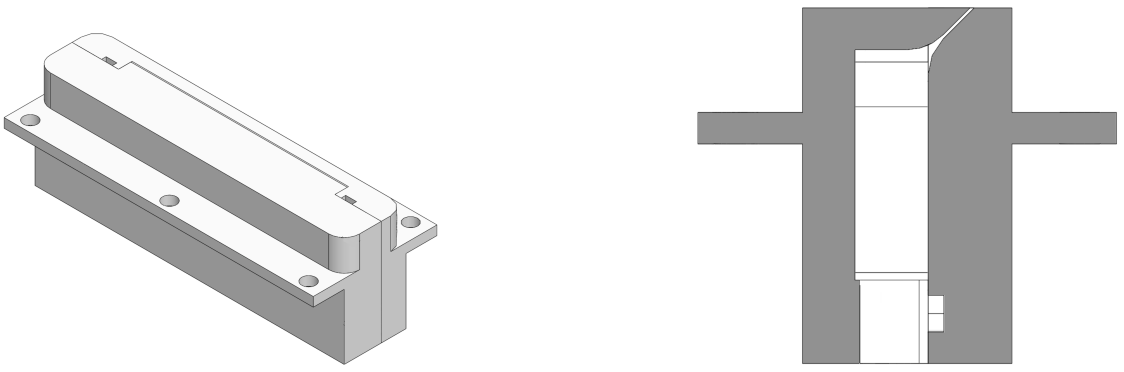

(a) Outside geometry (b) Inside geometry

Figure 3.4: Geometry of the actuator

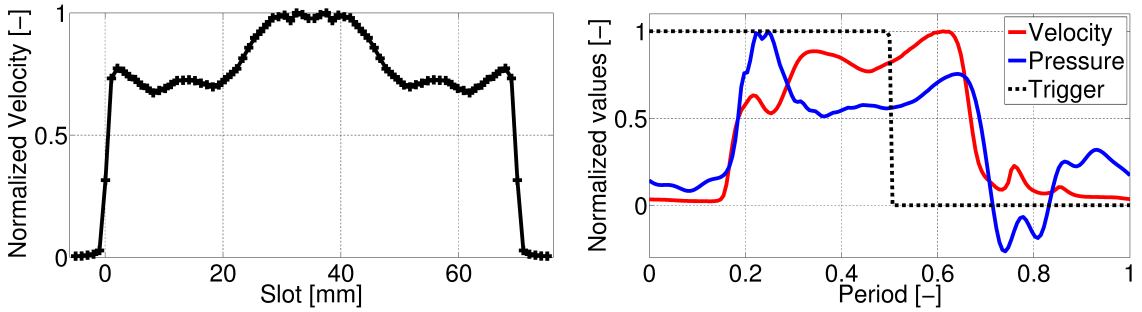

(a) Spanwise slot velocities

(b) Time depending slot velocities with trigger signal and pressure insight of the actuator

Figure 3.5: Velocity profiles of the actuator

transducer. As reference, the associated trigger signal is also plotted as a dashed line. The signals are phase-averaged over the period. The time delay of the rising edge of the pressure and hot wire signal is due to the switching time of the solenoid valve of $t_{switch} \approx 1.5ms$. A sudden rise in pressure occurs when the valve opens, resulting in a steep rising edge of the velocity. Then the actuator is nearly constantly blowing over the opening time of the valve. Afterwards, when the valve is closed, the remaining pressure evacuates the actuator chamber. The now accrued low pressure within the chamber result in a small suction phase where the chamber is refilled. This is illustrated by the pressure signal as well as the velocity peak behind the falling edge of the signal. Since the hot wire signal is unidirectional the velocity is also positive, but together with the pressure signal the statement is confirmed.

The jet velocity of the actuator can only be obtained outside the wind tunnel. To determine the velocity during the experiments a correlation between the permanent recorded volume flow and the jet velocity has to be done. Again hot wire measurements took place with an instantaneous measurement of the volume flow. Knowing the area of the slot, which is $A_{act} = 28\,\mathrm{mm}^2$, the velocity of the actuator at the slot plane can be computed with the continuity condition (see Equation 3.2). Thereby the duty cycle Λ has to be taken into account. Utilizing the continuity condition means that it is only valid for incompressible flows, which means that the Mach number is smaller $Ma < 0.3$. The velocities from the hot wire measurements are averaged over the blowing phase angle Φ of the period.

$$v_{Vol} = \frac{\dot{V}}{A_{act}} \cdot \frac{100}{\Lambda} \tag{3.2}$$

The result is shown in Figure 3.6 where the measured velocity is drawn over the velocity obtained from the continuity condition. The real velocity is about $\approx 20\,\%$ below the computed velocities. Nevertheless a linear correlation can be found and therefore the jet velocity can be determined by means of the volume flow meter values recorded during the wind tunnel experiments.

This correlation can be used to compute the different velocity ratio VR as stated in Equation 2.3. To compare the actuator with other experiments the root mean square of the velocity and the momentum coefficient is established (see Equation 2.5 and 2.7). In Figure 3.7 (a) the dependency of u_{RMS} on the mass flow is shown. The mass flow is instead of the volume flow is taken to compensate the influence of the density. The velocity increases

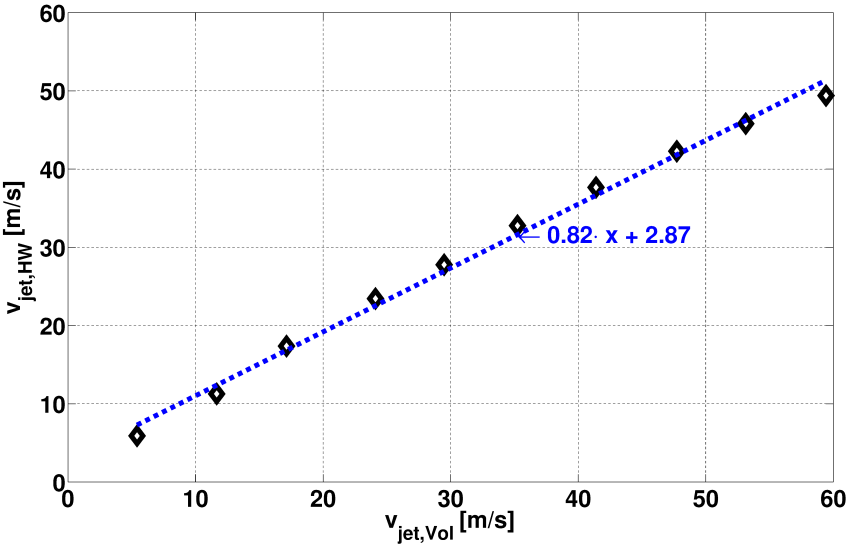

Figure 3.6: Correlation of continuity and hot wire velocities

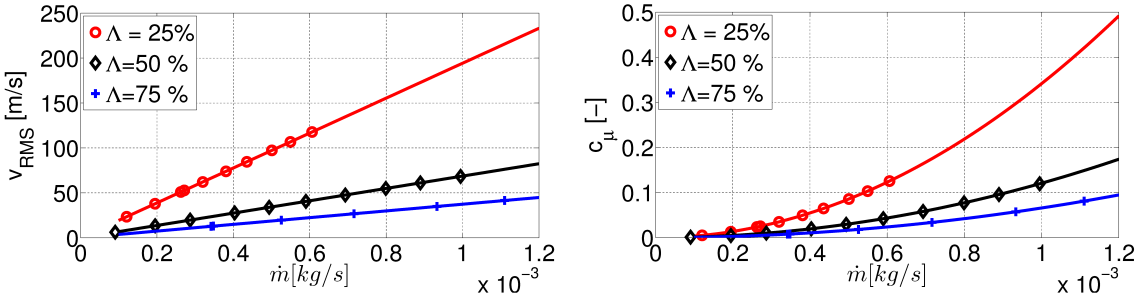

(a) Root Mean Square velocity over mass flow

(b) Momentum coefficient over mass flow

Figure 3.7: Characteristics of the actuator for the GWK at 100 Hz

linearly with the introduced mass flow. The duty cycle affects the RMS velocity. A small duty cycle, here of $\Lambda = 25\,\%$, means that the solenoid valve only opens for a quarter of the period and the mass flow rate decreases. Since the pressure is controlled by the pressure regulator, a lower duty cycle means a higher velocity at the same mass flow compared to a duty cycle of $\Lambda = 50\,\%$. Since the mass flow rate increases with the duty cycle, the gradient of the RMS velocity line decreases.
Utilizing the outcomes of correlation between the volume flow and the measured velocity the momentum coefficient can be computed in dependence of the duty cycle. This is done, as an example, for the wind tunnel of the Berlin Institute of Technology and illustrated on the right hand side of Figure 3.7.

3.3 Measurement setup

Figure 3.8 shows the schematic measurement chain used for all presented measurements. Originating from the measurement PC, the different signals of the transducers are recorded via the input channels. The regulating variables are transmitted to the corresponding control units via the output channels. The data acquisition and the step angle control are implemented in *LabView*. The signal generator implemented on the DSP is done in *Simulink* and controlled by software provided by the manufacturers.
The parameters of the signal generator, the frequency f, duty cycle Λ and the phase shift Θ are controlled with the measurement PC and transmitted to the DSP. This unit produces a rectangular trigger signal and transmit it to an amplifier, which provides the necessary voltage for the fast switching solenoid valves. Simultaneously the trigger signal is sent to the measurement PC. In addition the PID controller to adjust the volume flow is also implemented on the DSP. The volume flow is measured using the analogue-digital converter of the DSP and the corresponding voltage of the adjustment of the controller is sent to the pressure regulator. Therefore the excitation amplitude is controlled via the DSP system.
The complete pressure system consists of three identical rows with a pressure regulator, volume flow meter and a distributor when there are several actuators per row. This ensures that every actuator has the same amount of pressurized air and the desired volume flow is constant, due to the DSP controller.
The different sensors to measure the static and transient measurement values (MV) are recorded. The main parameters of the incident flow (temperature, dynamic and total pressure) as well as the values concerning the active flow control system (wall mounted pressure sensors, hot wire, hot film and volume flow) are converted by means of an analogue-digital converter. This data is then transmitted to the measurement PC. Beside the monitoring the external regulating variables can be controlled with the measurement

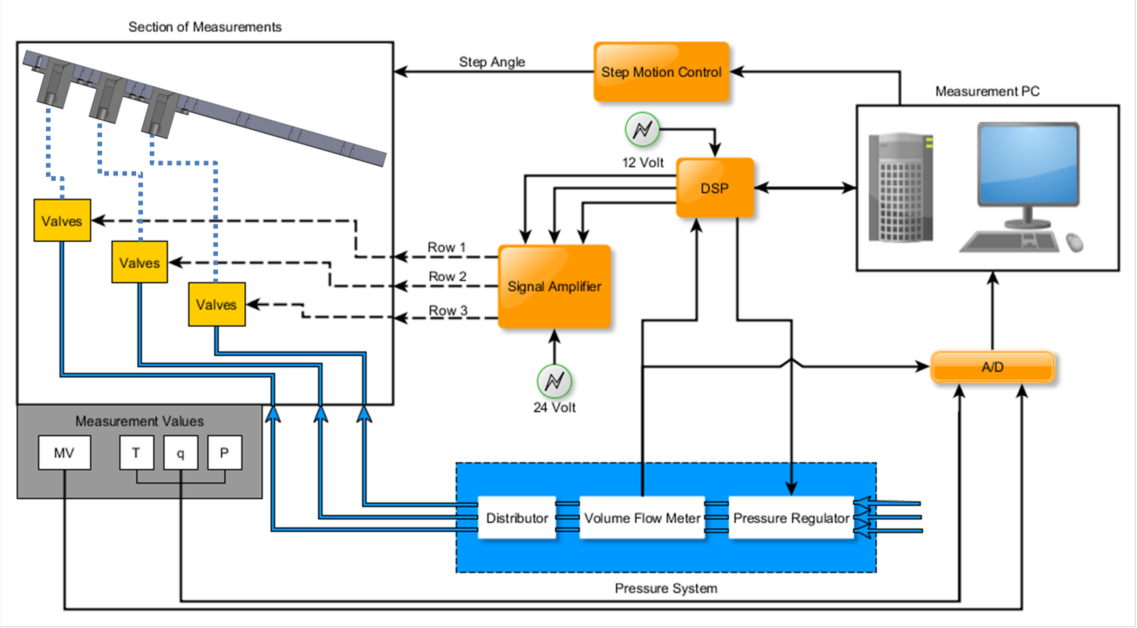

Figure 3.8: Measurement Chain

PC. For instance, the motion control unit to adjust the step angle or the position of the traverse.
The used measurement techniques to analyze and evaluate the reattachment process are described in the following sections.

3.3.1 Traditional measurement techniques

Different pressure transducer are used to measure the flow of the wind tunnel. The dynamic pressure q_∞ is measured with a Prandtl tube, utilizing a differential pressure transducer. The ambient pressure of the surrounding is received by means of a calibrated transducer. Including the temperature the density ρ_∞ can be computed utilizing the ideal gas equation, presuming incompressibility. With the dynamic pressure and the density the inlet velocity can be computed with Equation 3.3

$$u_\infty = \sqrt{\frac{2 \cdot q_\infty}{\rho_\infty}} \tag{3.3}$$

Despite the ambient pressure, which is a total pressure transducer, all used pressure sensors are differential pressure transducers. All sensors are piezoresistive and calibrated, transmitting a voltage proportional to the pressure. The analogue signal is converted with an analogue-digital converter and recorded for the evaluation.
The static pressure at a position x of the insert is obtained by means of a wall mounted pressure transducer. A sketch of such a setup is shown in Figure 3.9. The boundary layer hypothesis states that the static pressure is constant throughout the boundary layer and thus the static pressure of the flow is measured with this setup. The connecting hose between the transducer and the tube, connected with the wall, has to be short, to avoid a damping effect. Thus, it is guaranteed that the dynamic behavior can be analyzed. The transducers are mounted st the center of the surface of the insert at different locations (see Figure 3.3). The output of all sensors are recorded simultaneously.
To obtain the pressure coefficient c_p the transducer is connected to the static pressure of the incident flow p_{stat}. The voltage yielded by the sensor corresponds therefore to the difference $\Delta p = p_x - p_{stat}$. Taking the dynamic pressure into account, the pressure coefficient can be computed with Equation 3.4.

$$c_p = \frac{p_x - p_{stat}}{q_\infty} \tag{3.4}$$

Two thermoelectric measurement procedures were used to analyze the behavior of the active flow control system. The hot wire technique allows to measure the averaged as well as the fluctuation velocities of the flow field. The general principle is to overheat a small wire, bonded between two prongs, by means of a Wheatstone bridge. The overheat ratio is normally set to ≈ 1.7 above of the incident flow velocity. The resistance of the wire is changing, due to the convective heat emission to the fluid . The bridge is regulating this resistance by heating the wire. This method is called Constant Temperature Anemometer (CTA). The heating voltage is then used to measure the velocity. This relationship is given by King's law. Equation 3.5 expresses the relationship between heating voltage and flow

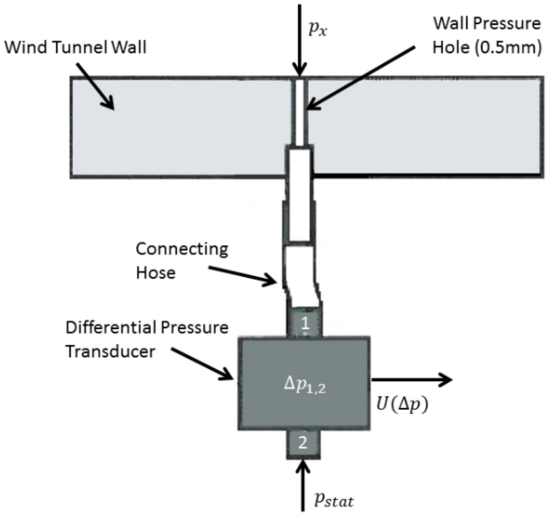

Figure 3.9: Sketch of Wall mounted pressure sensors, after [32]

velocity.

$$U^2 = A + B \cdot u^n \tag{3.5}$$

The constants A, B, n are obtained by means of a calibration. A single hot wire is unidirectional and therefore only one direction of velocity can be measured. To obtain more velocity components, a 2D or 3D hot wire probe is used.The effort of the calibration increases with the number of dimensions, due to the dependence of the wire on the direction. Since this a matter of thermoelectric measurements, the temperature of the measured fluid is an affecting factor, which has to be taken into account. The difference of the calibration temperature T_c and the fluid temperature T_f can be corrected with Equation 3.6 to obtain the actual heating voltage U_B. Presumed is the knowledge of the senor temperature T_s. A more detailed insight of the method and the thermal balance of the wire is given by Nitsche & Brunn [55].

$$U_B^2 = U_c^2 \cdot \frac{T_s - T_f}{T_s - T_c} \tag{3.6}$$

Another method used, also based on the constant temperature method, are hot film sensors. The hot film sensors can be used to measure the fluid friction on surfaces in a flow. In principle, the local shear stress is measured with a heated flush-mounted surface sensor. The sensor is electrically heated by means of a bridge, and the convective heat emission is measured. This value is proportional to the wall shear stress. The measurement principle is based on the Reynolds analogy between heat transfer and shear stress. The wall shear stress cannot be measured directly with this method, thereby the calibration is a important issue. Since the hot film sensors used for the measurements are uncalibrated only a short overview is given. A detailed overview is given by Nitsche & Brunn [55].
The relationship of the wall shear stress and the heating voltage is again shown by an empiric correlation as stated in Equation 3.5. As reference an appropriate measurement system has to be used, as example a mechanical shear stress balance. This method is very sensitive to temperature differences of the fluid and the wall. To protect the sensor from the wall temperature as well as to prevent the senor of heating the wall it is constructed on

a PVC foil.
The uncalibrated hot film sensors are therefore not capable of measuring the shear stress. Nevertheless, the 22 hot film sensors mounted subsequently downstream are measured simultaneously and thus a qualitative behavior can be analyzed. Due to its high cutoff frequency of $f_g = 50\,\mathrm{kHz}$ even high turbulence is measured.

3.3.2 Particle Image Velocimetry (PIV)

The particle image velocimetry is an image based measurement procedure and therefore is one of the non-intrusive measurements. The PIV captures the whole flow field within one plane during the considered measurement time. Three subsystems are mainly necessary for a PIV measurement. To visualize the flow field, tracers have to be supplied to the flow. A light sheet with high intensity to illuminate the tracers and a camera for optical imaging of these tracers.
The laser beam is extended to a quasi 2D plane in which the tracers are illuminated twice by short laser pulses. Two images are taken from the illuminated tracers within the lase pulse within a short period of time Δt. The correlation of these two images provides the displacement of the particles within the plane. The velocity is then computed with the known time delay $deltat$ between the light pulses. If the time delay is adequate the particle displacement is linear and the velocity remains constant.
Figure 3.10 briefly sketches the principle PIV setup used in the GSW. The laser beam is redirected and extended to a light sheet introduced through an optical access in the ceiling. This light sheet illuminates the tracers supplied to the flow twice. The lateral scattered light by the tracer particles is recorded on two single frames on a digital camera. The optical access for the camera is in the sidewall of the test section. The output is directly transferred to the memory of the computer.
To obtain the velocity out of the PIV recording the imagages are divided into small areas, called interrogation areas. The local displacement vector of the two images is determined

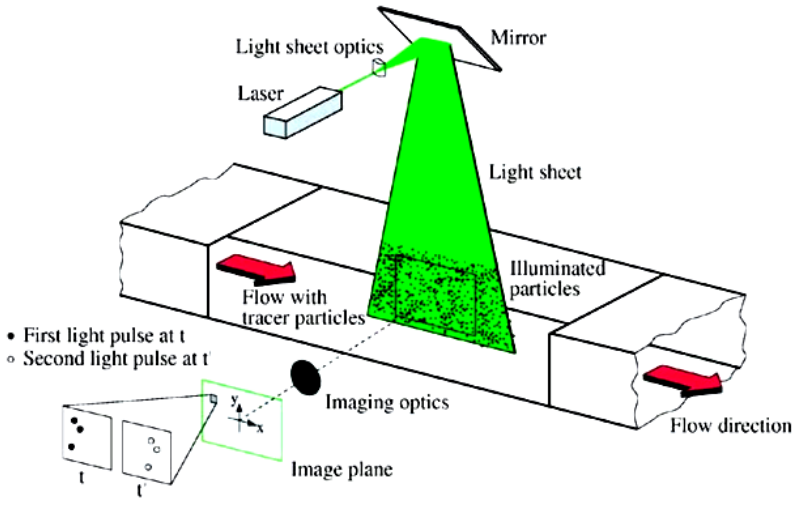

Figure 3.10: Principle 2D/2C PIV Setup, after DLR [18]

with respect to the short time delay Δt by means of the cross correlation function. This is based on the assumption that the particles have moved homogeneously between the two light laser pulses.The velocity vector is calculated on the bases of the known time delay and the magnification m of the images (see Equation 3.7).

$$\vec{u} = \frac{\Delta \vec{x}}{m \cdot \Delta t} \tag{3.7}$$

The seeding tracer can be any material reflecting or emitting light with a relativly constant particle size. The seeding normally used is Di-Ethyl-Hexyl-Sebacat (DEHS) which has a average diameter of $d_{DEHS} \approx 1\,\mu\mathrm{m}$. To supply the seeding to the flow a Laskin-nozzle can be used, where the seeding density and the size can be adjusted by a pressure regulator. Generally the scattering of the light by the particles is a function of the ratio of the refractive index of the particle to the surrounding medium, the size, shape and orientation [62]. In cases of spherical shaped particles, which are larger then the wavelength of the light, Mie's scattering theory can be applied. Another point concerning the tracer particles are the density of seeding within the flow. A high density can result in a speckle pattern, where the single particles are hardly detected. In this case further post processing has to take place. If the density is very low, it is referred to as particle tracking method. A homogeneous density is preferred for PIV measurements.
As a light source to illuminate the seeding, lasers are commonly used due to their ability to emit monochromatic light with a high energy density. The laser beam can be bundled, redirected and extended to thin light sheets, illuminating the tracer particles without chromatic abbreviations. Mostly double pulse lasers are used. The repetition rate per cavity of the laser beams gives the maximum sample frequencies. A detailed overview of the working principle of a laser is given by Raffel et al. [62]. The light sheet is extended by at least one cylindrical lens to achieve an appropriate thin light sheet. If a ND:YAG laser is used at least one additional lens has to be used to focus the light sheet.
Most common digital cameras are used for the optical imaging, which enable to obtain an image pair with a short time delay up to $\Delta t = 2\,\mu\mathrm{s}$. The standard PIV cameras have a Charged Coupled Device (CCD) chip and provides a sample rate of $F_s = 10\,\mathrm{Hz}$ regarding the double frame capture mode. The rapid progress in chip technology and the peripherals bring an increase in capabilities. Nowadays, more and more high speed cameras are used for time resolved PIV measurements (TR-PIV). These cameras are provided with a Complementary Metal Oxide Semiconductor as an imaging sensor and enable a sampling frequency up to $F_s = 10\,\mathrm{kHz}$. The images are stored in an internal memory, which also limits the maximum amount of single images.
Since a complete and detailed mathematical description is given by Westerweel [84] only a brief description is presented here. The obtained image pair is subdivided into small areas, the so called interrogation areas of the length $K \times L$. The particle displacement of every interrogation area is determined with a discrete cross correlation of the intensity values I_1 and I_2 of the particle images obtained at the times t_1 and t_2.

$$R_{II}(x,y) = \sum_{i=-K/2}^{K/2} \sum_{i=-L/2}^{L/2} I_1(i,j) I_2(i+x, j+y) \tag{3.8}$$

The displacement vector is given by the displacement of the maximum correlation peak $R_I I$. The cross correlation is capable of determining the displacement vector within ± 0.5

pixels. This can be improved by using an appropriate function like the three point Gauss peakfit. The velocity vector can be calculated, by means of the magnification and the known time delay between the image pair. To identify false vectors, several filters are commonly used. A brief description of the most important is given. The Local Filter calculates the difference of a velocity vector and its neighboring vectors. If the deviation is too high it is marked as an outlier. The Window Filter takes the magnitude and direction of all velocity vectors and plot them in a scatter diagram. Vectors which are inside of a given area, are marked as valid. The Signal-to Noise Filter is a filter which rates the quality of the correlation peak. Correlation peaks, which fall below a certain value, are also marked as outliers.
There are a lot of other factors, which have to considered, to obtain a high quality PIV measurement result. These factors as well as demanding methods to interpolate outliers are given by Raffel et al.[62] and Westerweel[84].

4 Evaluation and Tracking

To obtain useful information from the experiments key parameters and different evaluation methods are of great interest. In this part the focus will be on the evaluation criteria to rate the alignment of coherent structures in the flow and a tracking algorithm to detect and track vortices in the flow.

4.1 Flow characterization and key parameters

For the evaluation of the data acquired through the different measurement techniques, mentioned in the section above, to obtain the state of the flow in the wind tunnel and the interaction of the jet and vortices with the flow, several methods and parameters are known. The instantaneous velocity of a two dimensional measurement $u(t)$ and $v(t)$ is the composition of the time depending mean value and the superimposed fluctuation velocity [55]. This is shown in Eqaution 4.1 by the example of the velocity component $u(t)$, but is also valid in terms of a pressure signal and the uncalibrated hot film data.

$$u(t) = \bar{u} + u'(t) \tag{4.1}$$

whereby:

$u(t)$	–	instanteneous velocity,
$\bar{u}$	–	mean velocity,
$u'(t)$	–	fluctuation part.

This decomposition is done with a temporally discrete signal, which means that the signal consists of n single values obtained with a sampling frequency F_s. The values are therefore separated with the reciprocal of this frequency. Equation 4.2 shows the arithmetic mean value obtained from the single values u_i and the amount of values n. The mean value is a location parameter and describes the average of a distribution. To avoid a dependency of the mean value on the duration of the time interval, the duration of the signal has to be long enough, especially for periodic signals.

$$\bar{u} = \frac{1}{n} \sum_{i=1}^{n} u_i \tag{4.2}$$

Another location parameter is the median (Equation 4.3). The definition considers the median to be the 50th percentile of a distribution of numbers ranked in order of increase. In other words, the median represents the central value of an ordered series of uneven

numbers or the average of the two central values of an ordered series of even numbers [21]. The main difference to the mean value is the robustness against outliers.

$$\tilde{u} = \begin{cases} x_{\frac{n+1}{2}}, & \text{for n uneven} \\ \frac{1}{2}\left(x_{\frac{n}{2}} + x_{\frac{n}{2}+1}\right), & \text{for n even} \end{cases} \tag{4.3}$$

The parameter of the standard deviation σ_x describes the scattering of random variables around their expected value. In this case, it is the scattering of the measured values around the mean value. The standard deviation refers to the fluctuation part of the signal and is defined in Equation 4.4. This value is a measure of the intensity of the fluctuation, since the fluctuation part is considered square.

$$\sigma_u = \sqrt{\bar{u'^2}} = \sqrt{\frac{1}{n}\sum_{i=1}^{n}\left(u_i - \bar{u}\right)^2} \tag{4.4}$$

The Root Mean Square (RMS) is the result of the square root of the squared overall signal and is referred to as the mean squared deviation (see Equation 4.5) [55]. Therefore, the affecting time averaged effective value can be obtained. In case of pulsed blowing the RMS value shows the effective velocity induced by the jet over time. In the case of the hot film sensors, when only the fluctuation part is measured, the RMS value is equal to the standard deviation.

$$u_{RMS} = \sqrt{\frac{1}{n}\sum_{i=1}^{n} u_i^2} \tag{4.5}$$

In cases where an instantaneous measuring of all flow characteristics in a flow field is not possible, e.g. hot wire measurements, the phase averaging is a possibility, at least for periodic flow structures (see Equation 4.6). The phase locked mean value is determined from the single values obtained at a locked phase angle Θ of the signal. The number N_Θ is given by the amount of phase angles for which a certain number of single values exist. A reference signal has to be used to which the periodic signal is related. The frequency of the reference signal determines thereby which periodic parts are admitted. Every periodic share of the signal which are not in coherence with the reference frequency or their harmonics are damped (see Figure 4.1).

$$\langle u \rangle_\Theta = \frac{1}{N_\Theta}\sum_{i=1}^{N_\Theta} u_{\Theta,i} \tag{4.6}$$

In the case of pulsed blowing several single measurements can be related to a single reference signal measured at the same time and assembled to a flow field. As a result, the periodic shares of a flow field can be shown over one period. This is shown by way of example of two dimensional hot wire measurements on a flat plate with periodic actuation on a flat plate in Figure 4.2. In this case the fluctuation velocity of the flow field is shown to highlight the vortex.

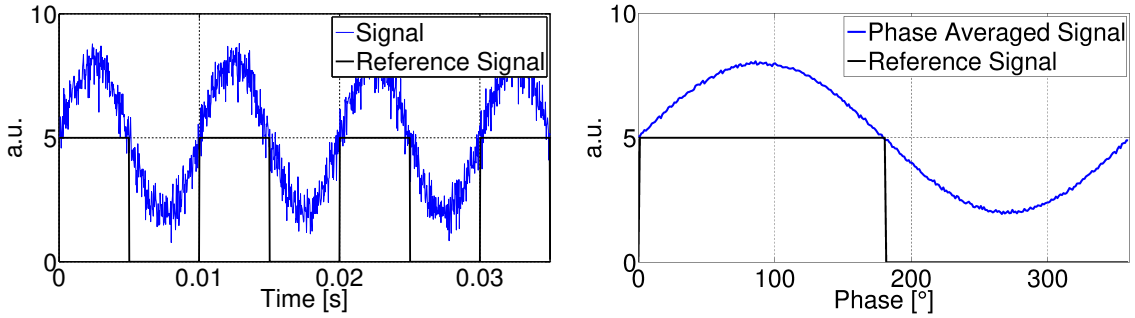

(a) Signal with reference signal over time

(b) Phase averaged signal over phase

Figure 4.1: Principle of phase averaging

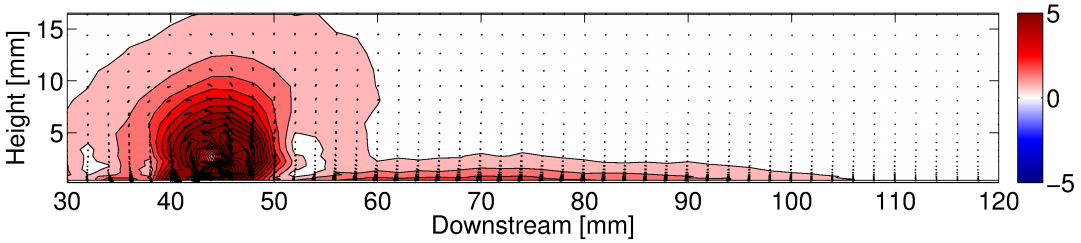

(a) Vortex at phase angle $\Theta = 124\,°$

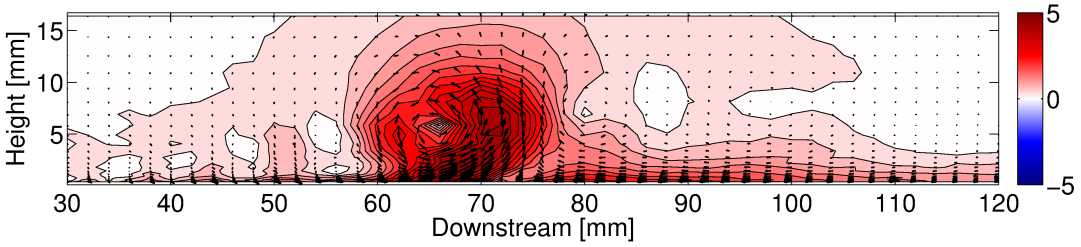

(b) Vortex at phase angle $\Theta = 179\,°$

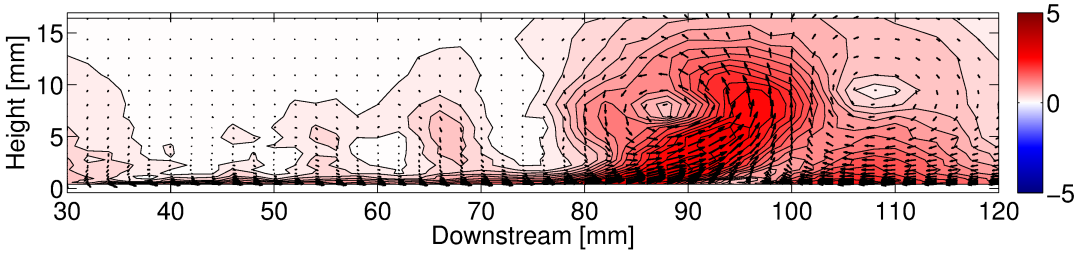

(c) Vortex at phase angle $\Theta = 234\,°$

Figure 4.2: Assembled flow field of two dimensional hot wire measurements (1342 single measurement points) for different phase angles

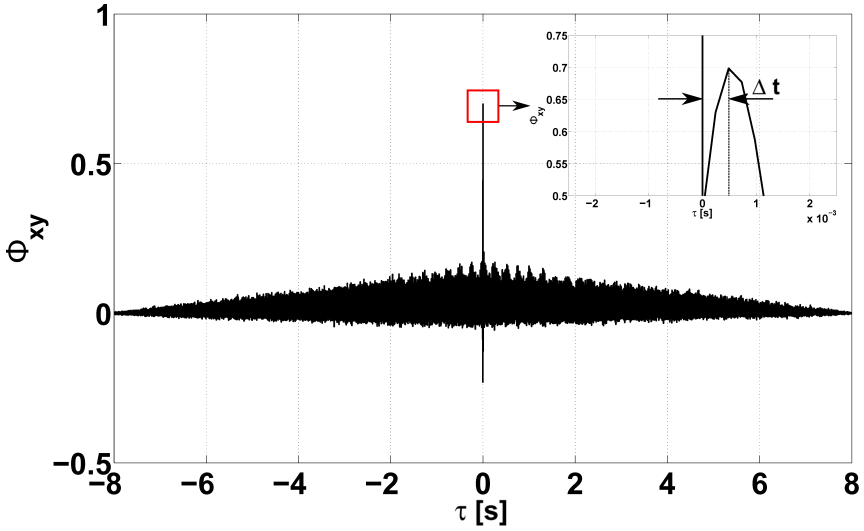

Figure 4.3: Cross correlation of two hot film sensor signals with characteristic time delay Δt (after [55])

Two signals are compared in the time domain by using correlation functions, which examine the similarities of the signals. The similarities of two different signals are detected by way of cross correlation (see Equation 4.7). The amplitudes of the signals are multiplied and integrated taking into account an increasing time delay [55].

$$\Phi_\tau = \int_{-\infty}^{\infty} x\,(t)\,y\,(t+\tau)dt \tag{4.7}$$

For the correlation of discrete time signals the sum function is used whereby $n \equiv t$ and $k \equiv tau$. In Equation 4.8 the cross correlation is normed, which means that if for any k the value is one, the signals are similar and for minus one the signals are in phase opposition.

$$\Phi_{xy} = \frac{\sum_{n=1}^{N} x_n y_{n-k}}{\sqrt{\sum_{i=1}^{N} x_i^2 \cdot \sum_{i=1}^{N} y_{i-k}^2}} \tag{4.8}$$

By amplifying similar and damping dissimilar parts, signal characteristics can be obtained from the time delay. In the case of hot film measurements the propagation velocity of a flow structure e.g. vortex, can be calculated. Figure 4.3 shows a cross correlation for two hot film sensors with pulsed actuation. With the known distance of the sensors and the obtained time delay Δt, the propagation velocity of the flow structure can be calculated. The parameter vorticity is a measure for strength of a vortex within a velocity field and is a significant value of fluid mechanics. It is a pseudovector field describing the local spinning of the flow around a point. In other words, it is the tendency of a fluid flow to cause rotation. Mathematically the vorticity is defined as curl or rotation of a vector field $\vec{v}$ and is shown for a two dimensional case in Equation 4.9.

$$\vec{\omega} = \nabla \times \vec{v} = \left(\frac{\partial v_y}{\partial x} - \frac{\partial v_x}{\partial y} \right) \vec{z} \tag{4.9}$$

Regarding PIV data, where the two dimensional velocity vector field is evenly spaced and the velocity data is disturbed by noise, a finite difference schema has to be applied to

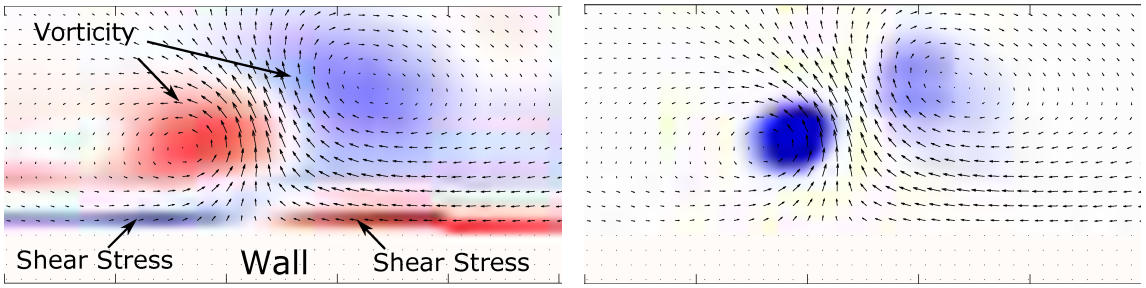

(a) Vorticity of a flow field with clockwise (blue) and counterclockwise (red) rotating vortices

(b) λ_2 criteria for the flow field depicted in (a)

Figure 4.4: Vorticity and λ_2 criteria for the same flow field with two vortices

calculate the vorticity [62]. In this case the central difference schema is used, assuming that the measurement uncertainties are independent of their neighbors. This assumption is valid, since the PIV images are not oversampled and have a high image density with small displacement gradients. Nevertheless the vorticity field indicates the presence of a vortices, but tends to be very noisy, which makes the identification of vortex centers difficult. Moreover, the vorticity also identifies shear stress as a vortex as shown in Figure 4.4(a).
To overcome this, the λ_2 operator is a useful method for the position estimation of vortices (see Figure 4.4(b)). Unfortunately the λ_2 criteria does not provide any information about the amplitude or direction of the vortex itself. But once the position is known other parameters can be calculated to obtain the relevant information. To detect vortices, Vollmers [83] stated that vortices appear for non-real eigenvalues of the gradient tensor G (Equation 4.10).

$$G = \frac{d\mathbf{U}}{d\mathbf{x}} = \begin{bmatrix} \frac{\partial U}{\partial X} & \frac{\partial V}{\partial X} \\ \frac{\partial U}{\partial Y} & \frac{\partial V}{\partial Y} \end{bmatrix} \tag{4.10}$$

To separate vortices from other patterns the discriminant λ_2 of non-real eigenvalues is calculated (Equation 4.11). Vortices are located at areas of negative λ_2 values.

$$\lambda_2 = \left(\frac{\partial U}{\partial X} + \frac{\partial V}{\partial Y}\right)^2 - 4\left(\frac{\partial U}{\partial X} \cdot \frac{\partial V}{\partial Y} - \frac{\partial U}{\partial Y} \cdot \frac{\partial V}{\partial X}\right) \tag{4.11}$$

The Equation 4.11 is restricted to two-dimensional flow fields and can be extended for three-dimensional vortex detection if the full three-dimensional tensor is available. False detection can occur at two-dimensional interpretation of flows if the overall flow is highly three-dimensional [62].

4.2 Alignment of multiple coherent structures in the flow

The interaction of vortices induced at different times and locations can be seen as alignment of multiple coherent structures. To rate these structures several methods are used. One is to look at the vertical velocities with regard to the incident flow. A vortex is characterized not only by its vorticity, but also by velocities vertical to the flow.
In Figure 4.5(a) the simultaneous blowing of three actuators are shown. Therefore three nearly identical vortices are induced propagating downstream. In the illustration on the right hand side, the three actuators are cooperating with each other producing one big vortex. Since this data is obtained by a phase averaging (Equation 4.6) the vortex at the end of the flow field ($x \approx 150\,\mathrm{mm}$) is the squeal of the vortex induced in the front. The velocities give a first hint of the effectiveness of the cooperative actuation. One might think that the effectiveness is depending on the phase shift of blowing. To rate the alignment of the structures the common computer vision algorithm RANSAC is used. This algorithm is used for fitting a model to experimental data. To overcome the drawback of the least square method, where outliers are changing the fitted model, the data points are assessed and therefore smoothed [22, 81]. In this case the alignment of the footprints left by the vortices over time are rated by calculating the deviation from a linear fit. The outcomes yields phase shifts Θ for best alignment.
The vertical component of the velocity as shown in Figure 4.5 is extracted in slices as seen in the illustration on the left hand side of Figure 4.6(a). To obtain the relevant velocities, only those which are twice above the standard deviation are taken into account (see Figure 4.6, center). The illustration on the right hand side of Figure 4.6 shows the outcome of the RANSAC algorithm. The sequel of the vortex, caused by the phase averaging as seen on the lower right edge of the illustration, would falsify the result. Therefore, the algorithm declares them as outliers, before fitting a linear line to the data. The square fitted error for that linear line in cartesian coordinates is estimated and the mean value of the error is taken as measure for the alignment. This means the better the alignment, the smaller the estimated error. Since the average deviance of the velocity for small phase shift deviations is only little, slices throughout the cross section of the vortices are analyzed to validate the results.

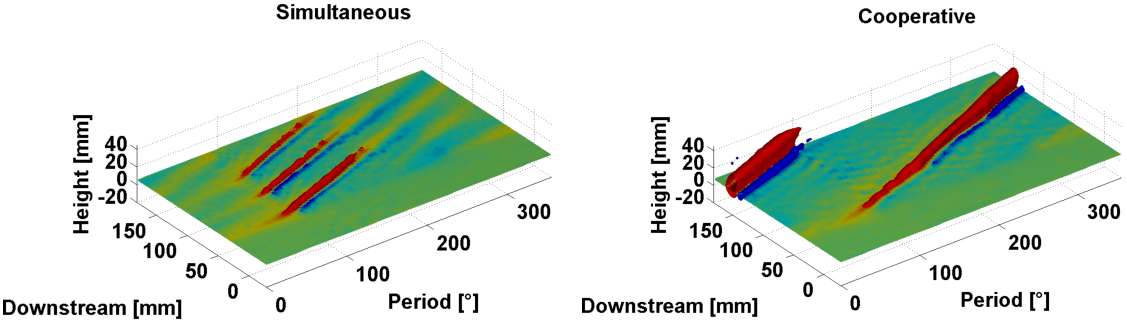

(a) Vertical velocities of simultaneous blowing (b) Vertical velocities of cooperative blowing

Figure 4.5: Isosurfaces of blowing with different phase shifts (red $+2\,\frac{\mathrm{m}}{\mathrm{s}}$, blue $-2\,\frac{\mathrm{m}}{\mathrm{s}}$)

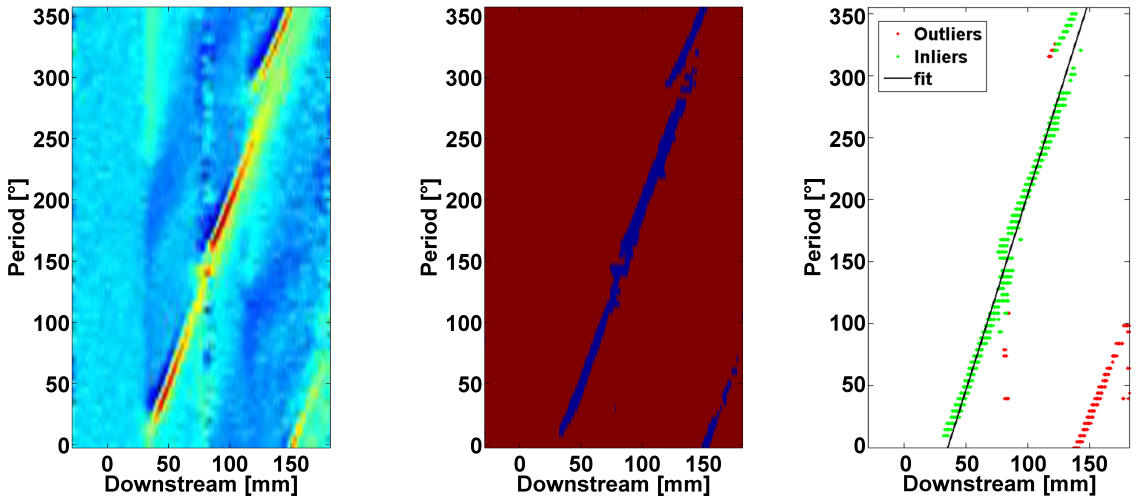

Figure 4.6: Example of real (left) and relevant (middle) velocities of one slice and the fitted line of the RANSAC algorithm (right)

The RANSAC algorithm can therefore be used to find the phase shifts which provides the best alignment of separate induced vortices over time. With the least deviation the probability of constructive vortex interaction, and therefore an amplification of the mechanism of reattachment, is increasing. Nevertheless it does not provide any information about the amplification and duration of vortices or about the shear layer entrainment.

4.3 Vortex detection and tracking

The alignment of vortices provide an estimation of the best phase shift, but to evaluate the physical behavior of the flow field the vortices have to be found and classified towards their impact on the reattachment process. There are a lot of detection methods, like $Lanbda_2$ Method [40], Eigenvector Method [75] or Streamline Method [59] which are summarized by Johnson and Hansen [31].
A simple but effective method to identify the core center of a vortex is presented by Holmén. The idea is to identify the vortex directly from the velocity field information by looking at the signs of the velocity. The direction of the flow around a center of rotation will have opposite signs on either side of the vortex [37]. The search algorithm proceeds in several steps. The first step is to carry out a signum operation at every point of the flow field. To identify a vortex, the four points around one point are selected and the sign of the velocity is considered. The point belongs to a vortex center if the sum of the signs of the normal velocity of the two horizontal points and the sign of the tangential velocities of the vertical points is zero (see Equation 4.12 relating to Figure 4.7(a)).
Since this criteria is also true for shear stress another check has to be made. This is done by considering only the signs of the normal velocity of the left point and the tangential velocity of the upper point (see Equation 4.13). In this case the sum of the signs must not be zero. Otherwise the considered point is discarded.

$$sign\left(v_{left}\right) + sign\left(v_{right}\right) + sign\left(u_{up}\right) + sign\left(u_{down}\right) = 0 \tag{4.12}$$

and

$$sign\left(v_{left}\right) + sign\left(u_{up}\right) \neq 0 \tag{4.13}$$

This criteria usually finds several vortex centers within one vortex. In the case of various centers, the Mean Shift algorithm finds the individual center of the vortex. The strength of this algorithm is that the center of several vortices in a flow field can be found simultaneously. In contrast to other clustering methods, there are no embedded assumptions of the shape of the distribution or the number of clusters.
In general this algorithm treats the points as an empirical probability density function where dense regions correspond to the local maxima of the distribution. An iterative optimization method, the gradient ascend method, is used on the local density until it converges. Any point associated with the stationary points of this method are considered as members of the same cluster [17]. For further and mathematical details refer to Cheng [9] and Comaniciu and Meer [11].
In Figure 4.7(b) the detected core centers (marked as circles) and the center of the vortex (marked as star) are shown. It can be seen that the center found matches the real center of this vortex. But to be sure a last check is done. To finally pass the detection method as vortex the center found has to match the λ_2 criteria. Due to the speed and robustness of this detection method it is suited for a large amount of data as found by PIV recordings.
Now that the center is found, the dimensions of the vortex can be computed using the vorticity ω. The idea is that the vorticity around a vortex center is following a Gauss distribution with the maximum located at the center. This assumption must be true for the horizontal as well as for the vertical part of the vortex. In Figure 4.8 the vorticity of a nearly circular shaped vortex is shown in length (a) and height (b). The radius of a single vortex can now be extracted using the corners of the vorticity distribution and with the formula of the circle $f(x) = y_m \pm \sqrt{r^2 - (x - x_m)^2}$ the edges of the vortex are given. It can be also seen in Figure 4.8 that even for this simple vortex the base diameter of the horizontal is slightly larger than for the vertical distribution. This difference is greater for complex flow conditions, like near wall vortex pairs or vortex interaction. The mismatch

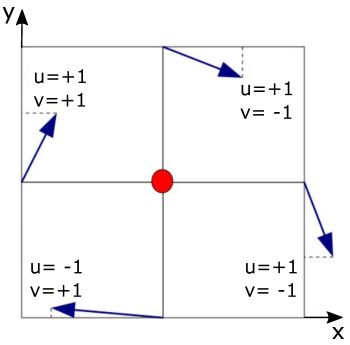

(a) Working principle of the algorithm. The numbers represent the sign of the velocities. (after [37])

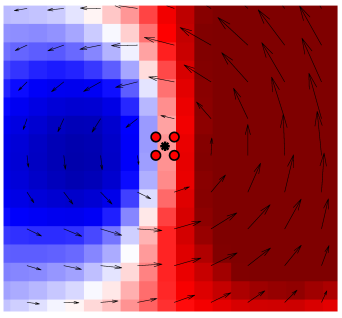

(b) Detected vortex core centers (circles) and result of MeanShift algorithm (star)

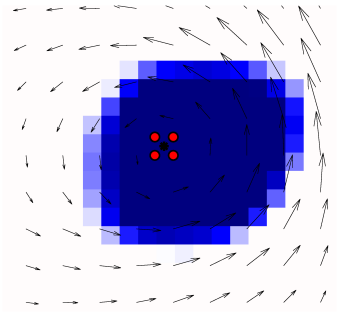

(c) λ_2 criteria for the vortex shown in Figure 4.7 (b)

Figure 4.7: Single steps of vortex detection

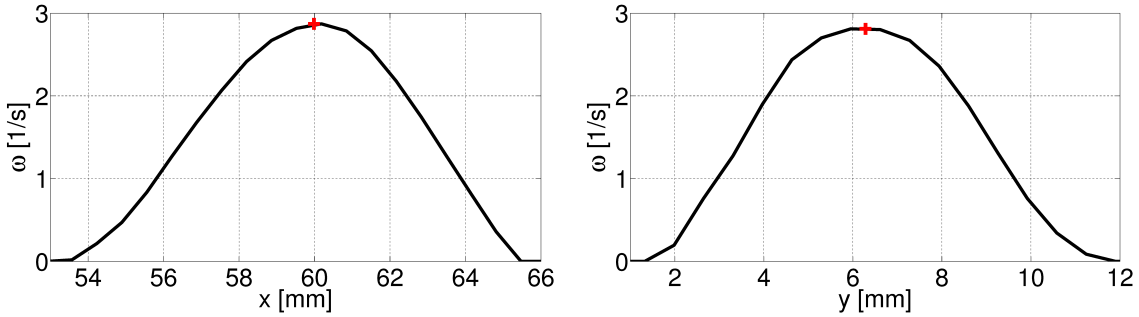

(a) Horizontel ω distribution (b) Vertical ω distribution

Figure 4.8: Vorticity distribution around the center (red cross) of a nearly circular shaped vortex

between the radii is handled using the ellipse formula shown in Equation 4.14.

$$\left(\frac{x - x_m}{r_v}\right)^2 + \left(\frac{y - y_m}{r_h}\right)^2 = 1 \tag{4.14}$$

However, most cases of vortex expansion are covered validly (see Figure 4.9). Another challenge is that vortices mostly appear in pairs, or in the case of vortex interaction at least two vortices are close together. Therefore, the vorticity distribution is not becoming or crossing zero at the edges. Moreover it is not always clear which vorticity belongs to which vortex, especially in the case of co-rotating vortex pairs. Therefore starting from the center in each direction only points higher than the standard deviation are taken into account. This means that the real vortex edge is not found, but the detected radii correspond to $66\,\%$ of the vortex, referred to as the core radius of a vortex. This is shown in both illustrations of Figure 4.9, where the vorticity distribution expands beyond the detected edges. Furthermore, the maximum of the vorticity distribution has often a small offset related to the center. Since the offset is small, the lower distance is taken in order to not overestimate the edges. This is shown for the horizontal line in illustration (b) of Figure 4.9. Taking the larger distance could cause an overlap in cases of nearby vortices. Since the vortex interaction is evaluated, this would lead to false results, because two nearby vortices would have the same bigger size, even if they are not merged. Having found the core radius the points within can be extracted and analyzed with regard to the vortex strength and flow behavior.

The evaluation of vortex interaction is based on the behavior of the vortices in respect to the time. Therefore the vortex must be tracked. Furthermore, all vortices of the flow field time series must be determined and followed. This is done by computing the propagation velocity of the core center once a vortex is detected. By means of the propagation velocity a search radius, in which the core center in the next time step has to be found, is computed. A safety factor of 1.5 is added to the computed search radius because of the influence of the flow field on the real vortex propagation. Since the propagation velocity can not be computed from the first flow field an initial search radius has to be given. If a vortex core center is found within the search radius in the next time step, the rotation of the vorticity is checked. If they match, it is very likely that the vortex is the same as detected in the previous time step. To be sure, the vortex center of the further time step should be near

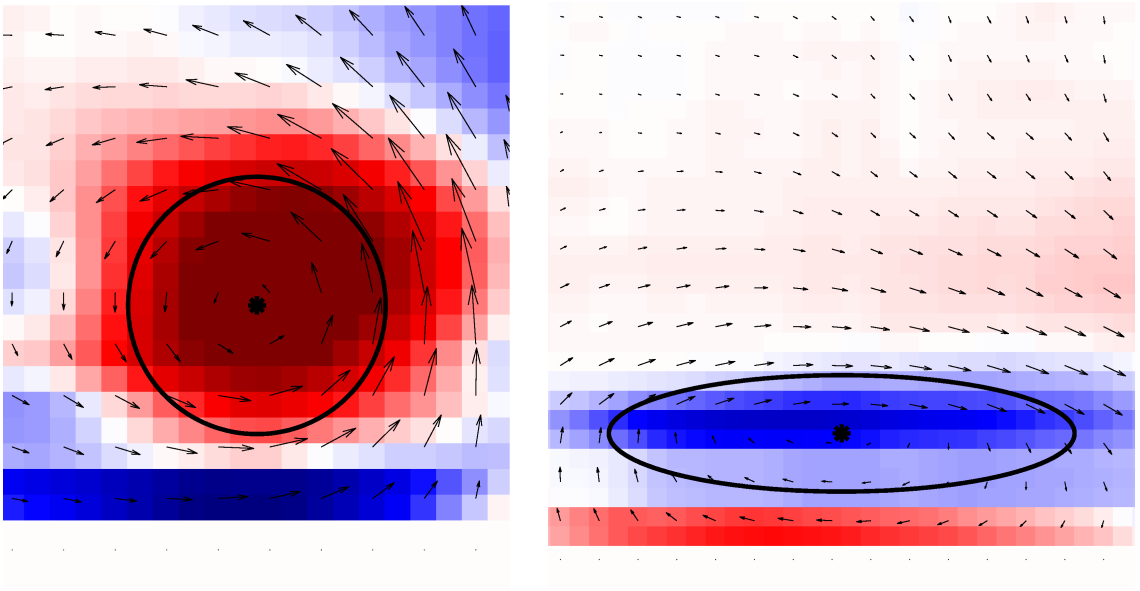

(a) Vorticity and flow field with core radius edges of a nearly circular shaped vortex

(b) Vorticity and flow field with core radius edges of a elliptic shaped vortex

Figure 4.9: Edge detection for differently shaped vortices

the estimated place. To estimate the new position of the vortex center the strength and direction of the propagation velocity is used (see Equation 4.15).

$$\begin{pmatrix} x \\ y \end{pmatrix}_{est} = \left(\begin{pmatrix} u \\ v \end{pmatrix}_{conv} \cdot \Delta t \right) + \begin{pmatrix} x \\ y \end{pmatrix}_{old} \tag{4.15}$$

In Figure 4.10 (a) a vortex with the search radius is shown woffering an estimation where the vortex in the next time step should be. In Figure 4.10 (b) the next time frame is shown with the vortex center found. The estimation is only slightly higher than the actual core center. The accuracy of the estimation is increasing with decreasing Δt for two reasons. First, the propagation velocity is more precisely, on the other hand, the influence of the flow field on the vortex is decreasing.
The overall result of the detection and tracking algorithms is shown in Figure 4.10 (c). There the vortex with the core radius and tracked positions is shown. The vortex properties, obtained within the core radius, are stored and composed for each tracked vortex. On the basis of this data the strength, behavior and changes during the existence of every vortex are analyzed. Moreover the changes during the interaction of all vortices can be monitored over time.

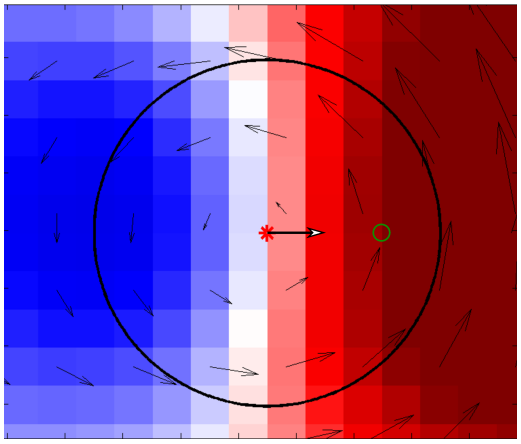

(a) Vortex with search radius and estimated position of vortex in the next time frame (circle)

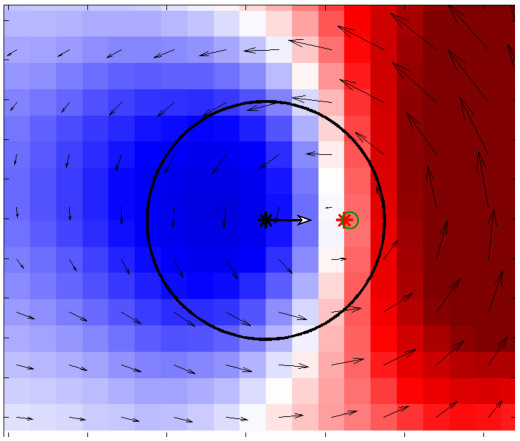

(b) Same vortex in the next time frame (red star). The search radius and estimated position form the prior time frame is also shown as working principle of the tracking algorithm

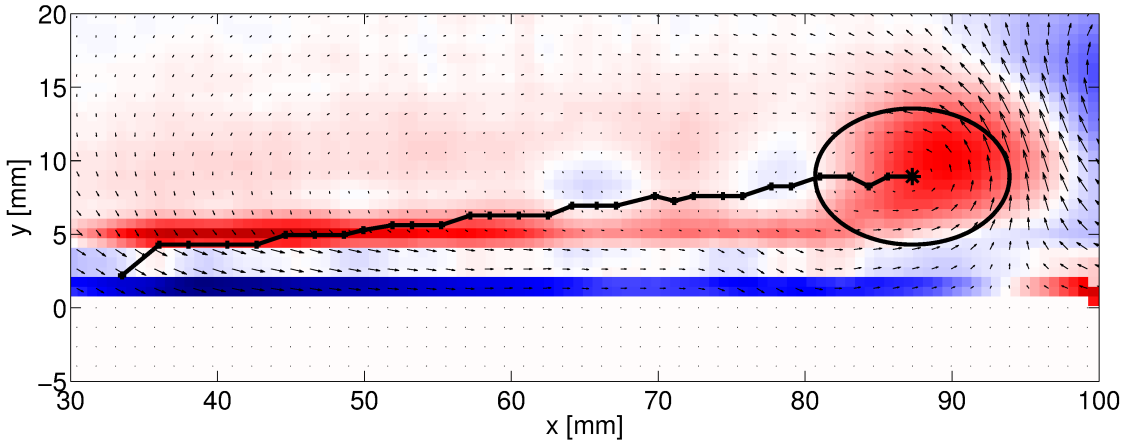

(c) Tracked vortex with core radius after several time frames

Figure 4.10: Working principle (a,b) of tracking algorithm and overall result of detection and tracking

5 Investigations of Vortex Interaction

This sections presents the evaluation of the investigation of merging vortices without pressure gradient. At first a single vortex is investigated with regard to the behavior and propagation velocity. Then the interaction of several vortices induced at different time steps are presented.
Afterwards, the results of the half diffuser measurements are provided. In the beginning the parameters and the base flow of the diffuser are shown. Next the influence of a single actuator row is presented. Then the effect of a pressure gradient on the merging of vortices induced from three actuator rows at different phase shifts is stated. At last a comparison of single, distributed and cooperative actuation is done.

5.1 Vortex interaction without pressure gradient

5.1.1 Single vortex propagation

The main idea is to amplify the reattachment process of pulsed blowing by inducing a second vortex interacting with the arriving vortex. Knowing the propagation velocity of the vortices induced by the pulsed blowing is important to estimate the required time delay for constructive interaction. Therefore, a single actuator was switched on at the flat plate of the LWK-2 and measured with 22 uncalibrated hot film sensors simultaneously to obtain several velocity ratios at different Reynolds numbers.
In Figure 5.1 (a) the original data is plotted over time for all active hot film sensors. The jet velocity is $v_{jet} = 30\,\frac{\mathrm{m}}{\mathrm{s}}$ at an incident velocity of $v_\infty = 20\,\frac{\mathrm{m}}{\mathrm{s}}$, which leads to a velocity ratio of $VR = 1.5$ and a momentum coefficient of $c_\mu = 0.12\,\%$. The dimensionless frequency is $F^+ = 1.5$. The propagation of the vortices is shown for three periods. Since the hot film sensors are uncalibrated the amplitude does not say anything about the strength of the vortex. Also two different types of hot film sensors are used. The more sensitive ones are attached between the actuator rows, whilst the less sensitive are installed behind the last actuator. To overcome the intensity problem each signal is normed with its maximum and only the fluctuation part is taken. Nevertheless the cross correlation (Equation 4.8) has been applied. Knowing the distance of the sensors and the time delay, the cross correlation can be computed and in Figure 5.1 (b) an example of the propagation velocity is shown. The parameters for the actuation are the same as on the left illustration. The red circles indicate the analyzed velocity and the dashed line is an exponential fit of the second order. The propagation velocity is considered valid if the normed correlation coefficient is at least 0.5. The propagation velocity drops strongly to the velocity of the incident flow within

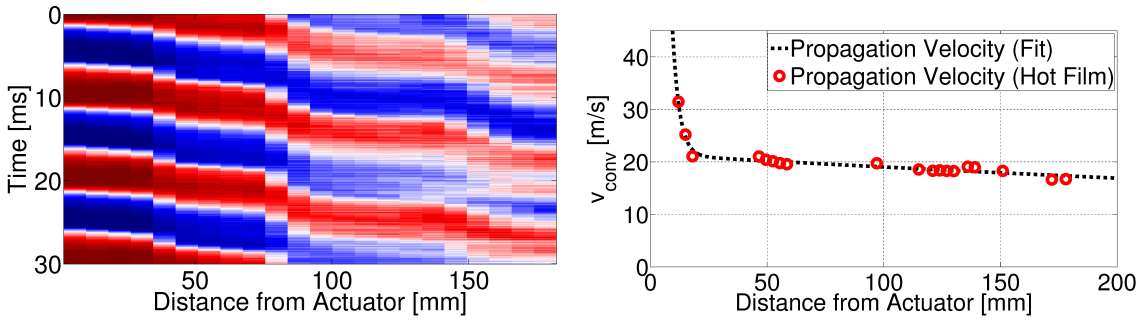

(a) Time depending hot film signal at different locations

(b) Computed propagation velocity and exponential fit

Figure 5.1: Original hot film data and propagation velocity of a Vortex at a velocity ratio $VR = 1.5$ and Reynoldsnumber $Re = 6.87e^5$

the first $x = 16\,\mathrm{mm}$. Then the propagation velocity of the vortex decreases slightly over the measured distance. It seems that the propagation velocity is linked to the incident flow. Therefore, several measurements have been taken to investigate the relation of jet velocity and incident flow on the propagation velocity. These measurements are shown in Figure 5.2. The illustration on the left hand side shows the relation of the jet velocity, decreasing from $VR = 2.3$ to $VR = 1.0$ at a constant Reynoldsnumber of $Re = 6.87e^5$. Velocity ratios below 1 do not correlate sufficiently to give a clear statement about the vortex behavior. The higher the jet velocity, the higher the propagation velocity, but the increase is small compared to the increase of the jet velocity. Nevertheless it has to be mentioned that in this case, where the distance of the actuators is $d_{act} = 40\,\mathrm{mm}$, the gap between the propagation velocities has to be considered.
The Reynoldsnumber has a bigger influence on the propagation velocity as shown in Figure 5.2(b). In the presented case, the jet velocity is held constant at $v_{jet} = 40\,\frac{\mathrm{m}}{\mathrm{s}}$. This means not only a wider gap between the propagation velocities, but also a change in the gradient for the different Reynoldsnumbers. This leads to the assumption that the Reynoldnumber has the largest influence on the vortex propagation, but the velocity ratio also has a stronger influence than Figure 5.2 (a) would presume. To combine these two dependencies, the propagation velocity at a distance of $d_{40} = 40\,\mathrm{mm}$ was computed and put into relation with the incident velocity.
The propagation ratio $PR = \frac{v_{conv,40}}{u_\infty}$ is shown in Figure 5.3 (a) over the velocity ratio. Since the actuators have a $40\,\mathrm{mm}$ distance, the influence of the jet velocity must be considered, but the main driving parameter is the Reynoldsnumber. The influence of the jet velocity increases linearly with the increase of the velocity ratio. This means that a relationship can be established to predict the propagation velocity at the point of the second actuator. This formula is given by Equation 5.1. To expand the prediction to other actuator distances a factor $k_{40} = \frac{1-2\cdot d_{act}}{1-2\cdot d_{40}}$ is established. Since the jet influence is decreasing with increasing distance, the gradient of the slope in Figure 5.3 is decreasing slightly. The factor therefore decreases the influence of the jet velocity as well as the slope. This assumption is valid for distances up to $d_{act} = 100\,\mathrm{mm}$.

$$v_{conv,act} \approx k_{40} \cdot \left(\frac{1}{6} \cdot v_{jet} + \frac{3}{4} \cdot v_\infty \right) \tag{5.1}$$

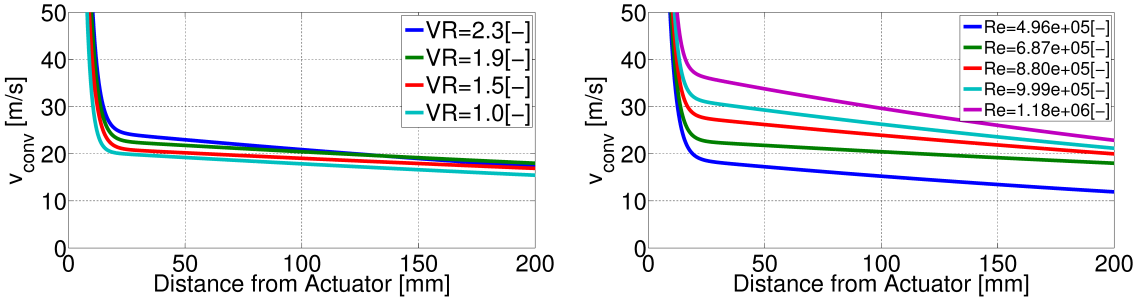

(a) Dependency of the propagation velocity on the velocity ratio

(b) Dependency of the propagation velocity on the Reynoldsnumber

Figure 5.2: Dependencies of vortex propagation velocity v_{conv}

The hot film sensors are unable to resolve the single vortex, but show an increase in amplitude over the hole blowing phase. To analyze the vortex independently, time depending PIV measurements are taken with a velocity ratio of $VR = 2.4$, a momentum coefficient of $c_\mu = 0.3\,\%$ with a sampling frequency of $F_s = 6\,\mathrm{kHz}$. In Figure 5.4 (a) the first appearance of a full vortex is shown with core center and core radius. The vorticity of the vortex of the flow field is also shown, where red marks counter-clockwise and blue clockwise rotating vortices. In Figure 5.4 (b) the same vortex is shown, when reaching the second actuator after an elapsed time of $\Delta t = 1.7\,\mathrm{ms}$. The tracked positions are also shown in this illustration.
It shows that the vortex is not only propagating in streamwise direction, but also departs from the surface during its propagation. At this point a counter rotating vortex starts to build up, which is indicated by the clockwise rotating vorticity in front of the tracked vortex. Another point is that the vorticity and size of the vortex are decreasing with distance and time, due to its dissipative behavior.
The tracking algorithm not only computes the core center and radius, but also determines the propagation velocity of the vortex core. During the measurements ten vortices are recorded and the propagation velocity is analyzed. The median velocity of the ten vortices

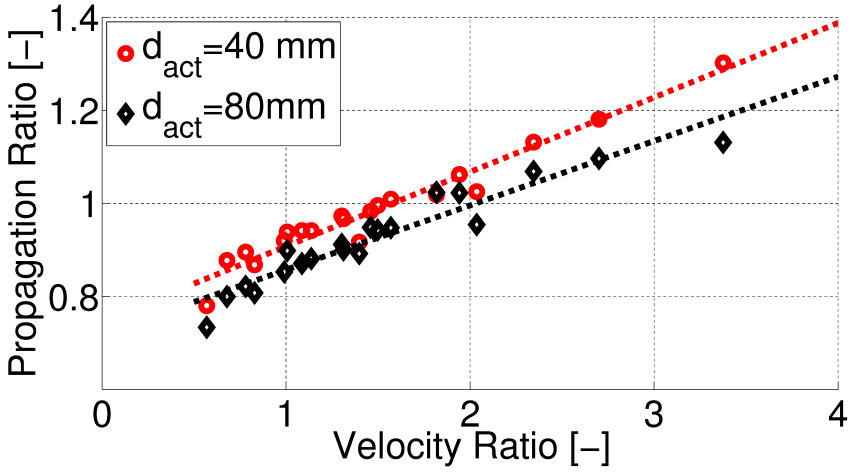

Figure 5.3: Propagation ratio over velocity ratio

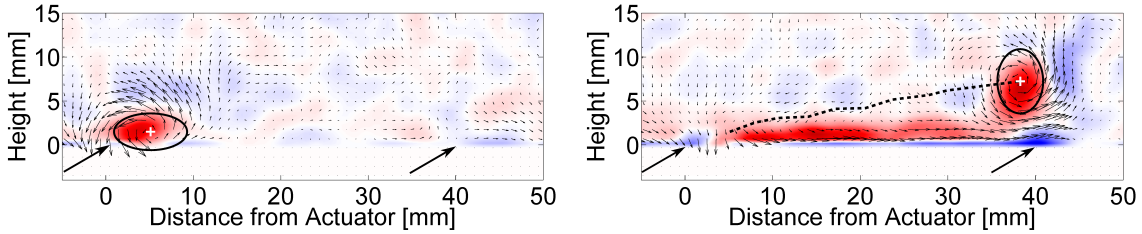

(a) Vortex with core radius and center after emergence

(b) Same vortex of illustration (a) after a certain time with tracked positions

Figure 5.4: Time resolved PIV visualizations of single actuation on a flat plate

are taken and compared to the result of the hot film measurements, acquired under the same conditions. Since these ten vortices are not tracked at the same position and are varying in occurrence length, the velocities within a five millimeter range are taken to build the median. This is shown in Figure 5.5. The propagation velocity of the vortex corresponds well with the velocity computed from the hot film sensors and the computed exponential fit. The velocity predicted on the basis of Equation 5.1 would be under the given conditions $v_{conv,40} \approx 23\,\frac{\mathrm{m}}{\mathrm{s}}$. The velocity from the PIV measurements is at that point $v_{conv,PIV} = 20.5\,\frac{\mathrm{m}}{\mathrm{s}}$. Although the prediction is overestimating the velocity slightly, it can be used as a first hint. Knowing the propagation velocity, now the phase shift between to actuators is computed with Equation 2.10. In this case the phase shift is around $\Theta \approx 84\,°$, taking into account that the vortex is fully built up ten millimeter behind the slot.

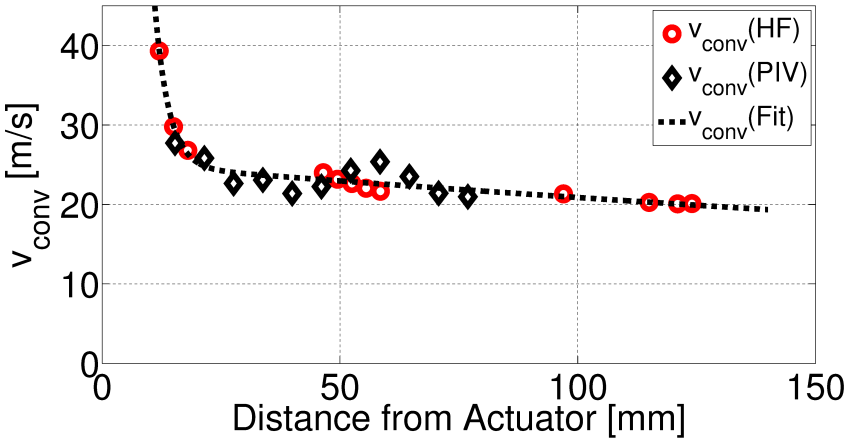

Figure 5.5: Comparison of computed vortex propagation velocity from hot film and PIV data for $v_\infty = 20\,\frac{\mathrm{m}}{\mathrm{s}}$ and a velocity ratio of $VR = 2.5$

5.1.2 Vortex interaction

Understanding the interactions of two co-rotating vortices induced at different times is a prerequisite to achieve the main task of reattaching the flow more efficiently. Therefore the interaction of two vortices is investigated at the LWK-2 for different phase shifts Θ by means of PIV measurements. This was done at a velocity ratio of $VR = 2.3$, a momentum coefficient of $c_\mu = 0.3\,\%$ and Strouhalnumbers of $F_1^+ = 1.5$ and $F_2^+ = 1.3$.
Using the correlated phase shift, computed on the basis of Equation 2.10, it turned out that the vortices are not merging sufficiently. This is shown in Figure 5.6 (a-d). The first vortex induced from the first actuator reaches the second slot at $d_{act,2} = 40\,\mathrm{mm}$ in illustration (a). This is considered as $t = 0\,\mathrm{ms}$ of the interaction process. In illustration (b) the second actuator starts to induce a vortex at $t = 0.34\,\mathrm{ms}$. In this state the first vortex is already interfering with the new one. Furthermore the emergence of the new vortex is affected. In the next steps the new vortex fully builds up and is pushing the first one away. This process withdraws energy and therefore vorticity of both vortices. This is shown in illustration (c) at a time step of $t = 0.68\,\mathrm{ms}$ after the interaction process starts. This results in a co-rotating vortex pair interfering with each other, where only one vortex with low vorticity remains (d) at the end.
This destructive behavior continues if the second vortex is induced too late, as shown in Figure 5.7 (a-d). In this case the phase shift is set to $\Theta = 92\,°$. Again, the appearance of the first vortex marks the beginning of the interaction process with $t = 0\,\mathrm{ms}$. In illustration (b) at the beginning of the second actuator blowing, the first vortex is at the point, where the second vortex is building up. After $t = 0.51\,\mathrm{ms}$ the uprising velocity of vortex two

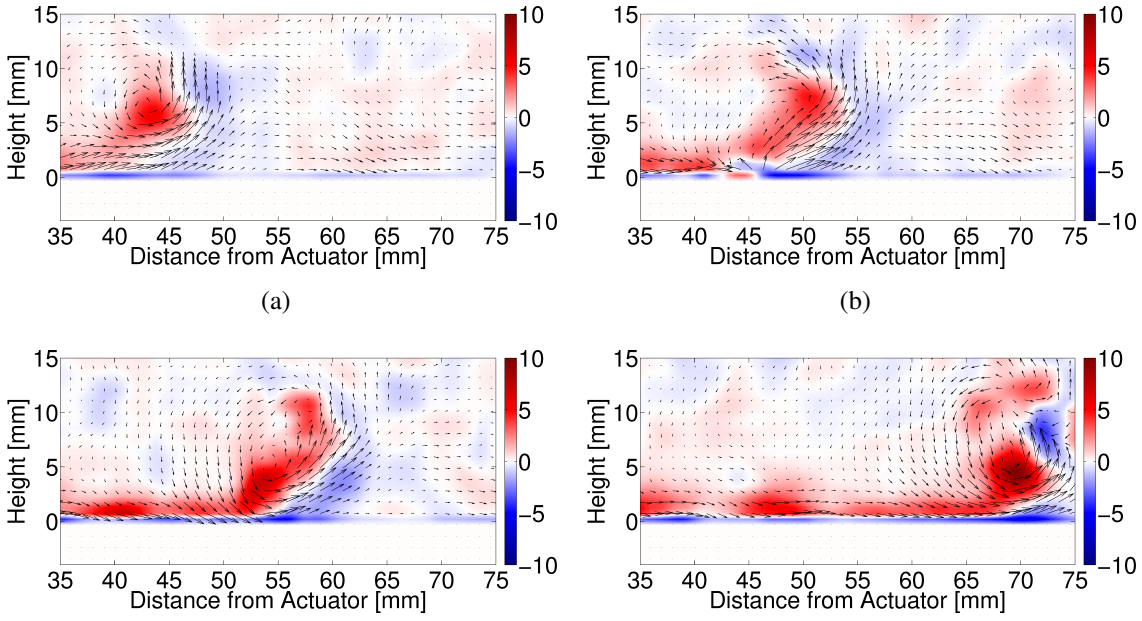

Figure 5.6: Interaction of two co-rotating vortices $\Theta = 84\,°$. (a) Appearance of first vortex $t = 0\,\mathrm{ms}$ (b) Inducing second vortex $t = 0.34\,\mathrm{ms}$ (c) First vortex is pushed upwards $t = 0.68\,\mathrm{ms}$ (d) Both vortices interfering with each other $t = 1.36\,\mathrm{ms}$

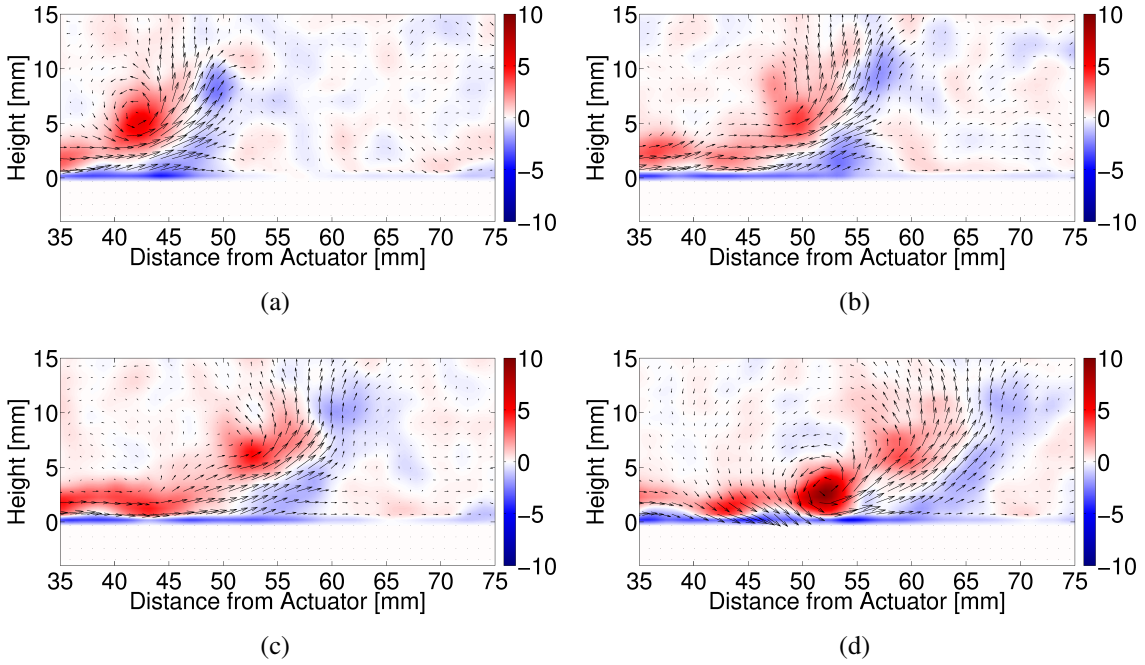

Figure 5.7: Destructive interaction of two co-rotating vortices $\Theta = 92\,°$. (a) Appearance of first vortex $t = 0\,\mathrm{ms}$ (b) Second actuator starts blowing $t = 0.34\,\mathrm{ms}$ (c) First vortex resolves $t = 0.51\,\mathrm{ms}$ (d) Second vortex with less vorticity $t = 0.85\,\mathrm{ms}$

is dissolving the first one completely (illustration c) and for a short time span no vortex is present at all. In the last illustration (d) the ongoing blowing of the second actuator is inducing a new, but significantly weaker vortex.
Therefore the phase shift was lowered so that the second actuator induces a vortex before the vortex of the first actuator arrives (see Figure 5.8 (a-d)). The optimal phase shift to merge these two vortices is found to be $\Theta = 72\,°$, which is $\Delta t = 0.4\,\mathrm{ms}$ earlier than expected. After the first vortex appeared at $t = 0\,\mathrm{ms}$ in illustration (a) the second vortex starts to build up in front of this one. Illustration (b) shows, that the second vortex uses the vorticity of the first one to build up a bigger vortex. After $t = 0.51\,\mathrm{ms}$ this process is still ongoing, even enhancing the vorticity further (c). In the last illustration (d) a bigger and stronger vortex emerges from this interaction process. Not only the vortex is amplified, the interaction time is also reduced, having a less disturbing effect on the flow.
The special case of simultaneous blowing results in two vortices propagating downstream hardly influencing each other. Nevertheless, due to the turbulence of the previous vortex the subsequent vortex is losing strength more rapidly and disappearing earlier.
To amplify the vorticity and duration of a vortex, and thus the mechanism of reattachment, it is necessary to induce the second vortex before the first one appears. The merging process is characterized by the newly created vortex receiving the vorticity of the incoming vortex. Using a constructive phase shift the duration of the merging is fast, with minimal turbulence involved. The emergence of the second directly underneath the vortex to merge with, repels the first one resulting in two turbulent co-rotating vortices with weaker vorticity. To decompose the first one the second actuator must induce a vortex shortly after the first vortex has passed the point of vortex origin. In this case the direction of the normal

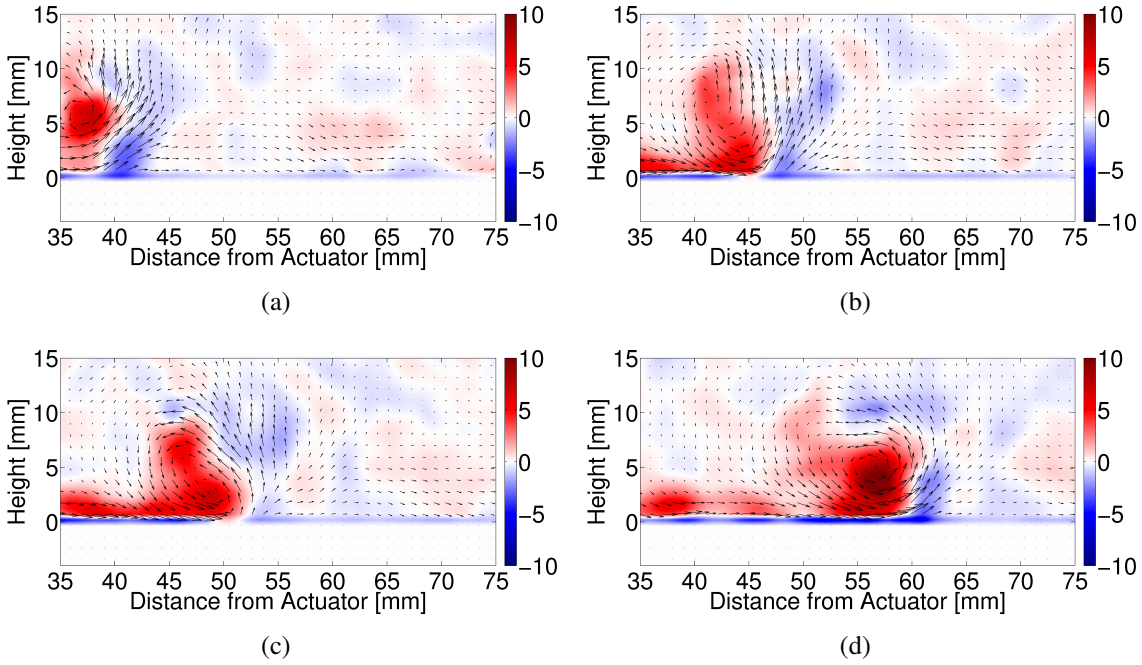

Figure 5.8: Cooperative interaction of two co-rotating vortices $\Theta = 72\,°$. (a) Appearance of first vortex $t = 0\,\mathrm{ms}$ (b) First step of vortex merging $t = 0.34\,\mathrm{ms}$ (c) Bigger vortex builds up $t = 0.51\,\mathrm{ms}$ (d) Stronger vortex propagates downstream $t = 0.85\,\mathrm{ms}$

velocities are opposed to each other. Nevertheless the ongoing blowing of the actuator results in a newly generated vortex.
To confirm the previous results under the conditions and the adaptions necessary for the measurements carried out at the GSW, 2D hot wire measurements are done. A relevant section of the middle plane was measured with an exponential grid for better resolution of the boundary layer. The 1342 single measurement points are phase averaged with Equation 4.6 to visualize the coherent structures of the flow field. To correspond with the characteristic length of the setup, the dimensionless frequency of the first actuator row is set to a subharmonic of $F^+ = 1$. This rsults in a Strouhalnumber of $F_1^+ = 2$ and therefore for the second actuator row $F_2^+ = 1.7$. The velocity ratio was set to $VR = 2$.
In Figure 5.9 (a) simultaneous blowing is shown. There, two vortices are propagating simultaneous downstream until dissolving after $t = 0.32\,\mathrm{ms}$. Applying the Equations 2.10 and 5.1 the phase shift would be $\Theta \approx 100\,°$. This is shown in Figure 5.9 (b). The path of the first vortex is interrupted before the vorticity of the second vortex starts. It can be seen that at period step $\Phi = 175\,°$ two isosurfaces are on top of each other until the upper dissolves a few steps later. This is in accordance with the measurement presented in Figure 5.6 (d) where the previous vortex is pushed upwards. If a vortex emerges, from the second actuator row before the first generated vortex arrives, the two vortices are matching harmoniously propagating the entire measured length (see Figure 5.9 (c)). At last a deconstructive phase shift, similar to the measurements at the LWK-2 is shown in illustration (d). In this case, the phase shift is set to $\Theta = 150\,°$. The first vortex is terminated by the emergence of the second vortex, and as a consequent the second vortex only lasts a short time before

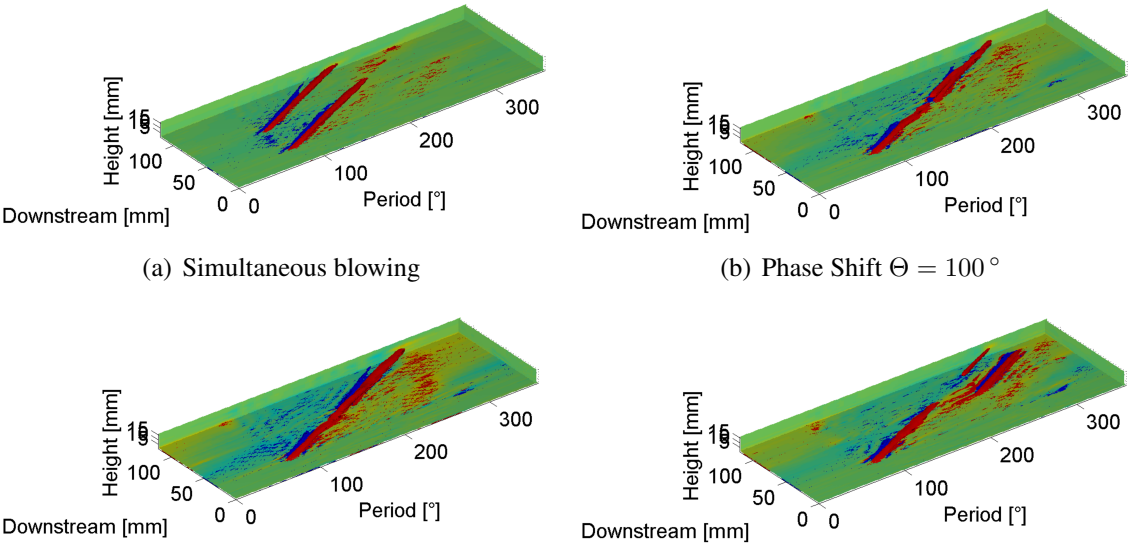

(a) Simultaneous blowing

(b) Phase Shift $\Theta = 100\,^\circ$

(c) Phase Shift $\Theta = 89\,^\circ$

(d) Phase Shift $\Theta = 150\,^\circ$

Figure 5.9: Comparison of the vorticity for different phase shifts. Counter-clockwise rotating (red) and Clockwise rotating (blue) (a) Simultaneous blowing of two rows (b) Computed phase shift $\Theta = 100\,^\circ$ (c) Constructive interaction for phase shift $\Theta = 89\,^\circ$ (c) Destructive interaction at phase shift $\Theta = 150\,^\circ$

disappearing. Similar two the previous destructive case the ongoing blowing generates a new vortex.
Interpreting these results to amplify or stabilize the reattachment process it is necessary to merge the generated vortices cleverly. The merging process is designated combining the vorticity of the vortices. This can be done by inducing the second vortex before the previously induced vortex arrives in the appearance area of the new vortex. If the second vortex is generated too early both vortices are propagating downstream, hardly affecting each other. Likewise, inducing a vortex too late also generates two downstream propagating vortices. Nevertheless these two vortices are not as strong as a vortex produced by a single actuator. Two considered cases show insufficient results. First, inducing the second vortex exactly under the propagating vortex. This leads to an repellent reaction of the vortices, withdrawing energy from both. The second even more destructive case is generating a new vortex right behind the propagating one. This can cause an annihilation of both vortices.

5.2 Vortex interaction in half diffuser

5.2.1 Basic flow of half diffuser

The measurements regarding the reattachment of a pressured induced separation were carried out in a half diffuser with an adjustable step angle. To analyze and evaluate the results of these measurements knowing the basic flow parameters is important. Several parameters are important when dealing with flow separation at an inclined step. There is the step Reynoldsnumber Re_H, which uses the step height H as characteristic length. This Reynoldsnumber is therefore a function of the step angle α_{step}. The flow velocity was set to $v_\infty = 20\,\frac{\mathrm{m}}{\mathrm{s}}$. With these values the step Reynoldnumber is between $1.59e^5 \leq RE_H \leq 1.74e^5$ for the used step angles $21\,^\circ \leq \alpha_{step} \leq 23\,^\circ$. This Reynoldnumbers are influencing the shear layer of the separated flow. In these cases the shear layer is dominated by the turbulent share, since the step Reynoldsnumber is above $Re_H < 10^4$ [43].
Another parameter is the condition of the boundary layer, which should be turbulent upstream of the step. In order to ensure that for all flow conditions, the transition of the boundary layer is forced with a carborundum at the beginning of the wind tunnel inlet. Following *Schlichting und Gersten* [66], the form factor for a turbulent boundary layer is between $1.3 < H_{12} < 1.4$. The form factor can be computed with the displacement height δ_1 and the momentum thickness δ_2.

$$H_{12} = \frac{\delta_1}{\delta_2} \tag{5.2}$$

At a step Reynoldnumber of $Re_H = 174000$ corresponding to a step angle $\alpha = 23\,^\circ$, the displacement height is $\delta_1 = 1.35\,\mathrm{mm}$ and the momentum thickness is $\delta_2 = 1.007\,\mathrm{mm}$. The boundary layer thickness in front of the step is $\delta_{99} = 9.46\,\mathrm{mm}$. The form factor of $H_{12} = 1.35$ proves therefore the fully turbulent boundary layer.
In a half diffuser the cross section is extended by the inclined step, whereby the static pressure increases by converting kinetic energy into pressure energy. The increase in pressure is therefore a function of the expansion ratio ER of the half diffuser and is stated as pressure recovery Δc_p. The pressure recovery is measured by means of two wall mounted pressure sensors, one before the step with a distance $x/L = -0.6$ and the second right after the step with a spacing of $x/L = 1.5$. The positions are shown in Figure 5.10 (a) in addition to the occurring flow states for different step angles α_{step}. In Figure 5.10 (b) the pressure recovery is plotted against the step angle. The pressure recovery increases linearly until a step angle of $\alpha_{step} = 20\,^\circ$. The local separation bubble as shown in illustration (a) arises at an angle of $\alpha_{step} = 17\,^\circ$, but is not measured by the pressure transducer, which is still outside of the separation [32]. At $\alpha_{step} = 20\,^\circ$ the pressure induced separation arises and is increasing with an increasing step angle. This happens, when the pressure recovery Δc_p drops in illustration (b). The downstream pressure transducer is now located within the area of recirculation. In this state, the pressure recovery takes place over the free evolving extension of the separated flow field. The separation position is thereby moving upstream until it geometrically separates at the leading edge of the step at $\alpha_{step} = 24\,^\circ$. The bigger the separation gets, the more the pressure recovery Δc_p decreases.
Active flow control is supposed to reattach the flow for these step angles of pressure induced separation ($20\,^\circ \leq \alpha_{step} \leq 23\,^\circ$). Effective reattachment of the flow to the surface

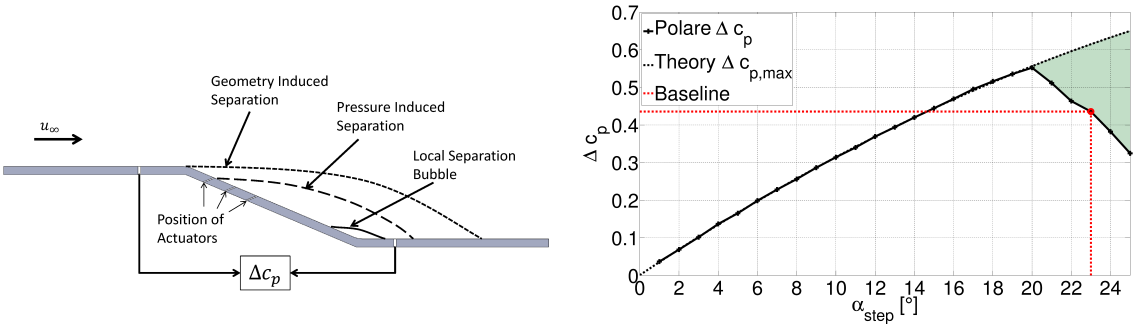

(a) Schematic visualization of separation states and positions of the pressure transducer (after [32])

(b) Δc_p vs α_{step} of the half diffuser

Figure 5.10: (a) Schematic separation conditions and positions of the pressure transducers. (b) Pressure recovery over the step angles for the half diffuser

leads to a pressure recovery of $\Delta c_{p,max}$ as shown by the dotted line in illustration (b) on the right. Therefore the value of Δc_p is a measure of the effectiveness of the actuation for the half diffuser configuration.
Since most investigations took place at a step angle of $\alpha_{step} = 23\,^\circ$, this position as well as the corresponding pressure recovery ($\Delta c_p = 0.43$) is marked in Figure 5.10 (b) by the dashed lines. The marked area is the theoretical gain active flow control can achieve. The averaged velocity field with pressure induced separation is shown in Figure 5.11 including the actuator insert with the position of the three actuators downstream. The scaling of the abscissa is zero at the beginning of the insert, which do not mark the beginning of the step, due to the round edge of the half diffuser. The distance between the actuators is $d_{act} = 40\,\mathrm{mm}$. For the step angle of $\alpha_{step} = 23\,^\circ$ the averaged separation point lies above the first actuator slot. The redirection of the flow is reduced and a recirculation area is formed, whereby the pressure recovery is decreasing. This flow condition, with the separation position upstream of the actuator, is a challenging configuration for the actuation concept, but with certain parameters it is possible to reattach the flow.

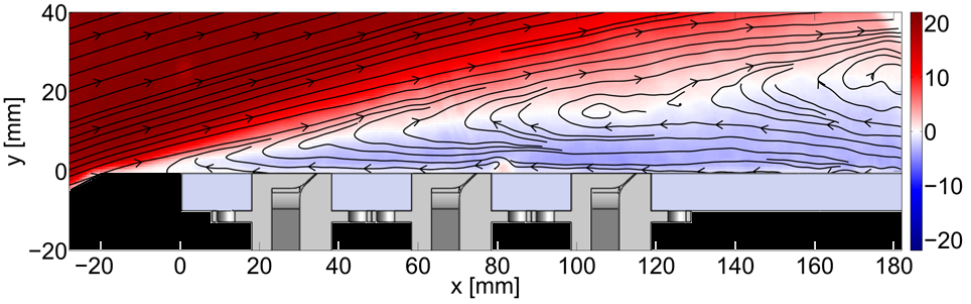

Figure 5.11: Flow visualization of the half diffuser at a step angle $\alpha_{step} = 23\,^\circ$ and $v_\infty = 20\,\frac{\mathrm{m}}{\mathrm{s}}$. The positions of the inactive actuators ($v_{jet} = 0\,\frac{\mathrm{m}}{\mathrm{s}}$) are shown relatively to the separation.

Since reasonably developed vortices are essential for this investigation, and to use the full capabilities of the PIV system, the total momentum coefficient was set to $c_{\mu,3} \approx 1\,\%$. The results of the cooperative actuation are compared to the simultaneous blowing. This is done to show the benefit, which can be achieved by a slight increase of the system effort compared to the distributed actuation.

5.2.2 Single vortex influence

Active flow control by means of pulsed blowing generates coherent structures resulting in a dynamic exchange and a transfer of fluid vertical to the surface. Therefore not only the increase in momentum in the recirculation area, but also the dynamic effects are used to reattach the flow. This increases the performance of the active flow control system. In Figure 5.12 (a), the dominating vortex structure is shown for the phase angle of $\Phi = 100\,°$. The temporal distance between the rising edge of the trigger signal and the appearance of the vortex is $\Phi = 85\,°$. The vortex is fully developed after $\Delta t = 0.33\,\mathrm{ms}$. The phase averaging, introduced in Equation 4.6, filters the phase independent and small scale structures.
With the beginning of the blowing phase, a vortex is induced at the actuator slot, the vorticity and strength of which depends on the jet angle [32]. In this case a jet angle of $\alpha_{jet} = 45\,°$ is chosen, resulting in a positive rotating vortex above the jet. The jet is redirected to the surface by another induced vortex, directly supplying high energy fluid to the recirculation area. Furthermore the vortex structure is responsible for a fluid transfer transversely to the main flow.
In the illustration on the ride hand side of Figure 5.12 the counter rotating vortex is shown. This happens at a phase shift of $\Phi = 190\,°$. These two vortices are building a vortex pair, transporting low energy fluid away from the recirculation area. Meanwhile the velocity component towards the surface and the jet are transporting high energy fluid to the surface. The vorticity of the vortex pair over the propagating distance is shown in Figure 5.13 (a). After the development of the vortex the vorticity increases within the next three phase

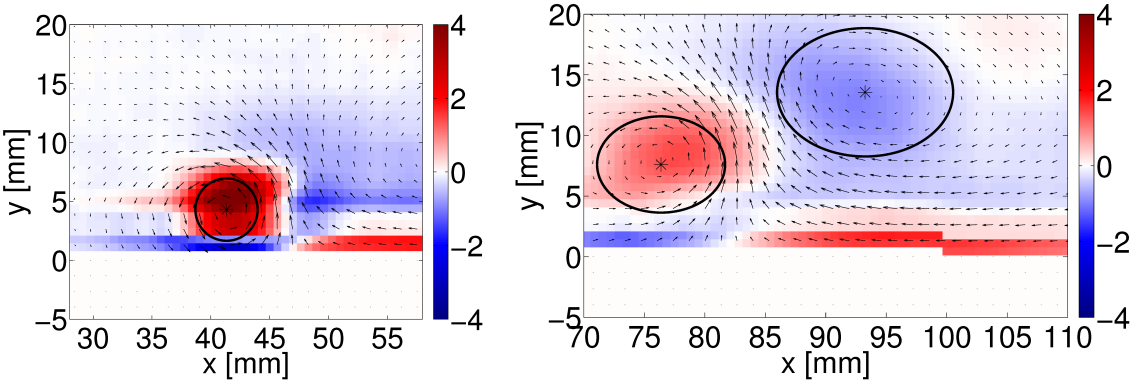

(a) Counter-clockwise rotation vortex shortly after the emergence

(b) Emergence of a related clockwise rotating vortex

Figure 5.12: Single vortex after $t = 0.34\,\mathrm{ms}$ and related vortex pair after $t = 4.2\,\mathrm{ms}$

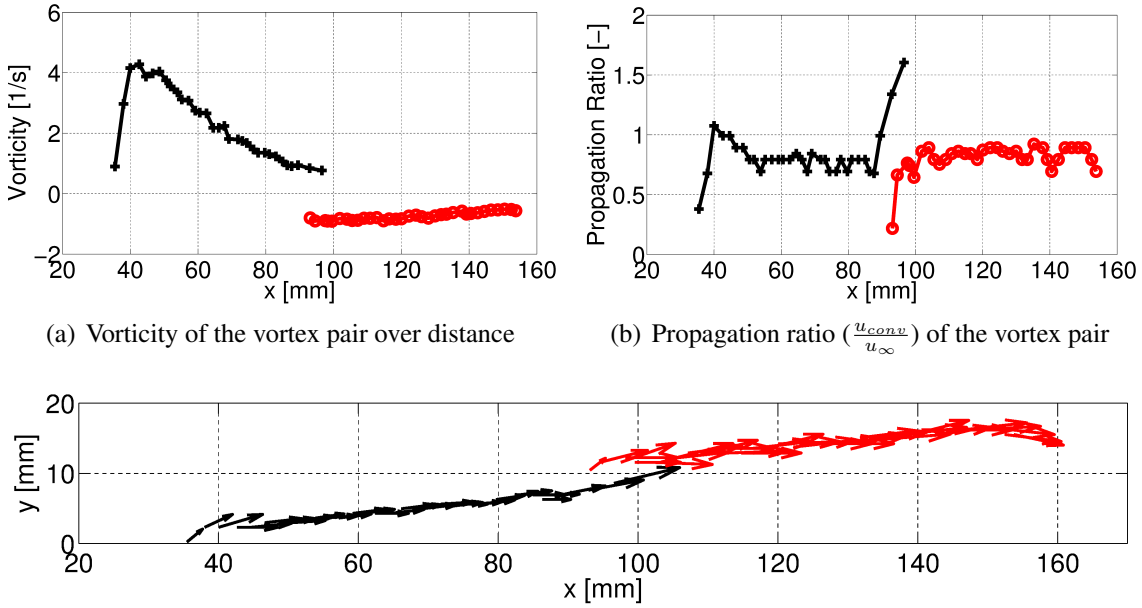

(a) Vorticity of the vortex pair over distance

(b) Propagation ratio ($\frac{u_{conv}}{u_\infty}$) of the vortex pair

(c) Velocity and direction of the vortices over distance

Figure 5.13: Vorticity, propagation ratio and direction of the vortices propagation, which emergence for single actuation

steps to its maximum. With further propagating the vortex is loosing strength, until it disappears after $\Delta\Phi = 175\,°$. The counter rotating vortex appears late at a phase angle of $\Phi = 190\,°$ with less vorticity. The vorticity then only decreases a little during the propagation downstream until it disappears after $\Delta\Phi = 165\,°$. The propagation ratio $PR = \frac{\vec{v}_{conv}}{u_\infty}$ over distance is shown in illustration (b) of Figure 5.13. With the appearance of the vortex the propagation velocity increases up to $\vec{v}_{conv} = 1.2 \cdot u_\infty$ and then decreases to a velocity around $\vec{v}_{conv} = 0.8 \cdot u_\infty$, which complies with the median propagation velocity of this vortex. At the time the counter rotating vortex is detected the vortex propagation accelerates up to $\vec{v}_{conv} = 1.65 \cdot u_\infty$ until it disappears. Nevertheless the counter rotating vortex propagation velocity increases to the median velocity, propagating with it until it disappears.
To understand the acceleration of the counter clockwise rotating vortex Figure 5.13 (c) is shown. There the position in the flow field as well as the velocity is presented. The jet angle $\alpha_{jet} = 45\,°$ at the beginning of the vortex propagation is visible. The vortex is then steadily cast away from the surface. The acceleration begins, when the vortex is reaching the end of the boundary layer, which is about $\delta_{99} \approx 9\,\mathrm{mm}$. Furthermore, the appearance of the clockwise rotating vortex seems to enhance the propagation velocity as well.

5.2.3 Effect of pressure gradient on vortex interaction

The vortex interaction with zero pressure gradient is presented in section 5.1.2. In this section the vortex interaction is investigated with the present of an adverse pressure gradient, obtained at the half diffuser with an step angle of $\alpha_{step} = 23\,^{\circ}$. To analyze the effect of the phase shift, three representative actuation cases are considered.
The simultaneous blowing is shown in Figure 5.14 (a), depicting three vortices with core radii and tracked positions. The vortices are induced at the same time but are located at different positions downstream. The core radii are increasing with the location of the actuators downstream, but the vorticity, on the other hand, is decreasing. The vortices are dissipating energy and thereby growing bigger in size. Apparently a vortex is impeded if another vortex is following and this effect is increasing with the number of vortices. The reason for that, stems from the mechanism of reattaching the flow by fluid entrainment through the shear layer. Through interaction of the vortices with the separated shear layer a momentum transfer vertical to the incident flow is generated. This momentum transfer ensures an exchange of fluid through the shear layer. Furthermore, the jet of the actuator attaches to the surface directly increasing the momentum of the separated area. Having several vortices following each other, the sequencing vortex transports the dispensed fluid of the jet located downstream away from the surface. Moreover, the fluid which is transported into the recirculation behind a vortex, is contrary to the entrainment of the following one.
The vorticity of the core radius is obtained for every single time step and shown in Figure 5.14 (b) over the distance x. The vortices are numbered from the first time they are detected. The average appearance distance of the single vortex is about $90\,\mathrm{mm}$ until it disappears.

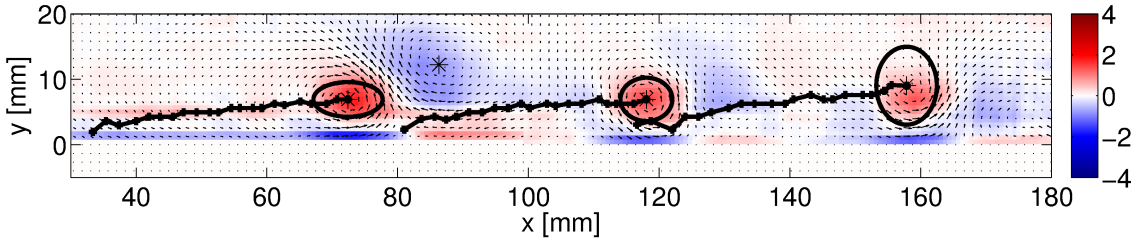

(a) Tracked positions with core radius for simultaneous blowing

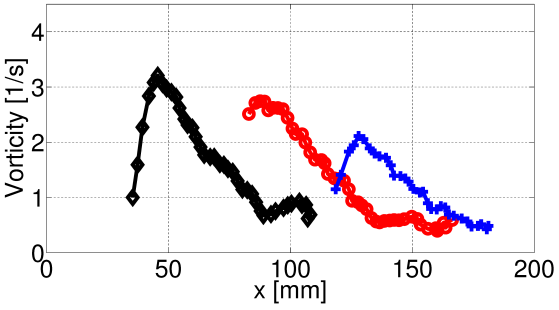

(b) Vorticity over tracked location

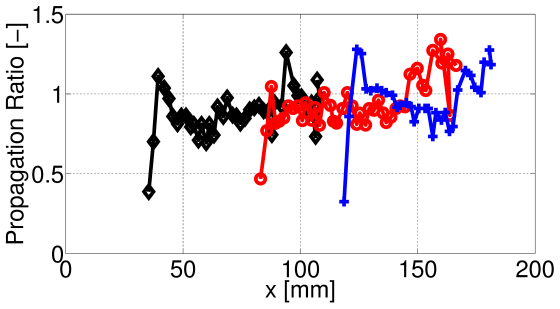

(c) Propagation Ratio vs. vortex location

Figure 5.14: Flow field, vorticity and propagation ratio for simultaneous blowing. Phase shift $\Theta = 0\,^{\circ}$, Velocity Ratio $VR = 2.4$, Step Reynoldsnumber $Re_H = 174000$

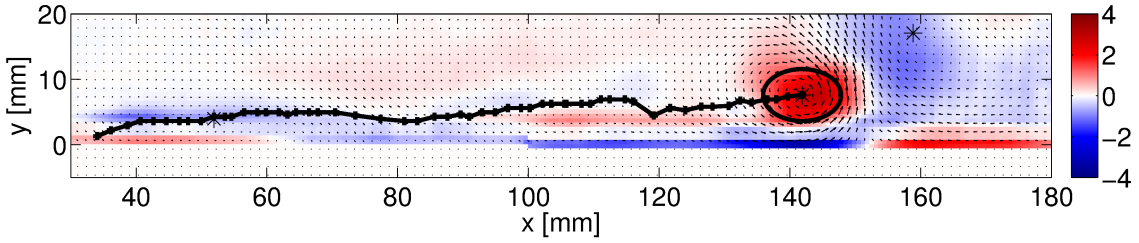

(a) Tracked position and core radius for cooperative actuation

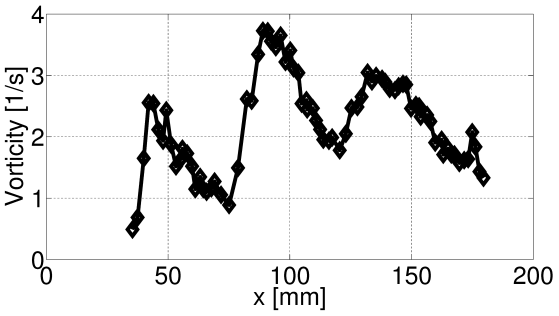

(b) Vorticity vs tracked location

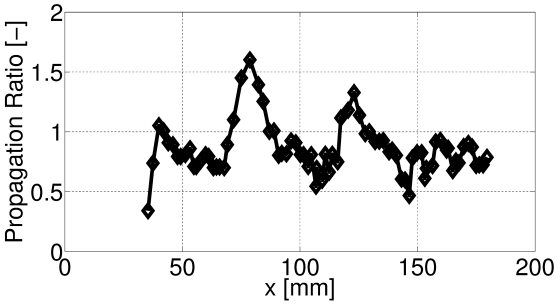

(c) Propagation Ratio over tracked position

Figure 5.15: Flow field and vorticity for constructive interaction. Phase shift $\Theta = 105\,°$, Velocity Ratio $VR = 2.4$, Step Reynoldsnumber $Re_H = 174000$

The vorticity is thereby decreasing rapidly within the first $60\,\mathrm{mm}$. The dissipative effect of the vortex influence on each other starts with the development of the vortices. While the first one has the highest vorticity, it is decreasing with every next vortex. However the gradient of the vorticity loss is not changing due to this interaction. The propagation ratio is similar to the single actuator row active and shown in Figure 5.14 (c). The propagation ratios increase up to $PR \approx 1.2$ and then decrease to the median ratio of $PR = 0.8$. All the vortices start to increase the propagation velocity when leaving the boundary layer. Although the velocity ratio is smaller, the vortices are propagating further downstream compared to the single actuation.
The cooperative interaction, as shown in Figure 5.15 (a), is, however, more constructive. The core radius as well as the vorticity are amplified by the merging process of the vortices. The tracked position suggests that the interaction between the arriving vortex and the induced vortex from the third actuator row is not merging perfectly ($x \approx 120\,\mathrm{mm}$). The transition at $70\,\mathrm{mm} \leq x \leq 90\,\mathrm{mm}$ is smoother than at the location of the third actuator row between $110\,\mathrm{mm} \leq x \leq 130\,\mathrm{mm}$. This is eventually proven by the vorticity shown in Figure 5.15 (b). Whereas the first merging process resulted in an amplification of the vorticity ($x \approx 74\,\mathrm{mm}$), the second interaction ($x \approx 120\,\mathrm{mm}$) do not gain a higher vorticity. At least the vorticity is higher than for a single one and is still stabilizing the vortex.
Nevertheless, to understand the loss of vorticity, the merging process must be considered more closely. Therefore a time series of the first vortex interaction is shown in Figure 5.16 (a-f). In the illustration on the left, the vortex arrives after $\Delta t = 0.42\,\mathrm{ms}$ of its first appearance. In illustration (b) the second actuator starts the blowing phase after a phase shift of $\Theta = 105\,°$. Since the jet is oriented $\alpha_{jet} = 45\,°$, the vortex arises about $5\,\mathrm{mm}$ behind the slot location. The jet velocity is redirected towards the preceding vortex and

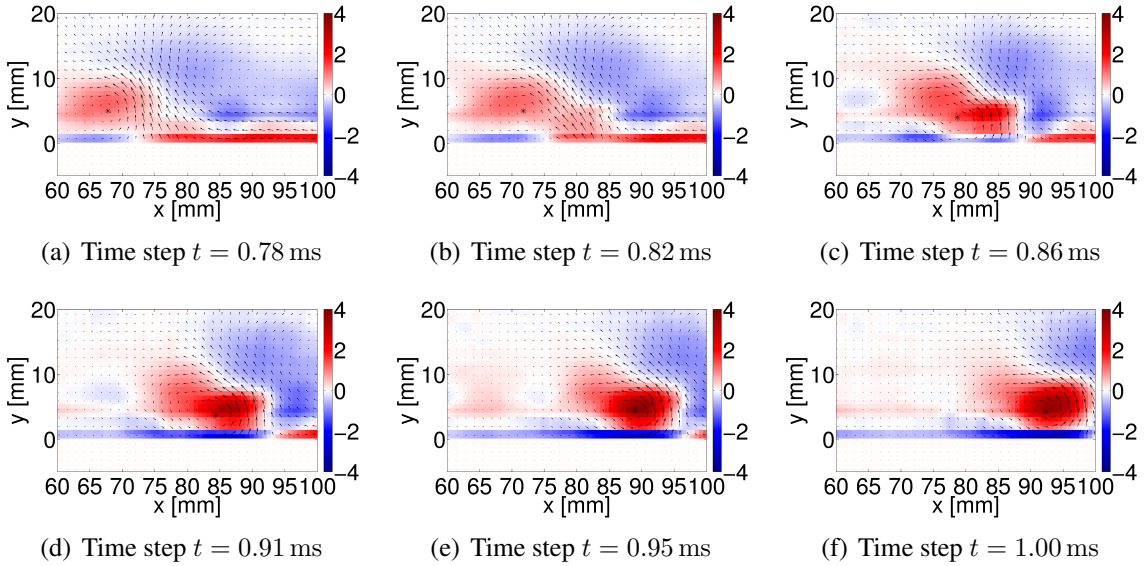

(a) Time step $t = 0.78\,\mathrm{ms}$ (b) Time step $t = 0.82\,\mathrm{ms}$ (c) Time step $t = 0.86\,\mathrm{ms}$

(d) Time step $t = 0.91\,\mathrm{ms}$ (e) Time step $t = 0.95\,\mathrm{ms}$ (f) Time step $t = 1.00\,\mathrm{ms}$

Figure 5.16: Sequence of vortex merging process for $\Theta = 105\,^\circ$ at a step Reynoldsnumber of $Re_H = 174000$

simultaneously this vortex is descending towards the surface (see Figure 5.16 (c-d)). The rotating velocity is extended over the arriving vortex, forming one big stretched vortex. In the illustrations (e -f) a stronger circular shaped vortex is propagating further downstream. The merging process happens within a time span of $\Delta t \approx 0.2\,\mathrm{ms}$. The necessity of inducing a vortex at the right time is important and depends on the propagation velocity of the vortex. The merging process is influencing not only the vorticity and core radius, but also the propagation velocity as shown in Figure 5.16 (c). Here the propagation ratio of the vortex PR is plotted over the vortex location x. The initial propagation velocity of the merged vortices is increased by $50\,\%$, compared to the initial propagation velocity of the first vortex. As a result, the third actuator induces the vortex a little to late and therefore the merging process is impeded and less vorticity evolves. At least the interaction is still there, amplifying and stabilizing the vortex. Nevertheless the second merging process can be optimized and obtains an even higher impact on the separation, by adjusting the phase shift Θ between the second and the third actuator row.
A constructive vortex interaction takes place over certain phase shifts Θ, but inducing

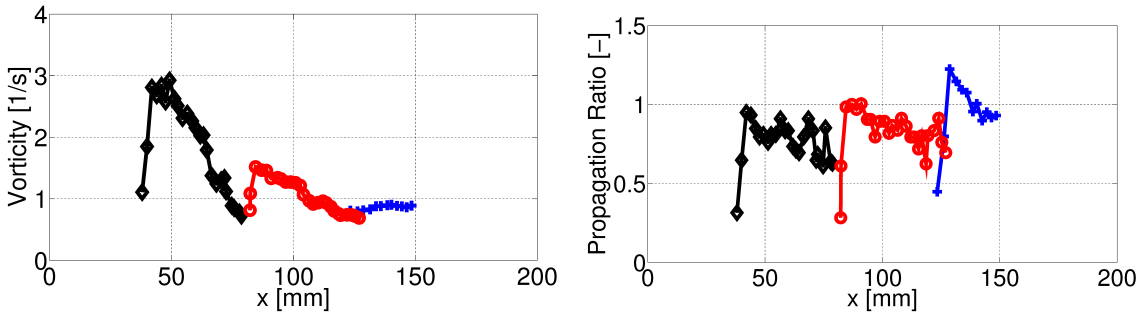

(a) Vorticity of a destructive phase shift over distance (b) Propagation ratio for the destructive case in (a)

Figure 5.17: Vorticity and propagation ratio for a phase shift of $\Theta = 150\,^\circ$

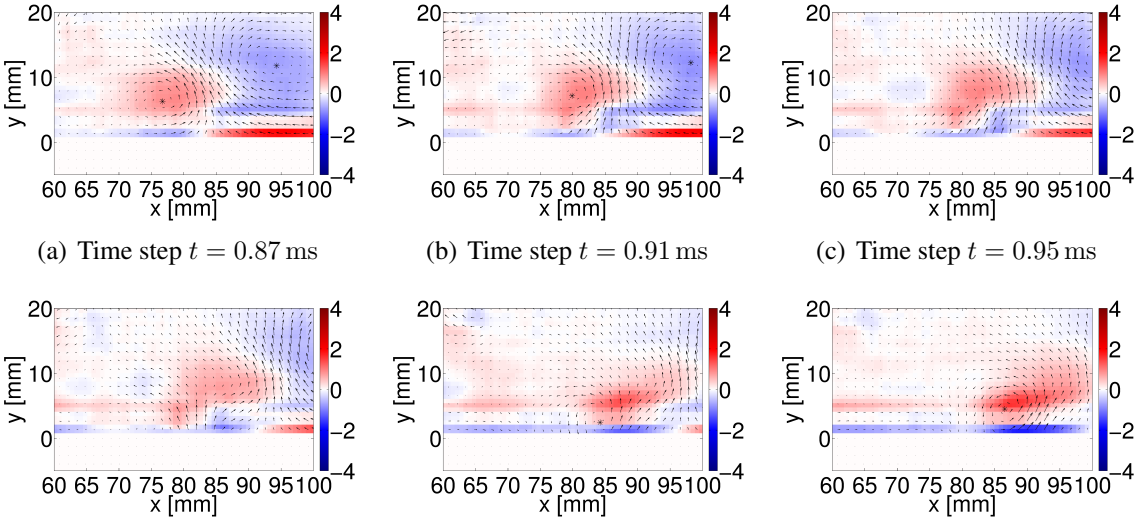

(a) Time step $t = 0.87\,\mathrm{ms}$ (b) Time step $t = 0.91\,\mathrm{ms}$ (c) Time step $t = 0.95\,\mathrm{ms}$

(d) Time step $t = 1.00\,\mathrm{ms}$ (e) Time step $t = 1.04\,\mathrm{ms}$ (f) Time step $t = 1.09\,\mathrm{ms}$

Figure 5.18: Sequence of a destructive vortex interaction for $\Theta = 150\,^\circ$ at a step Reynoldsnumber of $Re_H = 174000$

a subsequent vortex too late is dissolving the preceding vortex. The vorticity of such a destructive case is shown in Figure 5.17 (a). The first vortex develops normally until the emergence of the next vortex, where the preceding one dissolves. The newly generated vortex has $50\,\%$ less vorticity than the first one. When the third vortex is induced, a small overlap occurs, but the vorticity is again reduced about $50\,\%$. However, the propagation ratio, shown in illustration (b) of Figure 5.17, is hardly affected by the destruction of the vortex.

A sequence of this progress is shown in Figure 5.18 (a-f). In illustrations (a-b),the vortex is propagating over the emerging area of the second vortex. At the beginning of the blowing phase of the second actuator, the first vortex is located right in front of that slot. Therefore, the descending velocity of the first vortex is opposed to the ascending velocity of the jet, resulting in a complete destruction of this particular vortex (Figure 5.18 (c-d)). Moreover, the newly induced vortex is impeded in its development, resulting in a weaker vortex with less vorticity. Although a small part of the preceded vorticity seems to be included in the new one (illustration (e)), the vorticity is small compared to even the simultaneous blowing. Since the propagation velocity is hardly changing during this interaction, the procedure is repeated at the next slot.

5.2.4 Comparison of single and cooperative actuation

When reattaching a separated flow by pulsed blowing, it is important to increase the flow momentum in the separated area and refill it with high energy fluid. To increase the wall near momentum an entrainment through the shear layer has to take place in addition to the direct input of the jet. This fluid transfer triggered by the coherent structures is visualized by means of the velocity perpendicular to the surface.
To extract the normal velocities, lines perpendicular to the surface of the flow field behind every actuator ($d_n = 6\,\mathrm{mm}$) are taken and analyzed for every measured phase angle. In figure 5.19 these lines are shown in respect to the velocity magnitude of the pressure induced separated flow. The shear layer at the lines have a height of $(y/H)_1 \approx 0.05$ for the first line, $(y/H)_2 \approx 0.95$ for the second and $(y/H)_3 \approx 0.12$ for the last. To guarantee the fluid transfer through the shear layer, the normal velocity must be above these values. The fluid transfer for different cases are shown in Figure 5.20 (a - i) in respect to one actuation period. Each column illustrates the corresponding line in Figure 5.19. The first case (Figure 5.20 (a-c)) is the single actuator row active with a velocity ratio $VR_2.9$. The vortex is induced at a phase angle of $\Phi = 85\,^\circ$. The vortex induces an upward velocity around the positive velocity component of the vortex responsible for the removal of the low energy fluid. The extension of this fluid transfer extends clearly above the shear layer. Meanwhile the descending velocity is present over nearly the whole actuation period, transferring high energy fluid into the separation area. For the second location at $x = 80\,\mathrm{mm}$ the vortex has extended, still transporting fluid through the shear layer. However, a region with no normal velocities can be seen around the upward direction of the velocity. This region extends as shown in Figure 5.20 (c) at a location of (x = 120 mm). Since a velocity ratio of $VR = 2.9$ is sufficient to reattach flow by itself, the entrainment is still there, but decreasing with the location downstream.
In Figure 5.20 (d-f) simultaneous blowing for the three lines is illustrated. Here the velocity

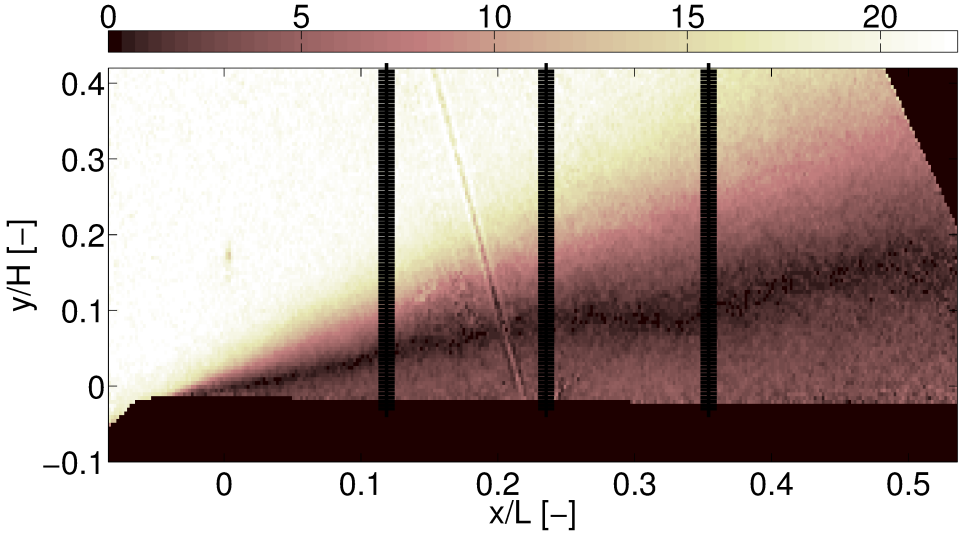

Figure 5.19: Half diffuser flow for an unactuated case at $v_\infty = 20\,\frac{\mathrm{m}}{\mathrm{s}}$ with the marked lines where the normal velocities are analyzed. The position are related to the actuator slot positions

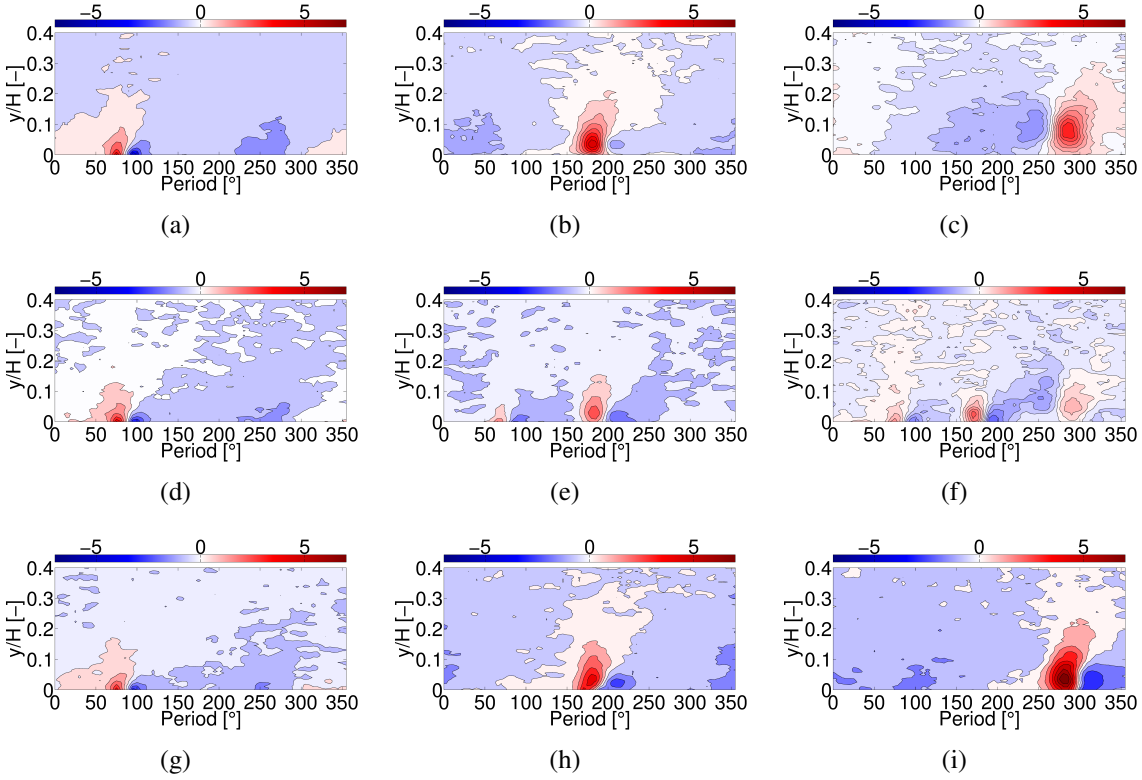

Figure 5.20: Normal velocities for different actuation cases over period. (a-c) Single actuation. (d-f) Simultaneous blowing ($\Theta = 0\,°$). (g-i) Constructive phase shift ($\Theta = 105\,°$)

ratio is $VR = 2.4$ and therefore $21\,\%$ less than for the single actuation. At the beginning of the step in Figure 5.20 (a) the entrainment through shear layer is shown. The descending velocity of the vortex is inducing a transfer of fluid towards the surface, while the upward direction is casting fluid away. In the next illustration (e) the impeded transfer is depicted. The first vortex is weakened and the transfer is damped. The second vortex is smaller than the upstream one, hardly interacting with the shear layer at a height of $(y/H)_2 \approx 0.9$. The transfer of fluid is getting worse with the location downstream (Figure 5.20(f)). The third vortex is even smaller, not triggering a fluid transfer through the shear layer. The whole transfer is scattered, damping the entrainment process over the period.
The cooperative actuation for a phase shift of $\Theta = 105\,°$ and a velocity ratio $VR = 2.4$ is shown in the illustration (g - i). Again at the first position the vortex triggers an entrainment, lasting nearly the whole period. The second location, as illustrated in (h), shows the enhancing mechanism of cooperative interaction. The vortex has merged and strengthened inducing a higher transfer through the shear layer throughout he entire period. This effect is even greater for the location further downstream (Figure 5.20 (i)). Both directions of the normel velocities of the vortex are growing bigger ensuring an optimal transfer all along the increasing shear layer height.
Due to the different velocity ratios between the single actuator row and the cases of cooperative blowing, a quantitative comparison is impossible. Nevertheless, the qualitative comparison shows that a constructive interaction is suitable to stabilize the entrainment through shear layer, at least over the measured flow field. Moreover the fluid transfer is

even stronger with less jet velocity when the vortices merge than for single blowing. On the other hand, it is shown that simultaneous blowing impedes the entrainment by evading the fluid transfer through the simultaneous propagating vortices. Furthermore, not only the entrainment process is impeded, but also the formation of the vortices itself.

6 Evaluation of Cooperative Actuation

In this section the evaluation and improvement of the cooperative actuation are presented. In the first part the results of the PIV measurements are shown. Since reasonably developed vortices are essential for this investigation, and to use the full capabilities of the PIV system, the total momentum coefficient was set to $c_{\mu,3} \approx 1\,\%$. The results of the cooperative actuation are compared to the simultaneous blowing. This is done to show the benefit, which is attainable by only a small increase of the system effort compared to the distributed actuation.
The second part describes the improvement with regard to the required momentum coefficient to reattach the flow. The savings for the single actuator as well as for the cooperative actuation system are presented.
Then the potential saving of mass flow is illustrated followed by a short discussion, an outlook and an overview of recommended future work.

6.1 Benefits of vortex interaction

6.1.1 Effect of vortex interaction on flow properties

The phase shift Θ was varied during the PIV measurement on the inclined step at the half diffuser to understand the behavior of the cooperative actuation. Moreover, to gain knowledge about the robustness, a sufficient segment of phase shifts was measured. The aim was to find the limits of constructive interaction. Therefore, the phase shift was varied in $\Delta\Theta = 5\,^\circ$. With the results of the flat plate experiment and Equations 2.10 and 5.1 the phase shift was computed to be $\Theta = 99\,^\circ$. Nevertheless the right assumption was that the adverse pressure gradient slows down the propagation velocity. Confirmed by the first results obtained during the measurement, the optimum phase shift was estimated to be around $\Theta = 120\,^\circ$. Therefore the phase shift was varied around this value in one-degree steps. For the PIV measurements, the simultaneous blowing is taken as reference to illustrate the performance increase compared to the easiest setup.
The various cases of the PIV measurements at the half diffuser have been analyzed by means of the RANSAC algorithm as presented in section 4.2. The vortex structures are considered as aligned if the deviation function of the algorithm is minimal. From the PIV flow field ten slices in height, throughout the normal velocities of the vortex, are taken into account to validate the result. Five of the ten slices are shown in Figure 6.1 (a).
The illustration on the right of Figure 6.1 shows the result of the alignment of vortices

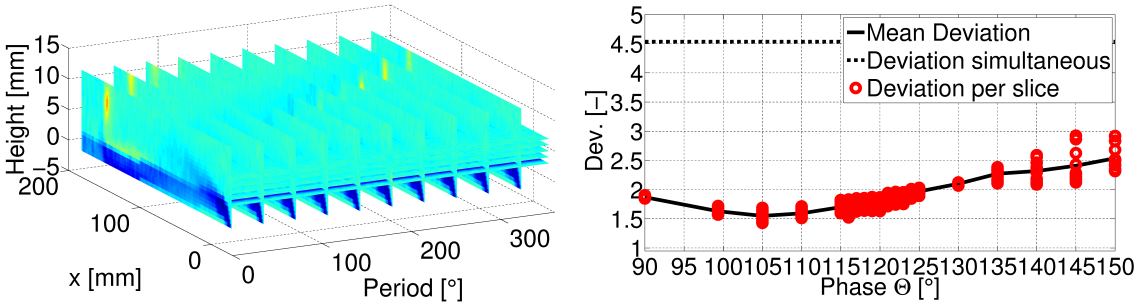

(a) Description of the single slices used for the RANSAC algorithm

(b) Deviation of single layers and its mean value resulting from RANSAC algorithm analysis versus phase shift Θ

Figure 6.1: Description and main findings of the RANSAC algorithm

obtained with the RANSAC algorithm. The development of the deviations shows a minimum at a phase shift of $\Theta = 105\,°$. The dependence on Θ is confirmed in every single slice and has a minimum at the same phase shift. This result confirms the assumption that the adverse pressure gradient slows down the propagation velocity of the vortex, but the reduction is smaller than expected. Nevertheless the region from $90\,° \leq \Theta \leq 130\,°$ shows a reasonable alignment of the vortices without too much deviation between the single slices. Increasing the phase shift further, the alignment as well as the single deviation between the slices are also increasing. This means that the outer vortex region somehow aligns, but the vortex core is drifting further apart. The strong deviation with simultaneous blowing ($\Theta = 0$) is not surprising due to the fact that the vortices are formed at the same time and therefore the footprints can not be aligned.
The behavior of the vortex is analyzed using the detected and tracked core radius of all investigated configurations. Mainly the vorticity as a measure of the rotation is evaluated. The outcome of the vortex tracking is shown in Figure 6.2. The results are normalized to the highest vorticity (eddy viscosity) calculated. Again, the best performance is at phase shift $\Theta = 105\,°$ with a gain of $\Delta\omega = 51\,\%$ ($\Delta\mu_\tau = 57\,\%$). This is due to the constructive merging process of the vortices presented in Figure 5.16. The vorticity (eddy viscosity) is enhanced by the fusion of two vortices, which results in a higher vorticity and, due to the the higher fluctuation, an enhancement of the eddy viscosity. Nevertheless the gain could be increased taking the modified propagation velocity after the interaction process into account. A constructive interaction can be considered for phase shifts between $95\,° \leq \Theta \leq 115\,°$.
A further increase of the phase shift results in an increase of the vorticity followed by a sudden drop of vorticity or eddy viscosity respectively. After a short recovery of vorticity (eddy viscosity) it drops back to a low value. These phases, between $115\,° \leq \Theta \leq 125\,°$, will be referred to as the transition of vortex merging. There, the location of the preceding vortex is above the point where the new vortex is induced. Since the data is phase averaged, no clear statement about the interaction can be made. However, on the flat plate (Section 5.1.2) the corresponding phase shift to this state is $\Theta = 84\,°$. It has been observed that from ten periods, at least two periods show some merging behavior. This leads to the assumption that the vortices sometimes merge and sometimes annihilate each other, depending on the surrounding flow state. According to which state happens more often, the phase averaged

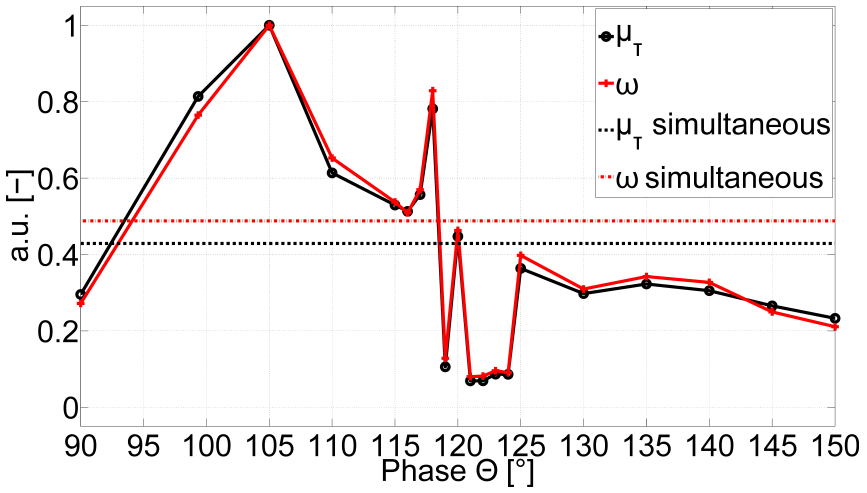

Figure 6.2: Comparison of vorticity (eddy viscosity) between cooperative actuation and simultaneous blowing

data show a merging or a destructive behavior. Originating from Figure 6.2, it is plausible that the interaction at $\Theta = 118\,^\circ$ occurs when the first vortex is located right in the $45\,^\circ$ jet stream. Later the destructive part seems to outweigh the interaction process.
As shown in Figure 5.18, increasing the phase shift leads to an annihilation of one vortex and an impeded development of the newly generated one. A further increase in phase shifts would lead to the same or damped effect as stated for simultaneous blowing, where the vortices are withdrawing energy of each other (see Figure 5.14(b)). The effect increases the closer the vortices are.

6.1.2 Momentum coefficient reduction

Since the aim is to reduce the needed momentum to reattach flow, the velocity ratio VR and therefore the momentum coefficient $c_{\mu,n}$, was lowered. As demonstrated on the flat plate in section 5.1.2, the propagation velocity depends on the incident flow velocity as well as on the jet velocity of the actuation. As shown in section 5.2.3 the pressure gradient has an influence on the propagation velocities of the vortices. Therefore, the pressure recovery Δc_p was measured for different phase shifts Θ and velocity ratios VR. The phase shift was varied in two-degree steps and the velocity ratio was changed by adjusting the mass flow. The dotted line in the following Figures shows the pressure recovery necessary to reattach the flow of the separated half diffuser. The step angle is $\alpha_{step} = 23\,^\circ$ at a step Reynoldsnumber of $Re_H = 174000$ for the shown cases. All cooperative measurements are compared to a single actuator row active, capable to reattach the flow. The velocity ratio for the conventional concept is $VR = 1.94$ and the associated momentum coefficient is measured with $c_\mu = 0.226\,\%$.
In Figure 6.3 (a) the pressure recovery distribution for total $c_{\mu,3} = 0.042\,\%$ is shown. The black line is a fit to the measured data points to illustrate the behavior in respect to the phase shift. The effect on the separation is small, since the separated flow has a pressure recovery of $\Delta c_p = 0.43$. Furthermore no dependence on the phase shift is visible. The

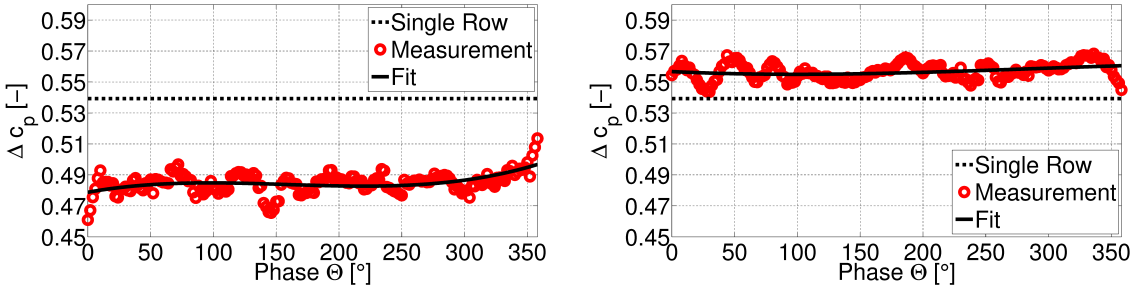

(a) Cooperative actuation with overall mass flow of $\dot{m}_3 = 0.0018\,\frac{\mathrm{kg}}{\mathrm{s}}$

(b) Cooperative actuation with overall mass flow of $\dot{m}_3 = 0.003\,\frac{\mathrm{kg}}{\mathrm{s}}$

Figure 6.3: Pressure recovery Δc_p over different phase shifts Θ compared to single actuation with $\dot{m}_1 = 0.0028\,\frac{\mathrm{kg}}{\mathrm{s}}$

velocity ratio of a single actuator is measured with $VR = 0.47$ meaning that not only the generated vortex is dissipating rapidly, but also the induced momentum is limited. Since there is no effect on the phase shift it is doubtful that the vortices interact at all.
In the illustration on the right hand side of Figure 6.3 the same variation of Θ is shown for a total momentum coefficient of $c_{\mu,3} = 0.117\,\%$. There the single measurement points indicate a low dependence on the phase shift, but considering the fitted line the dependency is insignificant. Moreover, the pressure recovery shows that for every phase shift the flow separation is suppressed. This means that the momentum input of the three actuation rows is sufficient to reattach the flow.
In Figure 6.4 the pressure recovery distribution is shown for a total momentum coefficient $c_{\mu,3} = 0.075\,\%$. In this case the constructive interaction is capable of reaching the same pressure recovery as the single actuation row depending on the phase shift. The measured points indicate a broad region of sufficient phase shifts Θ, where the cooperative actuation is capable to reasonably reattach the separated flow. This means that it is not necessary to hit the optimum phase shift or that the momentum coefficient can be reduced further with more effort, e.g a phase shift controlled actuation. Looking at the velocity ratio of the single actuator of $VR = 0.64$ and the associated single momentum coefficient of $c_\mu = 0.026\,\%$,

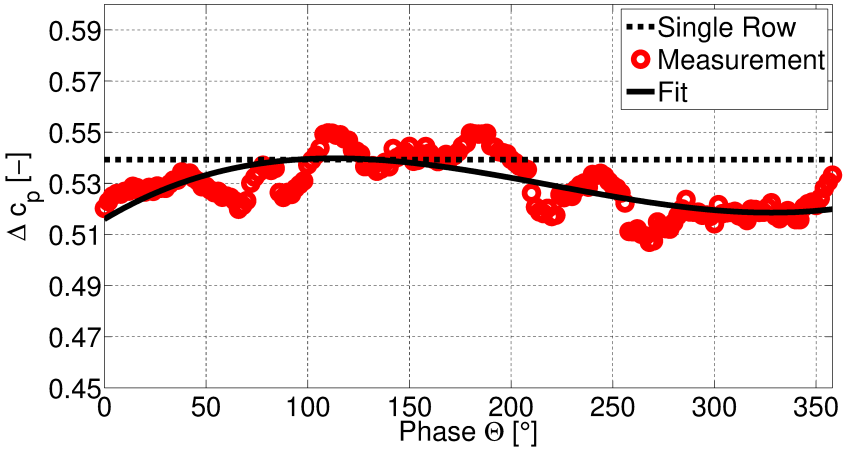

Figure 6.4: Pressure recovery Δc_p over different phase shifts Θ for $\dot{m}_3 = 0.003\,\frac{\mathrm{kg}}{\mathrm{s}}$

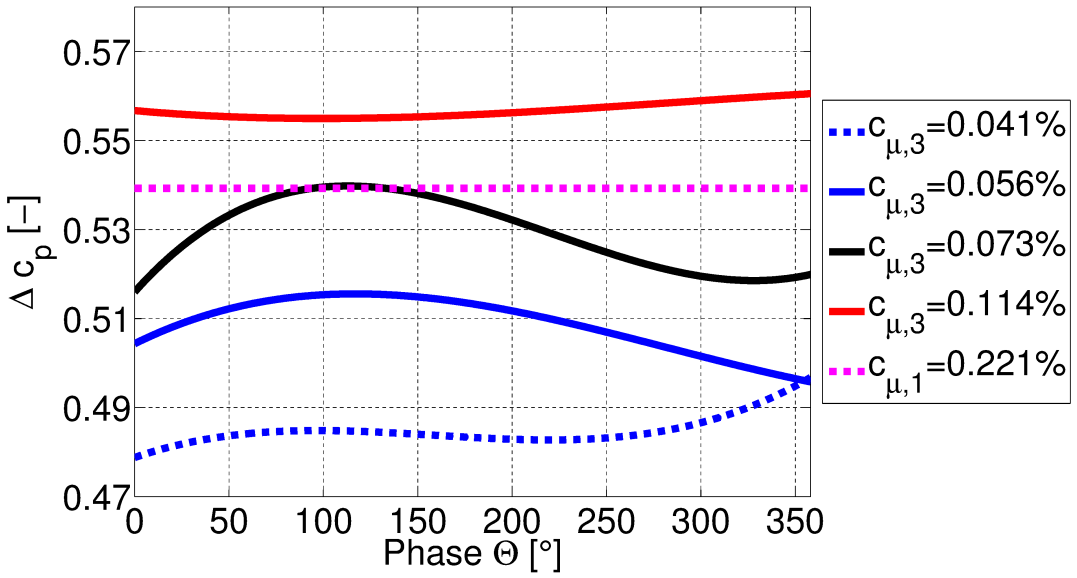

Figure 6.5: Comparison between cooperative actuation and single actuation (pink dotted line) for different momentum coefficients

these parameters are significantly lowered ($\Delta VR = 66\,\%$ and $\Delta c_\mu = 89\,\%$).
The main findings of pressure measurements are shown in Figure 6.5. The dotted line at $\Delta c_p = 0.54$ again is the pressure recovery of a single actuator row blowing with $c_{\mu,1} = 0.226\,\%$ for comparison. The other curves show the Δc_p for total momentum coefficients over the phase shift. These curves are the polynomials fitted lines of the measurements for clarity. Blowing with a $c_{\mu,3} = 0.042\,\%$ does not affect the separated flow as discussed before. When the amplitude is increased to $c_{\mu,3} = 0.057\,\%$ the separation is delayed. However, a phase dependence can be identified, with a maximum between $\Theta = 100\,°$ and $\Theta = 125\,°$. This corresponds to the finding discussed in section 5.1.2. Utilizing the cooperative effect has a positive influence on the separation. In this case the velocity ratio is $VR = 0.55$. Since the direct momentum increase in the detached area is small due to the low velocity and mass flow, the constructive merging of vortices must be responsible for the delay of the separation. The lowest momentum coefficient reaching the same performance as the single row is $c_{\mu,3} = 0.075\,\%$ as shown in Figure 6.4. The phase dependency of the Δc_p value is larger than before. Again the maximum can be identified between $\Theta = 100\,°$ and $\Theta = 125\,°$. This could lead to the assumption that the momentum coefficient has no significant impact on the required phase shift. However a look at the measurement results shows that the maximum of the pressure recovery is changing from $\Theta = 130\,°$ for $c_{\mu,3} = 0.057\,\%$ to $\Theta = 108\,°$ for $c_{\mu,3} = 0.075\,\%$. This is comparable to the results discussed in the section 5.1.2. Increasing the momentum coefficient even further ($c_{\mu,3} = 0.117\,\%$) results in a higher maximum pressure recovery than the single row active and shows limited dependency on the phase shift. A further increase of $c_{\mu,1}$ for the single row shows that the maximum pressure recovery to be reached is about $\Delta c_p \approx 0.55$. This means with three rows active an even higher Δc_p is achieved.
In Figure 6.6 the pressure recovery at the optimal phase shift of all measured cases are shown over the total momentum coefficient. Furthermore the pressure recovery for single actuation is shown for comparison. The points are polynomial fitted, to estimate the

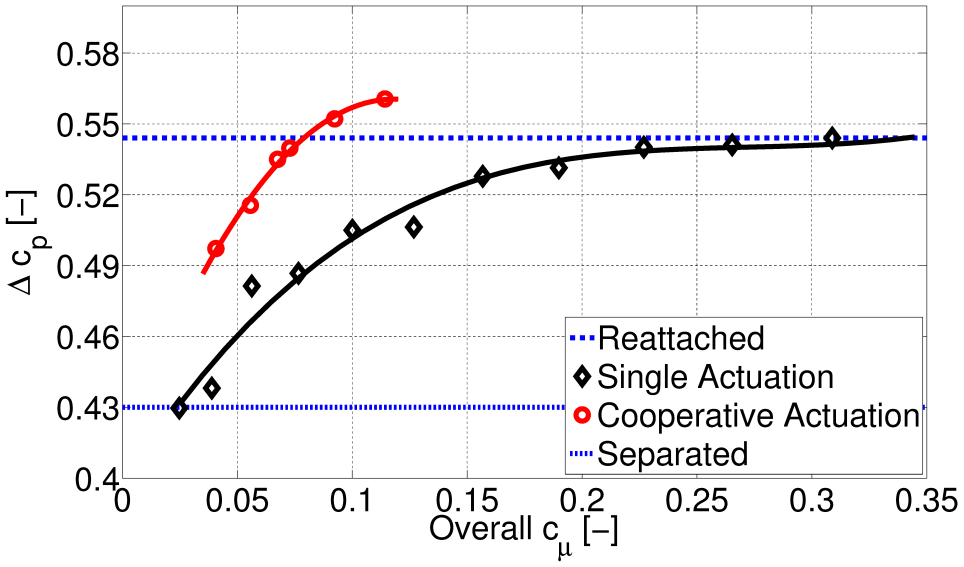

Figure 6.6: Comparison of single actuation to cooperative actuation in relation to the overall momentum coefficient c_μ

behavior of the pressure recovery with regard to the overall momentum coefficient. The illustration shows that $c_{\mu,3} = 0.075\,\%$ is the break even point with the single actuation. The comparison of the the actuator concepts shows that the momentum coefficient is reduced over the whole measured Δc_p range. However, as shown in the previous section, the phase shift between actuators after a merging process is not optimal, and with further adjustments the total momentum coefficient could be decreased further. The illustration also shows that a further increase of the momentum coefficient does not increase the pressure recovery proportionally. Nevertheless, a higher pressure recovery is achieved with less $c_{\mu,3}$.

6.1.3 Mass flow reduction

The velocity ratio and the momentum coefficient can be lowered by means of cooperative actuation as discussed in the previous sections. Since the momentum coefficient is not only affected by the jet velocity, but also by the mass flow, it is discussed in the following. Considering Figure 6.6, the break even point is reached with a velocity ratio of $VR = 0.64$. However, the overall mass flow consumption of all three actuator rows remains the same as for the single actuation. Nevertheless the above illustration also shows the separation is at least delayed that when the momentum coefficient is smaller. Furthermore it is also shown in Figure 4.6 that the cooperative actuation is not optimized due to the subsequent merging processes.
In Figure 6.7 velocity profiles at certain distances behind the actuators are shown for the single actuation concept compared to the separated flow. The positions are the same as illustrated in Figure 5.19. The black circles depict the velocity profile for the pressure induced separation. The back flow can be clearly distinguished, increasing with the location downstream. With active flow control the separation is reattached, resulting in a normal velocity profile. The illustration in the middle shows a surplus of velocity. This is due to the attached jet with a velocity ratio of $VR = 2.2$. The needed mass flow for reattaching the flow amounts to $\dot{m} = 2.8 \cdot 10^{-3} \frac{\text{kg}}{\text{s}}$. The same effect is visible in Figure 6.8 for the cooperative actuation with a velocity ratio of $VR = 0.8$ and a mass flow for the single actuator row of $\dot{m} = 0.9 \cdot 10^{-3} \frac{\text{kg}}{\text{s}}$. However, since three rows were active the overall consumption stays the same. Nevertheless the last illustration 6.9 shows a case with $15\,\%$ less total mass flow consumption. The profiles are still indicating an attached flow, even if it is smaller. The pressure recovery is $5\,\%$ lower than for the single actuation, which means the flow is delayed efficiently.
Therefore an estimation of the mass flow savings was done, taking all the measured pressure

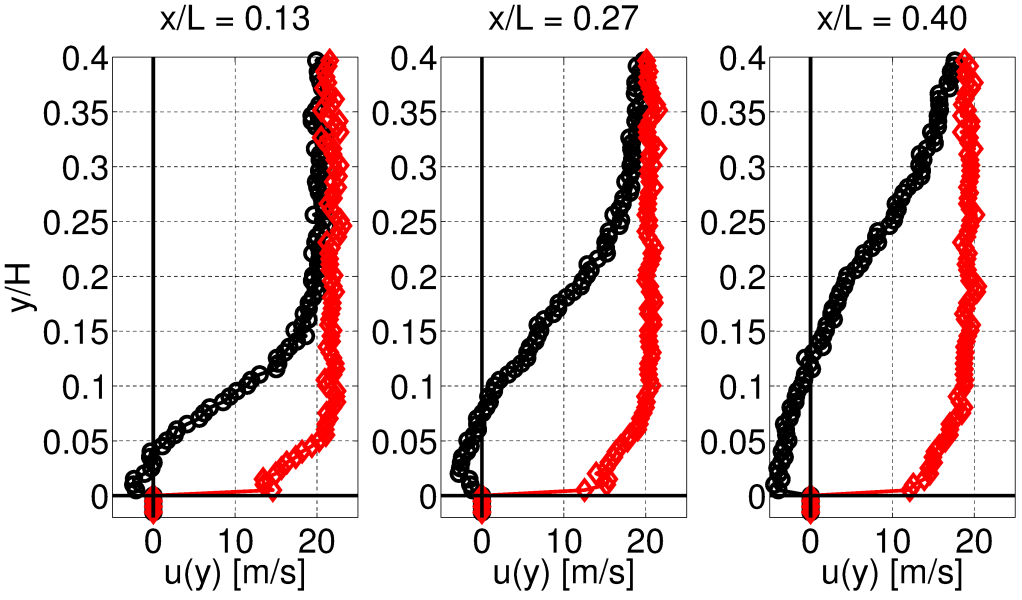

Figure 6.7: Velocity profiles at certain distances for single actuation with a momentum coefficient of $c_{\mu,1} = 0.22\,\%$

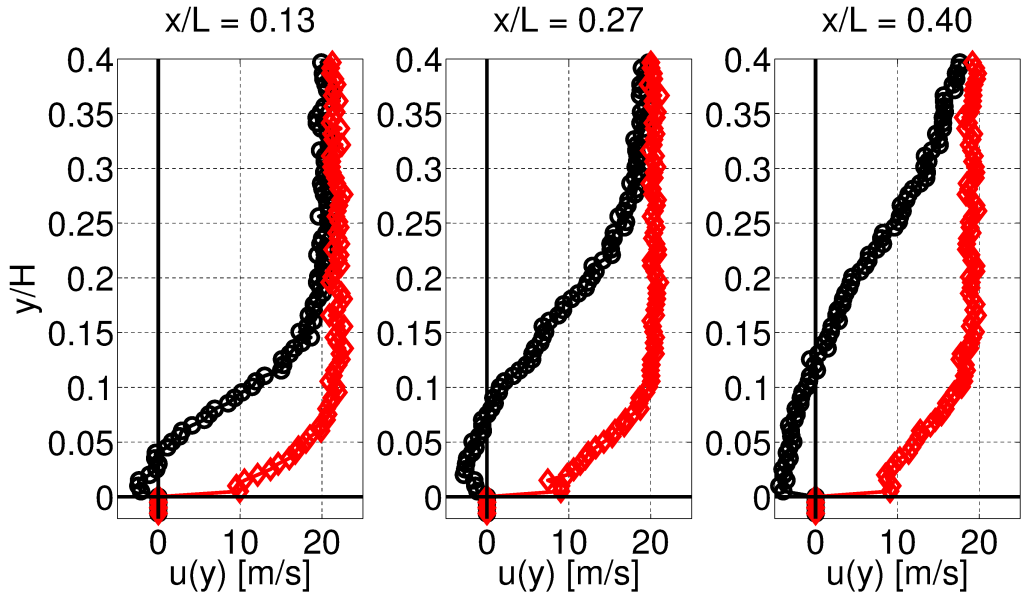

Figure 6.8: Velocity profiles at certain distances for cooperative actuation with a momentum coefficient of $c_{\mu,3} = 0.073\,\%$

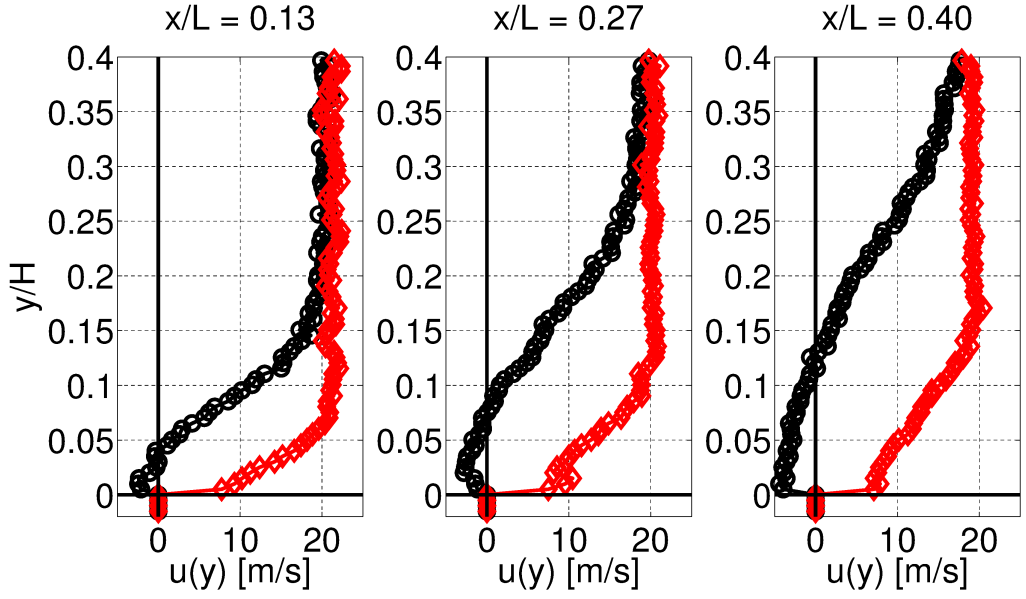

Figure 6.9: Velocity profiles at certain distances for cooperative actuation with a momentum coefficient of $c_{\mu,3} = 0.067\,\%$

recoveries for the single as well as for the cooperative actuation into account. These were used to estimate the potential mass flow savings with regard to the non-optimized system. For this, the measured points for the single actuation and the cooperative actuation are individually polynomial fitted as shown in figure 6.10(a). In the lower mass flow range the single actuation requires less mass flow than the cooperative actuation. This is due to the higher impulse of the single actuator, having a higher influence on the flow. However, with a certain mass flow ($\dot{m} = 2.3 \cdot 10^{-3}\,\frac{\mathrm{kg}}{\mathrm{s}}$) the cooperative actuation has a higher increase in Δc_p

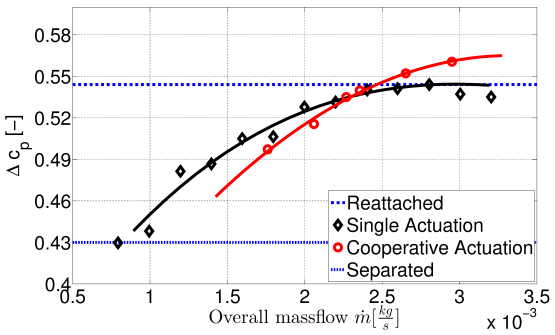

(a) Comparison of mass flow consumption for single and cooperative actuation

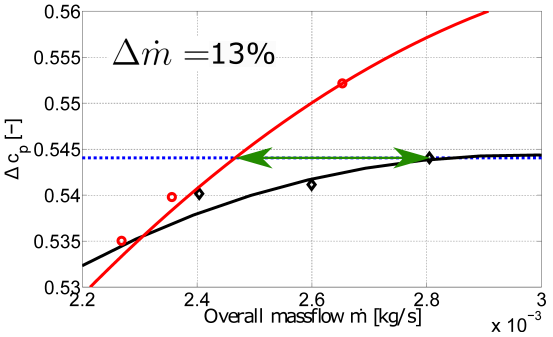

(b) Massflow savings of the cooperative actuation at the point of reattachment (Detailed view of (a))

Figure 6.10: Pressure recovery for single and cooperative actuation with regard to the overall massflow

than the single actuation with less mass flow consumption. Moreover, the single actuation saturates earlier than the cooperative one. Therefore the mass flow saving was computed for the highest measured pressure recovery of the single actuation ($\dot{m}_1 = 2.8 \cdot 10^{-3}\,\frac{\text{kg}}{\text{s}}$) with Equation 6.1.

$$\Delta\dot{m}(\Delta c_p) = \left(1 - \frac{\dot{m}_3\,(\Delta c_p)}{\dot{m}_1\,(\Delta c_p)}\right) \cdot 100 \tag{6.1}$$

As shown in figure 6.10(b) there is no measured point for the cooperative actuation equal to the single actuation. Therefore, the fitted line was taken for comparison (green arrow). The mass flow consumption for the single actuation to reattach the flow is $\dot{m}_1 = 2.8 \cdot 10^{-3}\,\frac{\text{kg}}{\text{s}}$. The same Δc_p is estimated to be achieved with $\dot{m}_3 = 2.44 \cdot 10^{-3}\,\frac{\text{kg}}{\text{s}}$. This leads to a saving of $\Delta\dot{m}\,(0.54) = 13\,\%$. Assumed that the single actuation concept would not saturate, the mass flow saving would further increase with higher Δc_p, because of the higher gradient with regard to the pressure recovery of the cooperative actuation concept. This means that with higher separation tasks the cooperative concept reveals a higher mass flow saving potential. On the other hand, at a certain point the cooperative concept has a performance increase compared to the single row concept.
Since the cooperative actuation is not optimized in terms of the phase shift nor the duty cycle, further savings can be expected. With a phase shift optimization a higher pressure recovery could be achieved with less mass flow. This would decrease the break even point with the single actuation and therefore increase the mass flow saving to reattach the flow. An even higher potential reveals the duty cycle as explained in the following.
The main effect of the cooperative actuation is the constructive interaction of vortices. Only an impulse is needed to build up a vortex at the beginning of the blowing phase, this effect can be used to lower the mass flow by reducing the duty cycle Λ. In Figure 6.11(a-d) the merging process of such a setup is shown. Here the duty cycle of the second and third row is set to $\Lambda_{2,3} = 25\,\%$ at a step Reynoldsnumber of $Re_H = 174000$. The vortex is merging as shown before (see Figure 5.16), resulting in a higher vorticity. Hence, this setup lowers the mass flow to $\Delta\dot{m} \approx 40\,\%$ per actuator. Utilizing the knowledge of vortex development by cutting the duty cycle back, results in an overall saving of $21\,\%$ for the whole system (see Figure 6.12). On the other hand this takes only the entrainment through shear layer into account, but the second mechanism, the increase of momentum,

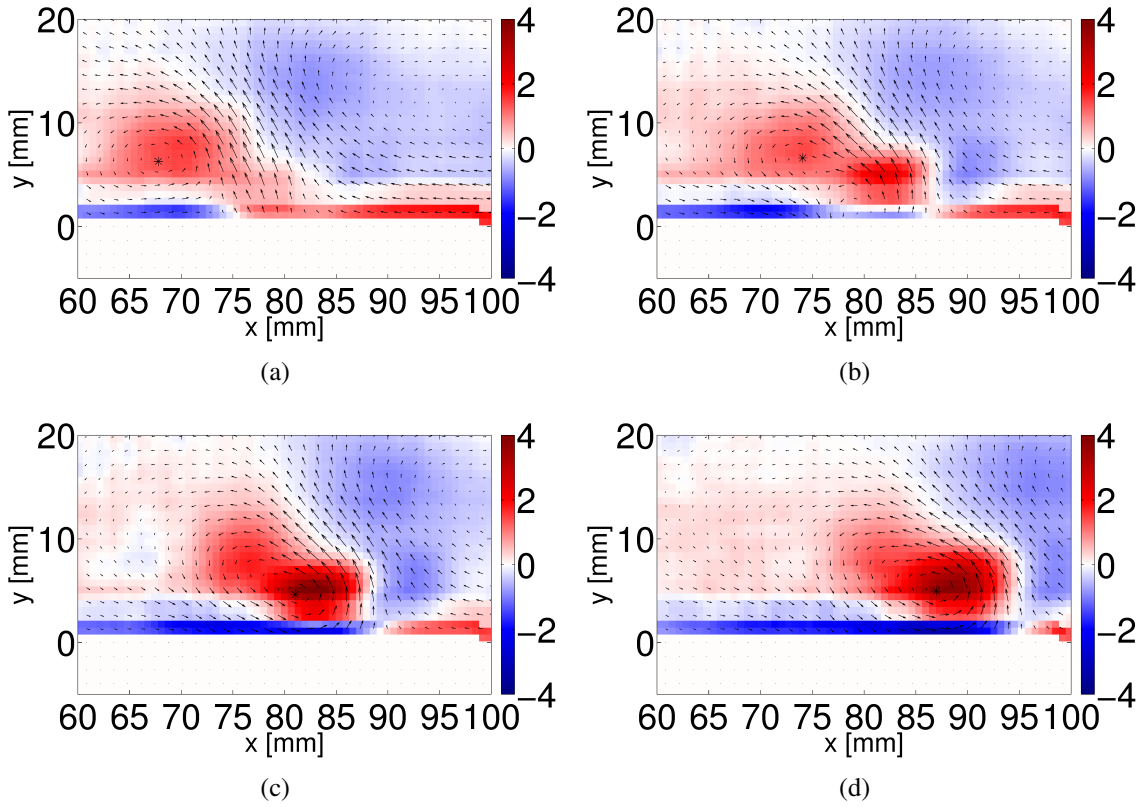

Figure 6.11: The merging process of a system configuration where the second and third row have a duty cycle of $\Lambda_{2,3} = 25\,\%$. The step angle is $\alpha = 23\,^\circ$ with an incident flow of $u_\infty = 20\,\frac{\mathrm{m}}{\mathrm{s}}$

is also affected by the duty cycle. A Strouhalnumber of $F^+ = 2$ with a velocity ratio of $VR = 1.9$ and a duty cycle of $\Lambda = 50\,\%$ results in an impulse of $\vec{p} \approx 3.8 \cdot 10^{-4}\,\mathrm{Ns}$ per period. The cooperative actuation with the same Strouhalnumber but with a velocity ratio of $VR = 0.64$ has an over all impulse of $\sum_i^n \vec{p}_i \approx 1.3 \cdot 10^{-4}$. However, the impulse is reduced for the cooperative actuation by $66\,\%$. Cutting down the duty cycle would result in a further decrease of the impulse dispensed by the actuator system. This loss has then to be compensated by the entrainment process.
Nevertheless, this opportunity reveals a great potential for future work and development of the cooperative system. A few possibilities to optimize this system are presented in the upcoming section.

6.2 Outlook and future work

Using the cooperative actuation it is possible to reduce the jet velocity to below the velocity of the incident flow. Therefore electric actuator concepts e.g. synthetic jets, can be reconsidered or at least lighter and smaller actuators can be developed. This is necessary at locations with strong limitations concerning the space, like the outer wing section of an aircraft. Furthermore, with lower requirements regarding the mass flow smaller pipes or supply systems can be provided, cutting down the overall mass of the active flow control system.
The next step to optimize this system would be, to further consider the enhancing effect of the cooperative actuation. As shown above the duty cycle discloses a great potential to auxiliary reduce the mass flow. To bring this system one step further the duty cycle for all rows has to be reduced. Since this is also cutting down the second mechanism of this system, an optimal equilibrium between the duty cycle and the direct increase of momentum should be detected. Moreover, a redesign of the actuator slot regarding the jet angle must be considered, since it has been presented by Hecklau ([32]) that a higher jet angle supports the reduction of the duty cycle. Figure 6.12 indicates that such a configuration lowers the overall mass flow to around $\Delta\dot{m} \approx 31\,\%$.
Further steps to evolve the cooperate actuation must concern the **interaction of the vortices** to enhance the capability of such a system. Furthermore a **mass flow control algorithm** should be established for additional savings. Last but not least the actuation system would be more effective if the average **detachment line** is sensed, giving the closest row the most authority. An outlook over these improvements are given below.
As shown in section 5.1.2, the propagation velocity of a merged vortex is increased by the interaction. Thus, the successive interactions after the first merging process can be optimized. An adjustment would increase the performance and the actuation parameters can

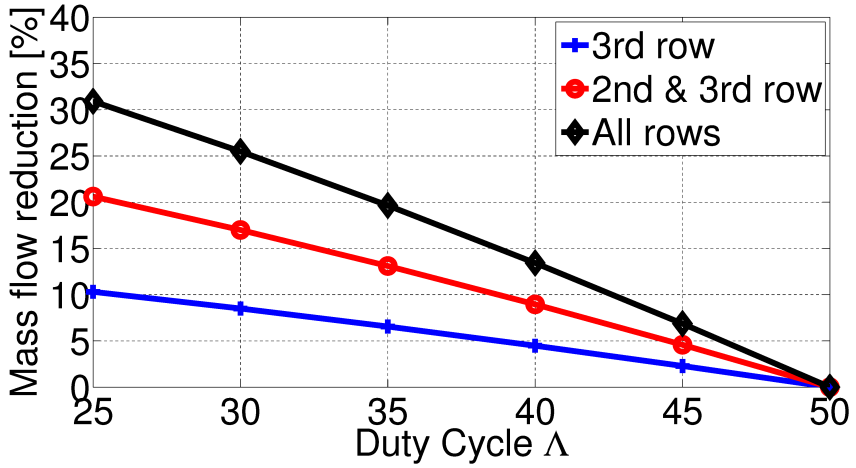

Figure 6.12: Estimated additional mass flow savings at the same overall momentum coefficient $c_{\mu,3}$ for different duty cycles Λ and different actuation concepts. Duty cycle lowered for the 3rd row and the the other two rows still set to $50\,\%$ (blue). Duty cycle lowered for the 2nd and 3rd row, but still $50\,\%$ for the first (red). Duty cycle lowered for all rows (black).

be further reduced. This adjustment of the phase shift Θ can be realized by implementing a control algorithm concerning the propagation velocity. The controlling can be done with different sensors. Hot film sensors achieve a high sampling rate and therefore a high temporal solution, but they are not practical in real world application, due to their sensitive structure. Therefore wall mounted pressure sensors are preferable for a functional sensor-actuator system. Such a buildup would not only optimize the cooperative actuation system, but is also independent from the flow parameters. While the adverse pressure gradient is affecting the propagation velocity a change of the incident flow as well as the separation area would change the parameters of the system. A sufficient control algorithm is capable of handling these amendments. It is plausible that the actuator parameters, e.g. the mass flow, can be optimized, with an optimal phase shift, resulting in a more efficient active flow control system.
Thinking about control algorithm, another optimization concerning the mass flow could be considered. In a real world application the mass flow has to be provided from the jet engines or an extra compressor, which results in a performance loss or additional weight. With the pressure recovery a simple but effective method is presented to rate the state of separation. Utilizing this, a control unit could optimize the mass flow for a given flow condition ensuring that only a minimum is used to reattach the separation.
Concerning the results stated by Troshin and Seifert [82], the actuator nearest to the separation is the most sufficient one. With several rows this knowledge can be used to increase the performance of the cooperative actuation. The sensors of a phase shift control unit can also be used to detect the average detachment line giving the nearest actuator row the most authority. For example, a pressure induced separation of a flap begins at the trailing edge moving upstream with the flap deflection δ. Thus the authority of the single actuator row is changing with the detachment line, still using the cooperative effect of all rows to increase the performance. A change of the authority can be done by increasing the duty cycle of that row, if the above mentioned duty cycle reduction is deployed.
An advantage of the cooperative actuation is the built-in redundancy. Having several rows of actuators, a loss of one actuator can be compensated by increasing the authority of an actuator in the above or following row. This would not even result in a higher mass flow consumption, if the phase shift is controlled as stated before. However, this means that the actuators have to be monitored regarding their performance. This can be done for example, by measuring the pressure inside of the actuators.
In the long run it would be preferable to have an autonomous system, capable of controlling independently the actuators, the phase shift, the mass flow and the authority towards the detachment line. However, such a system increases the complexity of the overall system, but the advantages would outweigh this drawback by effectively reducing the mass flow, power consumption and the robustness of the single actuator.

7 Conclusion

Much effort is put into the wing design of an aircraft by the manufacturers to optimize the aerodynamics for the various phases of flight. Especially in low speed flight conditions, like the take-off and landing, the performance must be enhanced using high lift devices. At locations with limited space , it is nearly impossible to deploy slats. This positions are predestined for the application of active flow control. Since these systems require energy, a novel system enhancing the mechanism of reattachment is needed. To prove the feasibility of this approach basic investigations were successfully performed.
The results of the examinations of a cooperative actuation show that it is possible to use the effect of enhancing coherent structures induced by the active flow control system to delay the separation or reattach the flow of a pressure induced separation. The velocity ratio as well as the momentum coefficient can be significantly lowered compared to a single actuation concept.
The two mechanisms of reattachment, direct increase of momentum in the separated area and the entrainment through shear layer by induced vortices, are closely considered. The coherent structures are generated through pulsed blowing and enhanced and stabilized with further actuators located downstream. First the interaction process was investigated on a flat plate. Later on the results were transferred to a half diffuser, where a pressure induced separation can be provided. Thereby it is proven that at least the entrainment through a shear layer is used constructively by enhancing the induced coherent structures. Depending on the delay between the excitation phase of the single actuator rows, the vortices are merging, annihilating or not effecting each other.
Large-scale vortex structures are generated trough pulsed blowing. Theses coherent structures are propagating downstream, depending on the jet and the velocity of the incident flow. This initiates a fluid transfer through the shear layer, which transports low energy fluid away from the surface and high energy from the incident flow into the detached area. For a duty cycle of $\Lambda = 50\,\%$ the jet angle affects the behavior of the jet. For jet angle of $\alpha_{jet} = 45\,^\circ$ the jet is attached to the surface, directly increasing the momentum of the separated area.
The propagation velocity mainly depends on the velocity of the incident flow, but especially after the generation of a vortex also on the chosen velocity ratio. After the formation of the vortex the propagation velocity drops to a value slightly above the incident flow. Then it decreases slowly, while propagating downstream until it dissipates. Thus the vortex moves away from the surface throughout the boundary layer. By leaving the boundary layer, the propagation velocity is rapidly increased, but the vortex propagation velocity increases as fast as it vanishes.
The investigation of the merging process on a flat plate demonstrates the dependence of constructive interaction on the phase shift of the excitation. It can be divided into four different processes. Inducing the subsequent vortices of the following actuators too early or too late results in several vortices propagating downstream, but still affecting each other.

Due to the opposite normal velocity of the vortices the entrainment process of each vortex is impeded by the following one. Furthermore, the high energy fluid dispensed by the jet is transported away by the following one. Utilizing the propagation velocity obtained from the single actuator investigations, to induce the next vortex when the previous arrives directly at the slot location, results in a co-rotating vortex pair interfering with each other. This interaction dissipates energy, therefore only one weak vortex survives. As a consequence, the entrainment process is at least impeded and the reattachment process is mainly driven by the jet dispensing high energy fluid. This means that the needed mass flow must be increased. If the vortex arises after the previous vortex is located right behind the actuator slot, the vortices are mostly annihilating each other. By the ongoing blowing of the actuator a new vortex builds up, with less vorticity and therefore less impact on the entrainment process. To actually merge two co-rotating vortices, the second one must be induced before the preceding vortex arrives. Then the jet of the new one and the vorticity of the preceding one have a constructive effect on each other resulting in a bigger and stronger vortex. An additional advantage is that the preceding vortex is pushed down to the surface again.
This knowledge is transferred to a half diffuser with pressure induced separation. In this investigation the step angle of the half diffuser was set in a way to locate the average separation line upstream the first actuator. By doing so a more challenging case was chosen to show the effectiveness of the multiple cooperative actuation. The adverse pressure gradient of the separation is affecting the propagation velocity of the vortex. First of all the velocity of propagation is slowed down. Furthermore the vortex casts away from the surface more rapidly leading to a shorter duration of the vortex. The merging process itself seems relatively independent of the pressure gradient, even if the phase of excitation has to be adjusted. Another point is that the constructive interaction process accelerates the vortex propagation so that the phase shift between subsequent actuators should be adjusted after a merging process. By varying the phase shift and analyzing the vorticity the different interaction processes can be restricted. A constructive interaction takes place for phase shifts, where the vortex built up in front of the arriving one and the vorticity is enhanced. Inducing the vortex later leads to a state called transition of merging. In this state the vortices sometimes merge and sometimes don't. Depending, which is happening more often the rate of vorticity is lower or higher. If the phase shift of excitation is increased further, the vortices are annihilating each other.
The state of flow in the half diffuser can be rated with the pressure recovery Δc_p. The static pressure increases as a function of the angle of the inclined step α_{step}, by converting kinetic energy into into pressure energy. This happens until the flow cannot follow the surface anymore and detaches. The static pressure decreases within the separated area. This behavior can be measured by means of a pressure transducer, before and after the step. The difference between these sensors yields the pressure recovery. Active flow control is supposed to suppress the separation, with a certain set of parameters. The conventional system, consisting of a single actuator or a row of several adjacent actuators, needs a high velocity ratio and a sufficient amount of mass flow. Cooperative actuation is supposed to reduce the velocity ratio by utilizing constructive interaction between the actuator rows. As shown in section 6.1.2, the velocity ratio is reduced by $\Delta VR = 66\,\%$ and the momentum coefficient of the single actuator by $\Delta c_\mu = 89\,\%$. The overall system saving is measured with the total momentum coefficient taking all rows into account. Compared to a single row the gain is still up to $66\,\%$.

Nevertheless the mass flow required to reattach the flow remains the same. But looking at Figure 6.10 and 6.9, the cooperative actuation is supposed to cut down these requirements. Therefore the potential mass flow savings are estimated. It is very likely that the cooperative actuation can reduce the required mass flow up to $\Delta\dot{m} \approx 10\,\%$. It should be recalled that the system is not optimized regarding the phase shift or the velocity ratio. Since the system aims at enhancing or at least stabilizing the vortex responsible for the entrainment through shear layer, the duty cycle of the second and third row was set to $\Lambda_{2,3} = 25\,\%$. The PIV measurements show that through the merging process the vortex is still enhanced. Such an adjustment leads to an overall saving of $\Delta\dot{m} = 21\,\%$. Other authors showed that the reattachment process can be triggered by only using the entrainment through shear layer. Utilizing this, all actuator rows can be set to a duty cycle of $\Lambda_{1,2,3} = 25\,\%$, which would lead to a saving of $\Delta\dot{m} = 31\,\%$. However, a redesign of the actuator slot regarding the jet angle should be considered. It is also shown that the merging process influences the propagation velocity of the vortex and therefore the related phase shift. A control algorithm would be capable to deal with that issue, by adjusting the phase shift individually. That would lead to further savings regarding the mass flow.
Additional positive side effects of the cooperative actuation are the built in redundancy and the possibility to react to the separation individually. This basic investigation of this new actuation concept shows promising results for future applications and creates the conditions for further investigations and developments to bring this system to market maturity.

Bibliography

[1] K. K. Ahuja, R. R. Whipkey, and G. S. Jones. Control of turbulent boundary layer flows by sound. *AIAA paper*, 726:1983, 1983.

[2] J. D. Anderson. *Fundamentals of Aerodynamics*. McGraw-Hill, Inc, 1991.

[3] M. J. Bamber. *Wind-tunnel tests on airfoil boundary layer control using a backward-opening slot*. National Advisory Committee for Aeronautics, 1932.

[4] M. Bauer. *Design and application of a fluidic actuator system for high lift flow control*. PhD thesis, Technische Universität Berlin, 2015.

[5] J. J. Bertin and M. L. Smith. *Aerodynamics for engineers*. Prentice-Hall, 1979.

[6] F. K. Browand and C. M. Ho. The mixing layer-an example of quasi two-dimensional turbulence. *Journal de Mecanique Theorique et Appliquee Supplement*, 1:99–120, 1983.

[7] L. N. Cattafesta III and M. Sheplak. Actuators for active flow control. *Annual Review of Fluid Mechanics*, 43:247–272, 2011.

[8] D. R. Chapman, D. M. Kuehn, and H. K. Larson. Investigation of separated flows in supersonic and subsonic streams with emphasis on the effect of transition. 1958.

[9] Y. Cheng. Mean shift, mode seeking, and clustering. *Pattern Analysis and Machine Intelligence, IEEE Transactions on*, 17(8):790–799, 1995.

[10] F. G. Collins and J. Zelenevitz. Influence of sound upon separated flow over wings. *AIAA journal*, 13(3):408–410, 1975.

[11] D. Comaniciu and P. Meer. Mean shift: A robust approach toward feature space analysis. *Pattern Analysis and Machine Intelligence, IEEE Transactions on*, 24(5):603–619, 2002.

[12] L. Cortelezzi and A. R. Karagozian. On the formation of the counter-rotating vortex pair in transverse jets. *Journal of Fluid Mechanics*, 446:347–373, 2001.

[13] T. Crittenden, B. Warta, and A. Glezer. Characterization of combustion powered actuators for flow control. *AIAA paper*, 2864:2006, 2006.

[14] S. C. Crow. Stability theory for a pair of trailing vortices. *AIAA journal*, 8(12):2172–2179, 1970.

[15] D. E. Culley. Variable frequency diverter actuation for flow control. In *3rd AIAA Flow Control Conference*, page 3034, 2006.

[16] A. D. Cutler, B. T. Beck, J. A. Wilkes, J. P. Drummond, D. W. Alderfer, and P. M. Danehy. Development of a pulsed combustion actuator for high-speed flow control. *AIAA paper*, 1084:2005, 2005.

[17] K. G. Derpanis. Mean shift clustering. *Lecture Notes. http://www. cse. yorku. ca/~ kosta/CompVis_Notes/mean_shift. pdf*, 2005.

[18] DLR. Pricipal-PIV-Setup. `http://www.dlr.de/as/en/Portaldata/5/Resources/images/abteilungen/abt_ev/artikel/PIV_img1_xl.jpg`, 2016. [Online; accessed 20-March-2016].

[19] A. Eroglu and R. E. Breidenthal. Structure, penetration, and mixing of pulsed jets in crossflow. *AIAA journal*, 39(3):417–423, 2001.

[20] A. Eroglu and R. E. Breidenthal. Structure, penetration, and mixing of pulsed jets in crossflow. *AIAA journal*, 39(3):417–423, 2001.

[21] European Union. Commission regulation (ec) no 796/2002. *Official Journal of the European Communities*, L128:22, 2002.

[22] M. A. Fischler and R. C. Bolles. Random sample consensus: a paradigm for model fitting with applications to image analysis and automated cartography. *Communications of the ACM*, 24(6):381–395, 1981.

[23] T. F. Fric and A. Roshko. Structure in the near field of the transverse jet. In *7th Symposium on Turbulent Shear Flows, Volume 1*, volume 1, page 6, 1989.

[24] T.F. Fric and A. Roshko. Vortical structure in the wake of a transverse jet. *Journal of Fluid Mechanics*, 279:1–47, 1994.

[25] M. Gad-el Hak. Modern developments in flow control. *Applied Mechanics Reviews*, 49(7):365–379, 1996.

[26] A. Glezer. Some aspects of aerodynamic flow control using synthetic-jet actuation. *Philosophical Transactions of the Royal Society of London A: Mathematical, Physical and Engineering Sciences*, 369(1940):1476–1494, 2011.

[27] A. Glezer and M. Amitay. Synthetic jets. *Annual Review of Fluid Mechanics*, 34(1):503–529, 2002.

[28] D. Greenblatt and I. J. Wygnanski. The control of flow separation by periodic excitation. *Progress in Aerospace Sciences*, 36(7):487–545, 2000.

[29] J. W. Gregory, E. P. Gnanamanickam, J. P. Sullivan, S. Raghu, and D. Fellow. Variable-frequency fluidic oscillator driven by piezoelectric devices. In *AIAA Journal, 43rd AIAA Aerospace Sciences Meeting & Exhibit Reno, NV*, 2005.

[30] J. W. Gregory, J. C. Ruotolo, A. R. Byerley, and T. E. McLaughlin. Switching behavior of a plasma-fluidic actuator. *AIAA paper*, 785:2007, 2007.

[31] C. D. Hansen and C. R. Johnson. *Visualization handbook*. Academic Press, 2011.

[32] M. Hecklau. *Experimente zur aktiven Strömungsbeeinflussung in einer Verdichterkaskade mit pulsierenden Wandstrahlen*. PhD thesis, Technische Universität Berlin, 2012.

[33] M. Hecklau and W. Salazar, D. P.and Nitsche. Influence of the actuator jet angle on the reattachment process with pulsed excitation. In *New Results in Numerical and Experimental Fluid Mechanics VIII*, pages 143–150. Springer, 2013.

[34] C. Ho and L. Huang. Subharmonics and vortex merging in mixing layers. *Journal of Fluid Mechanics*, 119:443–473, 1982.

[35] C. Ho and P. Huerre. Perturbed free shear layers. *Annual Review of Fluid Mechanics*, 16(1):365–422, 1984.

[36] J. D. Hodges, Z. D. Little, Craig P. Fernandes, G. Natsui, and J. S. Kapat. The effect of inclination angle on turbulent quantities of a single row of cylindrical jets in crossflow. In *51st AIAA/SAE/ASEE Joint Propulsion Conference*, page 4198, 2015.

[37] V. Holmén. Methods for vortex identification. *MasterâĂŹs Theses in Mathematical Sciences*, 2012.

[38] B. M. Horton. Fluid-operated system, February 25 1964. US Patent 3,122,165.

[39] F. Hsiao, J. Shyu, and C. Liu. Control of wall-separated flow by internal acoustic excitation. *AIAA journal*, 28(8):1440–1446, 1990.

[40] J. Jeong and F. Hussain. On the identification of a vortex. *Journal of fluid mechanics*, 285:69–94, 1995.

[41] G. V. Lachmann. *Boundary layer and flow control: its principles and application*. Elsevier, 2014.

[42] S. Le Dizes and A. Verga. Viscous interactions of two co-rotating vortices before merging. *Journal of Fluid Mechanics*, 467:389–410, 2002.

[43] A. Leder. *Abgelöste Strömungen Physikalische Grundlagen*. Grundlagen und Fortschritte der Ingenieurwissenschaften. Vieweg+Teubner Verlag, 1992.

[44] M. A. Leschziner and S. Lardeau. Simulation of slot and round synthetic jets in the context of boundary-layer separation control. *Philosophical Transactions of the Royal Society of London A: Mathematical, Physical and Engineering Sciences*, 369(1940):1495–1512, 2011.

[45] J. Lin, F. Howard, and G. Selby. Turbulent flow separation control through passive techniques. In *Shear Flow Conference*, pages –. American Institute of Aeronautics and Astronautics, March 1989.

[46] R.T. M'closkey, J.M. King, L. Cortelezzi, and A.R. Karagozian. The actively controlled jet in crossflow. *Journal of Fluid Mechanics*, 452:325–335, 2002.

[47] L. P. Melton, C. S. Yao, and A. Seifert. Active control of separation from the flap of a supercritical airfoil. *AIAA journal*, 44(1):34–41, 2006.

[48] P. Meunier, U. Ehrenstein, T. Leweke, and M. Rossi. A merging criterion for two-dimensional co-rotating vortices. *Physics of Fluids (1994-present)*, 14(8):2757–2766, 2002.

[49] P. Meunier and T. Leweke. Three-dimensional instability during vortex merging. *Physics of Fluids (1994-present)*, 13(10):2747–2750, 2001.

[50] W. Mokhtar. A numerical parametric study of high-lift low reynolds number airfoils. In *Aerospace Sciences Meetings*, pages –. American Institute of Aeronautics and Astronautics, January 2005.

[51] N. M. Morris. *An introduction to fluid logic*. McGraw-Hill, 1973.

[52] H. Nagib, J. Kiedaisch, P. Reinhard, and B. Demanett. Control techniques for flows with large separated regions: A new look at scaling parameters. *AIAA paper*, 2857:2006, 2006.

[53] M. Nishioka, M. Asai, and S. Yoshida. Control of flow separation by acoustic excitation. *AIAA journal*, 28(11):1909–1915, 1990.

[54] B. Nishri and I. Wygnanski. Effects of periodic excitation on turbulent flow separation from a flap. *AIAA journal*, 36(4):547–556, 1998.

[55] W. Nitsche and A. Brunn. *Strömungsmesstechnik*. Springer, 2. auflage edition, 2006.

[56] D. Oster, I. Wygnanski, B. Dziomba, and H. Fiedler. On the effect of initial conditions on the two dimensional turbulent mixing layer. In H. Fiedler, editor, *Structure and Mechanisms of Turbulence I*, volume 75 of *Lecture Notes in Physics*, pages 48–64. Springer Berlin Heidelberg, 1978.

[57] R. Petz and W. Nitsche. Active separation control on the flap of a two-dimensional generic high-lift configuration. *Journal of Aircraft*, 44:865–874, 2007.

[58] M. W. Plesniak and D. M. Cusano. Scalar mixing in a confined rectangular jet in crossflow. *Journal of Fluid Mechanics*, 524:1–45, 2005.

[59] F. H. Post, B. Ma, D. C. Banks, H. Pagendarm, et al. Selective visualization of vortices in hydrodynamic flows. In *Visualization'98. Proceedings*, pages 419–422. IEEE, 1998.

[60] L. Prandtl. *Ergebnisse der aerodynamischen Versuchsanstalt zu Göttingen*, volume 3. Universitätsverlag Göttingen, 2009.

[61] A. Qayoum, V. Gupta, P. K. Panigrahi, and K. Muralidhar. Influence of amplitude and frequency modulation on flow created by a synthetic jet actuator. *Sensors and Actuators A: Physical*, 162(1):36–50, 2010.

[62] M. Raffel, C. E. Willert, J. Kompenhans, et al. *Particle image velocimetry: a practical guide*. Springer, 2013.

[63] H. Reed and W. Saric. Transition mechanisms for transport aircraft. In *Fluid Dynamics and Co-located Conferences*, pages –. American Institute of Aeronautics and Astronautics, June 2008.

[64] M. Salewski, D. Stankovic, L. Fuchs, and E. Gutmark. Coherent structures in circular and non-circular jets in crossflow. In *44th AIAA Aerospace Sciences Meeting and Exhibit*, pages 2006–907, 2006.

[65] R. Sau and K. Mahesh. Optimization of pulsed jets in crossflow. *Journal of Fluid Mechanics*, 653:365–390, 2010.

[66] H. Schlichting and K. Gersten. *Boundary-layer theory*. Springer Science & Business Media, 2000.

[67] H. Schlichting and E. Truckenbrodt. *Aerodynamik des Flugzeuges*. Springer Berlin, Heidelberg, 1969.

[68] A. Seifert, T. Bachar, D. Koss, M. Shepshelovich, and I. Wygnanskil. Oscillatory blowing: a tool to delay boundary-layer separation. *AIAA journal*, 31(11):2052–2060, 1993.

[69] A. Seifert and L. G. Pack. Oscillatory excitation of unsteady ressible flows over airfoils at flight reynolds numbers. 1999.

[70] S. R. Shapiro, J. King, R. T. M'Closkey, and A. R. Karagozian. Optimization of controlled jets in crossflow. *AIAA journal*, 44(6):1292–1298, 2006.

[71] M. Shiokawa, K. Matsushima, and K. Nakahashi. Design and aerodynamics of lift enhancement control for a single element airfoil. In *43rd AIAA Aerospace Sciences Meeting and Exhibit*, page 2005, 2005.

[72] A. Shmilovich and Y. Yadlin. Flow control for the systematic buildup of high-lift systems. *Journal of Aircraft*, 45(5):1680–1688, 2008.

[73] A. Shmilovich and Y. Yadlin. Flow control techniques for transport aircraft. *AIAA Journal*, 49(3):489–502, 2011.

[74] A. M. O. Smith. High-lift aerodynamics. *Journal of Aircraft*, 12(6):501–530, 1975.

[75] D. Sujudi and R. Haimes. Identification of swirling flow in 3d vector fields. Technical report, Technical report, Department of Aeronautics and Astronautics, MIT, 1995. AIAA Paper 95-1715, 1995.

[76] F. Ternoy, J. Dandois, F. David, and M. Pruvost. Overview of onera actuators for active flow control. *AerospaceLab*, pages p–1, 2013.

[77] V. Tesař, C. Hung, and W. B. Zimmerman. No-moving-part hybrid-synthetic jet actuator. *Sensors and Actuators A: Physical*, 125(2):159–169, 2006.

[78] V. Tesař, S. Zhong, and F. Rasheed. New fluidic-oscillator concept for flow-separation control. *AIAA journal*, 51(2):397–405, 2012.

[79] F. Thomas. *Untersuchungen über die Erhöhung des Auftriebes von Tragflügeln mittels Grenzschichtbeeinflussung durch Ausblasen*. DFL-Bericht. Dt. Forschungsanstalt f. Luft- u. Raumfahrt e.V., 1962.

[80] F. Tinapp. *Aktive Kontrolle der Strömungsablösung an einer Hochauftriebs-Konfiguration*. PhD thesis, Technische Universität Berlin, 2001.

[81] P. H. S. Torr and A. Zisserman. MLESAC: A new robust estimator with application to estimating image geometry. *Journal of Computer Vision and Image Understanding*, 78(1):138–156, 2000.

[82] V. Troshin and A. Seifert. Performance recovery of a thick turbulent airfoil using a distributed closed-loop flow control system. *Experiments in fluids*, 54(1):1–19, 2013.

[83] H. Vollmers. Detection of vortices and quantitative evaluation of their main parameters from experimental velocity data. *Measurement Science and Technology*, 12(8):1199, 2001.

[84] J. Westerweel. *Digital particle image velocimetry: theory and application*. TU Delft, Delft University of Technology, 1993.

[85] J. Wild, G. Wichmann, F. Haucke, I. Peltzer, and P. Scholz. Large scale separation flow control experiments within the german flow control network. In *47th AIAA Aerospace Sciences Meeting*, page 530, 2009.

[86] I. Wygnanski. The variables affecting the control of separation by periodic excitation. In *Fluid Dynamics and Co-located Conferences*, pages –. American Institute of Aeronautics and Astronautics, June 2004.

[87] K. Zaman, A. Bar-Sever, and S.M. Mangalam. Effect of acoustic excitation on the flow over a low-re airfoil. *Journal of Fluid Mechanics*, 182:127–148, 1987.

[88] P. Zhang, J. Wang, and L. Feng. Review of zero-net-mass-flux jet and its application in separation flow control. *Science in China Series E: Technological Sciences*, 51(9):1315–1344, 2008.